Low-Frequency Wave Dynamics over a Fringing Reef

Observations from La Saline Reef, La Réunion

MSc Thesis

Margot Giliam



Delft University of Technology

TU Delft

Low-Frequency Wave Dynamics over a Fringing Reef

Observations from La Saline Reef, La Réunion

by

Margot Giliam

Supervisors Delft University of Technology:	Dr. M.F.S. Tissier and Dr.ir. M.A. de Schipper
Supervisor Université de Bretagne Occidentale:	Dr. F. Floc'h
Faculty:	Faculty of Civil Engineering and Geosciences, Delft
Department:	Hydraulic Engineering
Date:	24 August 2026

TU Delft

Preface

I would like to thank several people who contributed to this thesis and supported me throughout the process.

First of all, I would like to thank my thesis committee. Marion and France, thank you for giving me the opportunity to work on this project. France, thank you for welcoming me in Brest, for all your explanations, for always being available to help, and for making time for my questions. Marion, thank you for the discussions, your enthusiasm, and the many useful suggestions and feedback that helped shape this research. Matthieu, thank you for your input and the helpful comments during our meetings. Mila, thank you as well for your help during my thesis.

I would also like to thank everyone involved in the FUTURISKS project for making this research possible and for giving me the opportunity to join the workshop on Île de Batz.

Finally, I would like to thank my friends and family for their support throughout my thesis. Han, thank you for helping me with the move to Brest. Michiel and Danique, thank you for your support and for always giving me a place to stay whenever I was back in the Netherlands. Erik, thank you for visiting me in Brest and for the fun surfing sessions. Eliane, Barte, Imke, and Marloes, thank you for coming all the way to Brest to visit me, even when there was no wind. Luca, thank you for always supporting me and for all the good times we have together. Sofie, thank you for always being interested in my thesis and for the fun phone calls.

Margot Giliam
Delft, August 2026

Abstract

Coral reefs provide natural coastal protection by strongly dissipating incident gravity-wave (GW) energy. However, over shallow fringing reefs, low-frequency (LF) waves can dominate water-level variability and contribute substantially to shoreline run-up. The present study aims to identify the processes and forcing conditions that govern the magnitude and transformation of infragravity (IG) and very-low-frequency (VLF) waves over a fringing reef. For this purpose, an observational dataset was analysed, collected over approximately three months between June and September 2024 at the La Saline fringing reef on the microtidal western coast of La Réunion. It consisted of pressure and velocity measurements at multiple locations extending from the reef slope across the reef flat. In addition, pressure and velocity measurements close to the shoreline and video-derived run-up observations were available for 11 July 2024.

This study showed that the reef acts as a strong low-pass filter, with GW height decreasing on average by $97.6\,\%$ from the reef slope to the mid-reef, causing IG and VLF waves to dominate the reef-flat wave field. Variability in both IG and VLF wave heights was mainly explained by the offshore GW power and was further modulated by the water level. IG wave heights at the mid-reef remained approximately equal to their offshore magnitude, whereas VLF wave heights were on average amplified by $235\,\%$ relative to offshore conditions. In addition, observations on 11 July showed that IG wave heights increased again shoreward, while VLF wave heights remained approximately constant between the mid-reef and the nearshore station.

High reflection near the shoreline, together with cross-shore spectral patterns consistent with the expected locations of nodes and antinodes, indicates the development of standing LF waves across the reef flat. The reflection coefficient decreased offshore, suggesting that the wave field becomes more progressive in character towards the reef crest.

Individual events showed indications of a resonant VLF response consistent with an open-ended basin configuration of the reef flat. However, VLF energy was also present when no such resonant signature was observed. This suggests that resonance alone cannot fully explain the VLF energy on the reef flat. Other generation mechanisms, such as non-linear interactions between IG components, may therefore contribute as well, but require further investigation.

The run-up observations showed that wave set-up formed the largest contribution at $65.9\,\%$, while the IG band dominated the oscillatory part at $28.6\,\%$, against $3.3\,\%$ for GW and $2.2\,\%$ for VLF. Moreover, the $2\,\%$ exceedance run-up level was approximately $28\,\%$ higher than the corresponding surface-elevation level close to the shoreline. This indicates that nearshore water-level measurements may underestimate the water levels reached at the shoreline.

Overall, the results show that LF wave heights at La Saline are strongly linked to offshore GW forcing and water levels over the reef, while their spatial structure is shaped by (partly) standing-wave patterns. These LF motions dominate the nearshore wave field and contribute substantially to shoreline run-up. Understanding their full dynamics, including the role of resonance, is therefore important for future flood risk assessment.

Contents

Preface i

Abstract ii

Nomenclature xi

1 Introduction 1
- 1.1 Research context . . . 1
- 1.2 Research problem . . . 2
- 1.3 Research scope . . . 2
- 1.4 Research questions . . . 2
- 1.5 Report outline . . . 3

2 Background 4
- 2.1 Coastal flooding and the role of ecosystems . . . 4
- 2.2 Coral reef types and geomorphological characteristics . . . 5
- 2.3 Infragravity waves (IG) over reefs . . . 6
  - 2.3.1 IG wave generation . . . 6
  - 2.3.2 Standing waves . . . 8
  - 2.3.3 Resonance . . . 9
  - 2.3.4 Two-dimensional IG wave variability . . . 11
- 2.4 Very low frequency (VLF) waves over reefs . . . 13
  - 2.4.1 Relative VLF wave height and energy contribution . . . 13
  - 2.4.2 Conditions of VLF wave generation and amplification . . . 13
  - 2.4.3 Shear instabilities of the alongshore current . . . 14
- 2.5 Research gaps . . . 15

3 Methodology 16
- 3.1 Study area and experimental set-up . . . 16
  - 3.1.1 Study area . . . 16
  - 3.1.2 Sensor set-up and properties . . . 17
- 3.2 Data analysis . . . 18
  - 3.2.1 Pre-processing . . . 19
  - 3.2.2 Surface versus shear waves . . . 20
  - 3.2.3 Spectral analysis . . . 21
  - 3.2.4 Water level parameters . . . 22
  - 3.2.5 Transfer functions . . . 23
  - 3.2.6 Wave direction analysis . . . 23
  - 3.2.7 Standing wave analysis . . . 24
  - 3.2.8 Resonance assessment . . . 25
  - 3.2.9 Run-up analysis . . . 26
  - 3.2.10 Overview of analysis windows . . . 26

4 Results 27
- 4.1 Offshore forcing conditions during measurement period . . . 27
- 4.2 Nature of the low-frequency energy: surface versus shear waves . . . 28
- 4.3 General observations during measurement campaign . . . 31
  - 4.3.1 Spatial variability of bulk hydrodynamic parameters . . . 31
  - 4.3.2 Influence of offshore forcing on $H_{s,IG}$ and $H_{s,VLF}$ . . . 37
  - 4.3.3 Standing patterns . . . 39
  - 4.3.4 Resonance . . . 40

4.4 Detailed observations on 11 July 2024 . . . 44
4.4.1 Hydrodynamic parameters during 11 July . . . 44
4.4.2 Reflection and standing wave patterns . . . 49
4.4.3 Run-up . . . 52

5 Discussion **53**
5.1 Limitations . . . 53
5.1.1 VLF band limit choice . . . 53
5.1.2 Spectral uncertainty and its propagation into the derived parameters . . . 53
5.1.3 Limitations of the velocity-based analyses . . . 54
5.1.4 Fundamental mode estimation and peak frequency comparison . . . 54
5.1.5 VLF wave shape . . . 54
5.2 Offshore GW-driven, LF-dominated reef hydrodynamics . . . 55
5.3 Spatial structure of the LF wave field . . . 55
5.4 Resonance in the enclosed-basin formulation . . . 56
5.5 Possible VLF generation mechanisms . . . 56
5.5.1 Resonance . . . 56
5.5.2 Non-linear LF interactions . . . 58
5.6 Shoreline run-up . . . 58

6 Conclusions and recommendations **60**

References **62**

A Sensor metadata **66**

B Pre-processing examples **67**

C Wave Set-up **69**

D Run-up and Water Level Decomposition **71**

E Longshore hydrodynamic parameters **74**

F Cross-shore spectral evolution **75**

G IG resonance assessment **77**

H Additional spectra **78**

I Standing wave analysis on 11 July 2024 **80**

J IG peaks frequency difference on 11 July 2024 **82**

List of Figures

1.1 Overview of wave interactions with coral reefs and reef flats, and the transformation of wave characteristics as they propagate towards the island (Kench 2025). 1

2.1 Schematic representation of the components contributing to shoreline total water level, including tides, longer-term mean sea-level variability, storm surge, and wave run-up. Wave run-up consists of wave set-up and swash motions at the shoreline. Adapted from Lowe (2021). 5
2.2 General reef geomorphology and the three main reef types: fringing reef, barrier reef, and atoll (Watanabe and Nakamura 2019). 6
2.3 Sinusoidal waves with slightly different periods forming wave groups and a bound long IG wave (Bertin et al. 2018). 7
2.4 Illustration of the breakpoint forcing mechanism, with a shoreward and seaward free IG wave generated in the surfzone and an outgoing free long wave (OFLW) (Dongeren et al. 2016). 7
2.5 IG wave propagation on a fringing reef. An incident sea-swell (SS) group, the band referred to as GW in this report, generates a bound IG wave that propagates shoreward with the wave group. Upon short-wave breaking in the surf zone, the bound IG wave is released as a free IG wave. In addition, the breakpoint forcing mechanism generates both outgoing and incoming free IG waves. Free IG waves may reflect at the reef crest and the beach (Buckley et al. 2018). 8
2.6 Standing wave profiles and resonant modes in a basin of uniform depth, adapted from Sabatier (2007). (a) General standing wave profile (1) and the associated water particle motion (2). (b) Enclosed basin, reflecting at both boundaries, with a fundamental mode of wavelength $L_0 = 2\ell_B$ (node at the centre, antinodes at both boundaries) and the second and third modes below. (c) Open-ended basin, reflecting at one boundary and open at the other, with a fundamental mode of wavelength $L_0 = 4\ell_B$ (antinode at the reflecting boundary, node at the open end) and the higher odd harmonics below. 10
2.7 Approximate ray trajectories of edge waves for modes 2, 5, and 8, for an edge-wave frequency of $0.02\,\mathrm{Hz}$ and a beach slope of $\beta = 0.01$. The horizontal axis shows the cross-shore distance from the shoreline ($x = 0$), and y denotes the alongshore direction. Adapted from Herbers et al. (1995). 11
2.8 Conceptual model of the combined cross-shore and alongshore standing IG wave pattern over an alongshore-variable bathymetry, proposed by Winter et al. (2017). (a) Surface elevation field, with red and blue marking positive and negative elevation and thus regions in antiphase ($\pm 180°$), resulting from the incident and reflected cross-shore components (bottom arrows) and the oppositely propagating refracted alongshore components (centre arrows). (b) The resulting alongshore and (c) cross-shore standing wave pattern. 12

3.1 Location of La Réunion and indication of La Saline fringing reef (white box), the study site of this project. Figure adapted from Bruch et al. (2022). 16
3.2 Bathymetry and sensor locations at the study site on La Saline fringing reef, projected in WGS 84 / UTM zone 40S (EPSG:32740). Background elevation and depth contours are given relative to the RGR92 datum and are derived from the $40\,\mathrm{cm}$ resolution bathymetric dataset of the HYSCORES project (Ifremer, UBO, Office de l'Eau Réunion) (Mouquet et al. 2016). Red markers indicate the sensor locations, and the dashed line the cross-shore transect. 17

3.3 (a) Detailed top-view of the 160 m wide cross-shore transect relative to the RGR92 vertical datum, using bathymetry data from Jaud et al. (2025). (b) Averaged cross-shore bathymetric profile along the transect. The dotted line denotes the section of the profile where the bathymetry has high uncertainty. 18
3.4 Campaign mean energy density spectra at RS2 and the reef flat sensors (RF7, RF5, RF4, RF3, RF1). 22

4.1 Offshore forcing conditions measured at the reef slope station RS2 over the study period: (a) tide, referenced to RGR92 vertical datum, (b) GW significant wave height $H_{s,GW}$, (c) GW peak period $T_{p,GW}$. 27
4.2 Normalised velocity-to-pressure variance ratio N at ADV3. The left column shows the N time series for the IG (a) and VLF (c) bands from 29 June to 17 July, with the shaded band marking 11 July. The right column shows N against the offshore wave power proxy $P_{Tm01} = H_{s,GW}^2\, T_{m01,GW}$ measured at RS2, for the IG (b) and VLF (d) bands, with the 11 July bursts in red. The dashed horizontal line marks $N = 1$. 28
4.3 Normalised velocity-to-pressure variance ratio N at ADV3 and ADV-lidar on 11 July 2024, for the IG (a) and VLF (b) bands. ADV3 is given per $30\,\mathrm{min}$ burst, and the ADV-lidar over $3\,\mathrm{h}$ windows as well as over the same $30\,\mathrm{min}$ windows as the ADV3 bursts. The dashed horizontal line marks $N = 1$. 29
4.4 Comparison of two ADV3 bursts on 2 July 2024, one with a high VLF ratio ($N = 6.29$, 20:00) and one with a low VLF ratio ($N = 0.57$, 22:00). From top to bottom the rows show the GW-band surface elevation at RS2, the ADV3 mean current, and the IG and VLF band-passed surface elevation η and horizontal velocities. The left column shows the high-ratio burst and the right column the low-ratio burst. 30
4.5 Hydrodynamic parameters at RS2, RF7, and RF1 over the full study period: (a) tide, (b) $T_{m01,GW}$, (c) $H_{s,GW}$, (d) $H_{s,IG}$, (e) $H_{s,VLF}$, (f) wave set-up $\bar{\eta}$ at RF7 and RF1. 32
4.6 Cross-shore evolution of the significant wave height per band, normalised by the value at RF7 ($H_{s,\mathrm{band}}/H_{s,\mathrm{band}}^{\mathrm{RF7}}$). Only $3\,\mathrm{h}$ windows during which all sensors were simultaneously present in the array are included, which covers 27 June–16 August 2024, excluding 22–30 July 2024. Each line is one $3\,\mathrm{h}$ window, coloured by the offshore forcing $P_{Tm01} = H_{s,GW}^2\, T_{m01,GW}$: (a) GW, (b) IG, (c) VLF, and (d) the cross-shore bed profile. 35
4.7 Free-surface elevation and its low-frequency components at (a) RF7, (b) RF4, and (c) RF1 on 3 August 2024 between 01h30 and 01h45, showing the demeaned total free-surface elevation η, the combined IG+VLF component η_{IG+VLF}, and the VLF component η_{VLF}, all on the same vertical scale. The red arrows indicate the maximum of the VLF component, which is $0.12\,\mathrm{m}$ at RF7, $0.13\,\mathrm{m}$ at RF4, and $0.17\,\mathrm{m}$ at RF1. 36
4.8 Observed versus predicted (a–c) $H_{s,IG}$ and (d–f) $H_{s,VLF}$ at RF7, RF1, and ADV-lidar, using the transfer function based on offshore wave power P_{Tm01} and tidal level. Grey dashed line indicates the 1:1 relation. 38
4.9 Mean energy density spectrum at each reef-flat sensor over the study period, with the selected IG-band peak (antinode) and valley (node) frequencies marked by red circles and blue squares, respectively. 39
4.10 Shallow water wavelength of the IG-band peak and valley frequencies at each reef-flat sensor, plotted against distance from the shoreline. Peaks (antinodes) are compared against the $x = L/2$ line and valleys (nodes) against the $x = L/4$ line, both expected for a standing wave with an antinode at the shoreline. 40
4.11 Temporally varying fundamental period T_{node} of the reef flat, for the open-ended basin and closed-basin configurations, over the full deployment period. 41
4.12 $H_{s,VLF}$ at RF1 against the ratio of the offshore VLF peak frequency at RS2 to the open-basin fundamental. (a) shows the raw $H_{s,VLF}$ and (b) shows $H_{s,VLF}$ normalised by the transfer-function prediction $H_{s,VLF}^{TF}$. The four cases examined in more detail are highlighted. 41

4.13 Cross-shore VLF response on 2 August 2024 19:30. (a) shows the energy density spectrum at each reef-flat sensor, with the red line marking the open-ended basin eigenfrequency $f_{node,open} = 0.002\,22\,\mathrm{Hz}$ at that moment. (b) shows the band-integrated $H_{s,VLF}$ (top) and the narrow-band H_{eq} around the RF1 peak frequency (bottom) at each reef-flat sensor. Together they show whether the energy at the eigenfrequency grows toward the shoreline, as expected between a node at the reef crest and an antinode at the shoreline. The offshore peak at RS2 lies at $0.002\,42\,\mathrm{Hz}$ and the RF1 peak at $0.002\,12\,\mathrm{Hz}$, giving ratios to the fundamental of 1.09 and 0.95, respectively. 42
4.14 Cross-shore VLF response on 12 June 2024 01:30. (a) shows the energy density spectrum at each reef-flat sensor, with the red line marking the open-ended basin eigenfrequency $f_{node,open} = 0.002\,10\,\mathrm{Hz}$ at that moment. (b) shows the band-integrated $H_{s,VLF}$ (top) and the narrow-band H_{eq} around the RF1 peak frequency (bottom) at each reef-flat sensor. The offshore peak at RS2 lies at $0.002\,12\,\mathrm{Hz}$ and the RF1 peak at $0.001\,52\,\mathrm{Hz}$, giving ratios to the fundamental of 1.01 and 0.72, respectively. RF7 was not available during this record, so the sensor closest to the reef crest is RF5. 43
4.15 Hydrodynamic parameters at RS2, RF7, and RF1, and the ADV-lidar record near the shoreline (red), on 11 July 2024: (a) tidal level relative to the RGR92 datum, (b) mean GW period $T_{m01,GW}$, the significant wave height in each band, (c) $H_{s,GW}$, (d) $H_{s,IG}$ and (e) $H_{s,VLF}$, and (f) wave set-up $\bar{\eta}$ at the three reef-flat sensors. In (c), and over part of the record in (e), the RF1 (yellow) and ADV-lidar (red) lines coincide. The shaded area marks the near-stationary window (9h–21h) used in the subsequent analysis, during which the mean offshore wave power was $P_{Tm01} = 66.2\,\mathrm{m^2\,s}$. 45
4.16 Mean wave angle $\bar{\theta}$ for the (a) GW, (b) IG, and (c) VLF bands at ADV3, ADV1, and the ADV-lidar on 11 July 2024. For ADV1 and ADV3 each point is a $30\,\mathrm{min}$ burst; for the ADV-lidar the estimates (red) use $3\,\mathrm{h}$ windows, with an additional $30\,\mathrm{min}$ estimate over the same burst windows as the other stations shown as the black dashed line. $\bar{\theta}$ is measured relative to the cross-shore direction (positive values indicate rotation towards the southeast longshore direction). The shaded area marks the near-stationary window (9h–21h). 46
4.17 Cross-shore evolution of (a) significant wave height H_s, (b) peak period T_p, (c) mean wave angle $\bar{\theta}$, (d) mean free surface elevation η relative to the RGR92 datum, and (e) the cross-shore bed profile, averaged over the near-stationary window (9h–21h) on 11 July 2024. The averaging windows differ between bands and stations (Table 3.1), which should be kept in mind when comparing them directly. 48
4.18 Reflection coefficient K_r for the (a) GW, (b) IG, and (c) VLF bands at ADV3, ADV1, and the ADV-lidar on 11 July 2024. For ADV1 and ADV3 each point is a $30\,\mathrm{min}$ burst; for the ADV-lidar the estimates use $3\,\mathrm{h}$ windows, with an additional $30\,\mathrm{min}$ estimate over the same burst windows as the other stations shown as the black dashed line. The shaded area marks the near-stationary window (9h–21h). 49
4.19 Spectra at ADV3 and the ADV-lidar on 11 July 2024: (a) incoming and outgoing spectra at ADV3, (b) incoming and outgoing spectra at the ADV-lidar, (c) total, incoming, and incoming + outgoing spectra at ADV3, and (d) total, incoming, and incoming + outgoing spectra at the ADV-lidar. The spectra are averaged over the 6 ADV3 bursts falling within the near-stationary window (9h–21h), with the same windows applied to the ADV-lidar so that the two stations can be compared directly. 50
4.20 Mean energy density spectrum at each reef-flat sensor and at the ADV-lidar over the near-stationary window (9h–21h) on 11 July 2024, with the identified IG-band peak (red circles) and valley (blue squares) frequencies marked. No peak and valley are marked for the ADV-lidar, since it lies at the shoreline. 51
4.21 Contributions of the set-up and of the GW, IG, and VLF components to the $2\,\%$ exceedance level of the run-up ($R_{2\%}$) and of the ADV-lidar surface elevation ($\eta_{2\%}$), 11 July 2024, 13h–14h. The bars start at the offshore still water level (blue dashed line, $-0.08\,\mathrm{m}$ RGR92) and each block gives the contribution of that term in metres. The red number above each bar is the total $2\,\%$ exceedance level relative to the still water level. The dotted line marks the RGR92 vertical datum. 52

5.1 $H_{s,VLF}$ at RF1 against the ratio of the VLF peak frequency at RF1 to the open-basin fundamental. (a) shows the raw $H_{s,VLF}$ and (b) shows $H_{s,VLF}$ normalised by the transfer-function prediction $H^{TF}_{s,VLF}$. The highlighted cases are the same as in Figure 4.12, in which the offshore VLF peak frequency at RS2 is used as the reference instead. Whereas the response in that figure is largest near a ratio of one, the response at RF1 peaks at ratios below one. 57
5.2 Steady-state harmonic response of a damped oscillator. (a) Amplitude of the response against the ratio of the forcing frequency to the undamped natural frequency, for increasing damping ratio (ζ). (b) Phase lag of the displacement with respect to the applied force. Adapted from Heinrich and Dufour (2015). 57
5.3 Campaign-mean spectrum (26 Jun–16 Aug 2024, excluding 22–30 Jul 2024) at RF7, RF5, and RF3, with the highest IG-band peak, a smaller secondary IG peak, and their difference frequency marked. 58

B.1 Example of the pressure record cleaning procedure, shown for sensor RF4. Unphysical spikes, identified using a threshold of eight standard deviations of the hourly running mean, are shown alongside the resulting cleaned record. 67
B.2 Example of the ADV velocity pre-processing procedure. The raw signal is shown alongside the result after each successive filtering step: the running standard deviation filter, the correlation-based filter (correlation threshold of 80%), and the phase-space despiking method of Goring and Nikora (2002). 67
B.3 Raw run-up signal marking the gaps in the data. 68

C.1 Wave set-up $\bar{\eta}$ across the reef flat over the full study period, shown for all five reef-flat sensors (RF7, RF5, RF4, RF3, RF1) relative to the SWL at RS2. 69

D.1 Decomposition of the run-up R on 11 July 2024. (a) Run-up relative to the RGR92 datum. (b) Record mean R_0 per continuous segment. (c) Offshore still water level $\tilde{\eta}_{\text{tide}}$. (d) Set-up $\bar{R} = R_0 - \tilde{\eta}_{\text{tide}}$. (e–g) GW, IG, and VLF components obtained by band-pass filtering $R - R_0$. The shaded area marks the $1\,\text{h}$ window (13h–14h) used for the $2\,\%$ exceedance levels. 72
D.2 Decomposition of the surface elevation η at the ADV-lidar over the same window as Figure D.1. (a) Surface elevation relative to the RGR92 datum. (b) Record mean η_0 per continuous segment. (c) Offshore still water level $\tilde{\eta}_{\text{tide}}$. (d) Set-up $\bar{\eta} = \eta_0 - \tilde{\eta}_{\text{tide}}$. (e–g) GW, IG, and VLF components obtained by band-pass filtering $\eta - \eta_0$. The shaded area marks the $1\,\text{h}$ window (13h–14h) used for the $2\,\%$ exceedance levels. 73

E.1 Longshore hydrodynamic parameters at RF3, RF3a, and RF3b over the full study period: (a) water depth h, (b) $H_{s,GW}$, (c) $H_{s,IG}$, (d) $H_{s,VLF}$. 74

F.1 (a, c, e) Temporal evolution and (b, d, f) mean energy density spectrum at RS2, RF7, and RF1. Red boxes mark the period used for the mean spectrum. (g) Mean energy density spectra of RS2, RF7, and RF1, zoomed to the VLF and IG bands, illustrating that at RS2 comparable IG energy is already present relative to RF1. 76

G.1 $H_{s,IG}$ against the ratio of each sensor's own IG peak frequency to the closed-basin eigenfrequency, per reef-flat sensor. The left column shows the raw $H_{s,IG}$ and the right column shows $H_{s,IG}$ normalised by each sensor's own transfer-function prediction $H^{TF}_{s,IG}$. 77

H.1 Cross-shore VLF response on 3 August 2024 01:30. (a) shows the energy density spectrum at each reef-flat sensor, with the red line marking the open-ended basin eigenfrequency $f_{node,open} = 0.002\,11\,\text{Hz}$ at that moment. (b) shows the band-integrated $H_{s,VLF}$ (top) and the narrow-band H_{eq} around the RF1 peak frequency (bottom) at each reef-flat sensor. The offshore peak at RS2 lies at $0.001\,52\,\text{Hz}$ and the RF1 peak at $0.000\,91\,\text{Hz}$, giving ratios to the fundamental of 0.72 and 0.43, respectively. 78

H.2 Cross-shore VLF response on 11 July 2024 16:30. (a) shows the energy density spectrum at each reef-flat sensor, with the red line marking the open-ended basin eigenfrequency $f_{node,open} = 0.001\,89\,\mathrm{Hz}$ at that moment. (b) shows the band-integrated $H_{s,VLF}$ (top) and the narrow-band H_{eq} around the RF1 peak frequency (bottom) at each reef-flat sensor. The offshore peak at RS2 lies at $0.002\,42\,\mathrm{Hz}$ and the RF1 peak at $0.000\,61\,\mathrm{Hz}$, giving ratios to the fundamental of 1.28 and 0.32, respectively. 79

I.1 Shallow water wavelength of the IG-band peak and valley frequencies at each reef-flat sensor over the near-stationary window (9h–21h) on 11 July 2024, plotted against distance from the shoreline. Peaks (antinodes) are compared against the $x = L/2$ line and valleys (nodes) against the $x = L/4$ line, both expected for a standing wave with an antinode at the shoreline. 80

I.2 Cross-shore structure of the wave height H_{eq} associated with each sensor's peak frequency over the near-stationary window (9h–21h) on 11 July 2024. Each panel uses the peak frequency identified for that sensor and shows the profile across the whole array, with the sensor's own position marked by a star. The vertical axis is the same in every panel. 81

J.1 Mean spectrum on 11 July 2024 at RF7, RF5, and RF3, with the highest IG-band peak, a smaller secondary IG peak, and their difference frequency marked. 82

List of Tables

2.1 Phase relationships between IG surface elevation η and horizontal velocities (u cross-shore, v alongshore) used to distinguish leaky IG waves and edge waves. CS = cross-shore, LS = alongshore 12

3.1 Analysis window used for each parameter. Where two windows are given for the ADV-lidar, the record was analysed over the longer window and, in addition, over the same $30\,\mathrm{min}$ windows as the ADV bursts, so that the stations can be compared over an identical window length. 26

4.1 Mean band energy fractions at the reef slope (RS2), reef crest (RF7), and mid-reef (RF1), obtained from the mean energy density spectrum, with the standard deviation of the individual $3\,\mathrm{h}$ fractions in parentheses. The last three columns give the change in the absolute band energy relative to RS2. All values are computed over the period during which all stations were simultaneously deployed (27 June to 16 August 2024, excluding the RF7 gap of 22 to 30 July). 33

4.2 Transfer functions for $H_{s,IG}$ at each reef-flat sensor, with the coefficient of determination R^2 and the root-mean-square error (RMSE). The last two columns give the ratio of explained variability attributed to each predictor, as a percentage of the total explained variance. 37

4.3 Transfer functions for $H_{s,VLF}$ at each reef-flat sensor, with the coefficient of determination R^2 and the root-mean-square error (RMSE). The last two columns give the ratio of explained variability attributed to each predictor, as a percentage of the total explained variance. 37

4.4 IG-band peak and valley frequency at each reef-flat sensor. 39

4.5 Mean $\bar{\theta}$ and $\bar{\delta}$ per band and station, averaged over the near-stationary window (9h–21h) on 11 July 2024. The angles are circular means over the doubled angle, since $\bar{\theta}$ defines an axis. 47

A.1 Deployment period, sampling frequency, instrument type, location, and elevation above the bed for each pressure sensor. All deployments took place in 2024. 66

A.2 Deployment details for the Nortek ADV current meters. All deployments took place in 2024. Bed refers to the frame location, used as the sensor's analysis position. Head and bottom coordinates of the ADVs were surveyed separately and were used to determine instrument orientation. Note that the vertical coordinates are expressed as ellipsoidal heights (geodetic heights), rather than as levelled heights relative to the local vertical datum of RGR92. They are presented this way as they were surveyed as such, which avoids a conversion bias when using them directly in the projection of the velocity components. 66

C.1 Elevation of RS2 obtained from the regression against each reef-flat sensor, compared with the adopted value of $-11.67\,\mathrm{m}$. 70

I.1 IG-band peak and valley frequency at each reef-flat sensor over the near-stationary window (9h–21h) on 11 July 2024. At RF1 the second IG peak is used, since its first peak lies at a considerably lower frequency than at the other sensors. 80

Nomenclature

Abbreviations

Abbreviation	Definition
ADV	Acoustic Doppler Velocimeter
FFT	Fast Fourier Transform
GW	Gravity Wave (band)
IG	Infragravity (band)
LF	Low-Frequency (band)
MTR	Mean Tidal Range
PSD	Power Spectral Density
RGR92	Réseau Géodésique de La Réunion 1992 (vertical datum)
RMSE	Root-Mean-Square Error
SWL	Still Water Level
VLF	Very-Low-Frequency (band)

Symbols

Symbol	Definition	Unit
d_s	Elevation of pressure sensor above the bed	[m]
$E(f)$	Energy density spectrum	[m^2/Hz]
E_{inc}	Variance of incident pressure head	[m^2]
E_{ref}	Variance of reflected pressure head	[m^2]
f	Frequency	[Hz]
f_n	Eigenfrequency of mode n	[Hz]
f_p	Peak frequency	[Hz]
g	Gravitational acceleration = 9.81	[m/s^2]
H_s	Significant wave height	[m]
H_{eq}	Narrow-band equivalent wave height	[m]
$H_{s,GW}$	Significant wave height, gravity band	[m]
$H_{s,IG}$	Significant wave height, infragravity band	[m]
$H_{s,VLF}$	Significant wave height, very-low-frequency band	[m]
h	Water depth	[m]
$\bar{h}$	Mean reef-flat water depth	[m]
h_p	Vertical distance from the pressure sensor to the water surface, $h_p = h - d_s$	[m]
K_p	Pressure response factor	[–]
K_r	Reflection coefficient	[–]
k	Wave number	[rad/m]
L	Wavelength	[m]
ℓ_B	Width of the reef flat (basin)	[m]
M	Number of averaged segments per spectrum	[–]
m_n	n-th spectral moment	[m^{2}Hz^n]
N	Normalised velocity-to-pressure variance ratio	[–]
N_s	Number of samples	[–]
n	Mode number	[–]

Symbol	Definition	Unit
P	Pressure	[Pa]
P_{Tm01}	Offshore wave power proxy, $H_{s,GW}^2\, T_{m01,GW}$	[m^{2}s]
R	Run-up	[m]
R_0	Record mean of the run-up	[m]
$\bar{R}$	Set-up component of the run-up, $R_0 - \tilde{\eta}_{tide}$	[m]
R^2	Coefficient of determination	[–]
$R_{2\%}$	2% exceedance run-up level	[m]
$S_\eta(f)$	Surface-elevation energy density spectrum	[m^2/Hz]
T	Wave period	[s]
T_{m01}	Mean wave period (spectral based)	[s]
T_p	Peak period	[s]
T_{node}	Fundamental period of the reef flat	[s]
t	Time	[s]
u	Cross-shore velocity component	[m/s]
$\hat{u}$	Band-passed cross-shore velocity component	[m/s]
v	Longshore velocity component	[m/s]
$\hat{v}$	Band-passed longshore velocity component	[m/s]
x	Cross-shore coordinate (distance from shoreline)	[m]
z_b	Bed elevation relative to datum	[m]
α	Fraction of the velocity variance attributable to shear motions	[–]
Δf	Spectral resolution	[Hz]
$\bar{\delta}$	Directional spread	[–]
η	Free-surface elevation	[m]
$\hat{\eta}$	Band-passed pressure head	[m]
η_0	Record mean of the surface elevation	[m]
$\bar{\eta}$	Set-up component of the surface elevation, $\eta_0 - \tilde{\eta}_{tide}$	[m]
η_{hyd}	Hydrostatic pressure head	[m]
η_{low}	Low-frequency (slowly varying) surface component	[m]
η_{res}	High-frequency residual surface component	[m]
$\tilde{\eta}_{tide}$	Tidal component of the water level	[m]
η_{inc}	Incident pressure head time series	[m]
η_{ref}	Reflected pressure head time series	[m]
$\eta_{2\%}$	2% exceedance surface elevation	[m]
$\bar{\theta}$	Mean wave propagation direction	[deg]
ρ	Seawater density = 1025	[kg/m^3]
σ	Standard deviation	[–]

1

Introduction

1.1. Research context

Climate change is driving more extreme natural events. In tropical regions, this means more intense tropical cyclones, heavier precipitation extremes, and more severe droughts (IPCC 2021). Many low-latitude, low-lying islands are located in areas that are particularly exposed to these hazards, and many of these coasts are bordered by coral reefs. Coral reefs can act as natural coastal barriers because they dissipate incoming wave energy (Ferrario et al. 2014). Their ability to do so depends, among other factors, on bed friction and on the water depth above the reef crest (Figure 1.1). However, rising greenhouse gas concentrations are warming the Earth and its oceans, causing coral reefs to degrade and sea level to rise. Degradation alters bed friction and reduces the reef's capacity to dissipate wave energy, while a higher water level allows more wave energy to propagate across the reef flat. Both can raise the total water level over the reef flat and therefore the resulting wave run-up, the vertical extent reached by waves at the shoreline, and thereby increase the flood risk for low-lying islands (Cheriton et al. 2016; Bruch et al. 2022; Kench 2025).

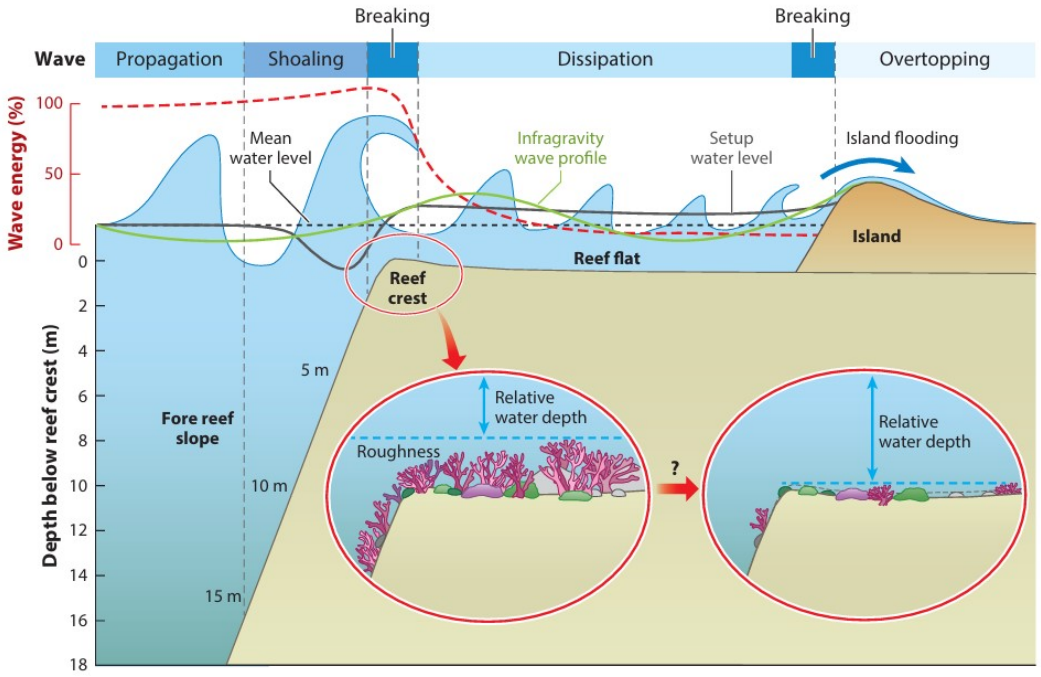


Figure 1.1: Overview of wave interactions with coral reefs and reef flats, and the transformation of wave characteristics as they propagate towards the island (Kench 2025).

1.2. Research problem

Wave motion can be divided into different frequency bands according to its nature, namely gravity waves (GW), infragravity waves (IG), and very-low-frequency waves (VLF), in order of decreasing frequency. GW are the incident sea and swell waves. IG waves are longer-period waves primarily generated by the wave groups of incident GW. VLF waves are the lowest-frequency motions, and the mechanisms responsible for their generation are still relatively poorly understood (Shimozono et al. 2022; Belkadi et al. 2024; Bruch et al. 2022). As incident GW are reduced over the reef, the relative importance of the low-frequency (LF) components increases. In this sense, the reef acts as a low-pass filter, in which the GW are strongly reduced while the IG and VLF components can dominate water-level variability on the reef flat (Bruch et al. 2022; Cheriton et al. 2016).

Fringing reefs are characterised by shallow reef platforms that are directly attached to the bordering coast, with reef flats typically less than $2\,\mathrm{m}$ deep (Kennedy and Woodroffe 2002). They are particularly of interest because their narrow and shallow geometry can result in large wave set-up and run-up at the shoreline (Bruch et al. 2022).

Given this dominance of the LF waves and the importance of assessing them on fringing reef systems, the present study addresses both the IG and VLF components in such an environment in order to understand the dynamics of the LF part of the spectrum. It aims to quantify the contribution of LF waves to water-level variability and to examine the processes that govern them.

1.3. Research scope

This study was carried out within the framework of the FUTURISKS project, which focuses on improving the understanding and prediction of coastal hazards along vulnerable coastlines under changing climate conditions. In this context, Bruch et al. (2022) studied wave transformation, set-up, and run-up across the La Saline fringing reef, located on the microtidal western coast of La Réunion Island. The present work uses the same study site and partly builds on their work. Although the broader objective is to contribute to the assessment of coastal submergence, this study focuses on water levels over the reef flat and on the drivers of LF waves. In particular, the physical mechanisms responsible for LF generation and amplification are considered, including the roles of longshore dynamics, wave reflection, and resonance. A full quantification of wave run-up therefore falls outside the main focus, although run-up is considered to a limited extent.

LF motions over a reef flat can arise from different hydrodynamic processes. Surface waves are characterised by a dynamic coupling between velocity and free-surface elevation, whereas other motions may show strong velocity fluctuations with only a limited surface response. This study focuses on understanding the hydrodynamics associated with the surface-wave component of LF variability.

Furthermore, Bruch et al. (2022) showed that the one-dimensional XBeach Surfbeat model reproduced GW and IG wave transformation and set-up reasonably well, but underestimated VLF wave heights on the reef flat, especially during the most energetic wave events. This motivates further research into the contribution and driving mechanisms of VLF waves to improve the understanding of their dynamics. Numerical modelling itself, however, is outside the scope of the present study.

1.4. Research questions

The main research question is: *What processes and conditions influence the magnitude of IG and VLF waves over a fringing reef?* To answer this question, the following sub-questions are considered:

1. *How do offshore wave conditions and local water depth influence IG and VLF wave heights across the reef flat?*
2. *How do GW, IG, and VLF wave properties evolve in the cross-shore and longshore directions?*
3. *Do standing-wave patterns occur on the reef flat, and if so, what is their spatial signature?*
4. *What physical mechanisms drive the generation and amplification of VLF waves on the reef flat?*

1.5. Report outline

This report is organised as follows. Chapter 2 provides the background on coastal flooding and the role of ecosystems, on coral reef types and their geomorphological characteristics, and on wave transformation and the behaviour of IG and VLF waves over fringing reefs, and identifies the remaining research gaps. Chapter 3 describes the study area and the experimental set-up, and the methods used to process the pressure, velocity, and run-up measurements. Chapter 4 presents the results, covering the observed oceanic conditions, the influence of the offshore forcing and the water level on the LF wave heights, the cross-shore evolution of the wave field up to the shoreline, and the physical processes governing the LF response. Chapter 5 discusses these results in the context of earlier work and addresses the limitations of the study. Chapter 6 answers the research questions and gives recommendations for further research.

2

Background

This literature review provides the theoretical foundation required to address the research questions defined in Chapter 1 and places the present study within the broader context of reef-fronted coastlines. The main purpose of this review is to establish the current state of knowledge on wave transformation processes over reef systems, with particular emphasis on fringing reefs and LF dynamics.

Building on the broader discussion of coastal flooding and ecosystem-based coastal protection, this review focuses specifically on coral reefs. The geomorphological characteristics of coral reefs and their classification are introduced first. The generation and evolution of IG waves over reefs are then reviewed, followed by a discussion of VLF wave dynamics, including resonant behaviour, and the current understanding of the conditions under which extreme VLF wave heights develop. Finally, research gaps related to VLF wave generation, amplification, and spatial variability over fringing reefs are discussed.

Throughout this review, waves are classified into frequency bands following Bruch et al. (2022) (GW, IG and VLF). The boundaries between these bands are not fixed but are generally defined from the local minima observed in the energy spectra, and they therefore differ between studies. Bruch et al. (2022) adopt limits of 0.04–0.25 Hz for GW, 0.004–0.04 Hz for IG, and 0.0006–0.004 Hz for VLF, whereas Shimozono et al. (2022) use 0.04–0.2 Hz, 0.005–0.04 Hz, and 0.002–0.005 Hz, and Gawehn et al. (2016) use 0.04–0.2 Hz, 0.005–0.04 Hz, and 0.001–0.005 Hz for the GW, IG, and VLF bands, respectively. These differences should be kept in mind when directly comparing results across studies.

2.1. Coastal flooding and the role of ecosystems

As described in Chapter 1, climate change is increasing the risk of flooding of coastal regions. Coastal flooding occurs when the total water level at the shoreline exceeds the crest elevation of the coast. This total water level is influenced by several processes, including tides, longer-term mean sea-level variability, storm surge, and wave-driven water-level fluctuations (Figure 2.1). The wave-driven component is referred to as wave run-up, which is defined as the sum of wave set-up and swash oscillations. Wave set-up is the increase in mean water level caused by wave breaking, whereas swash oscillations describe the time-varying uprush and backwash of individual waves at the shoreline (Stockdon et al. 2006).

Over the past decades, there has been substantial growth in the proposed use of ecosystem features for coastal protection, as ecosystems can help mitigate coastal hazards such as flooding and erosion. Two important physical mechanisms responsible for this protective behaviour are wave attenuation through drag dissipation and through wave breaking. Examples of such ecosystems include kelp forests, seagrass meadows, coral reefs, mangroves, and salt marshes, which can attenuate waves through one or both of these processes (Lowe 2021).

Drag dissipation is frequency-dependent, with higher-frequency waves generally being more strongly attenuated because they induce larger velocity gradients and greater frictional losses within the vege-

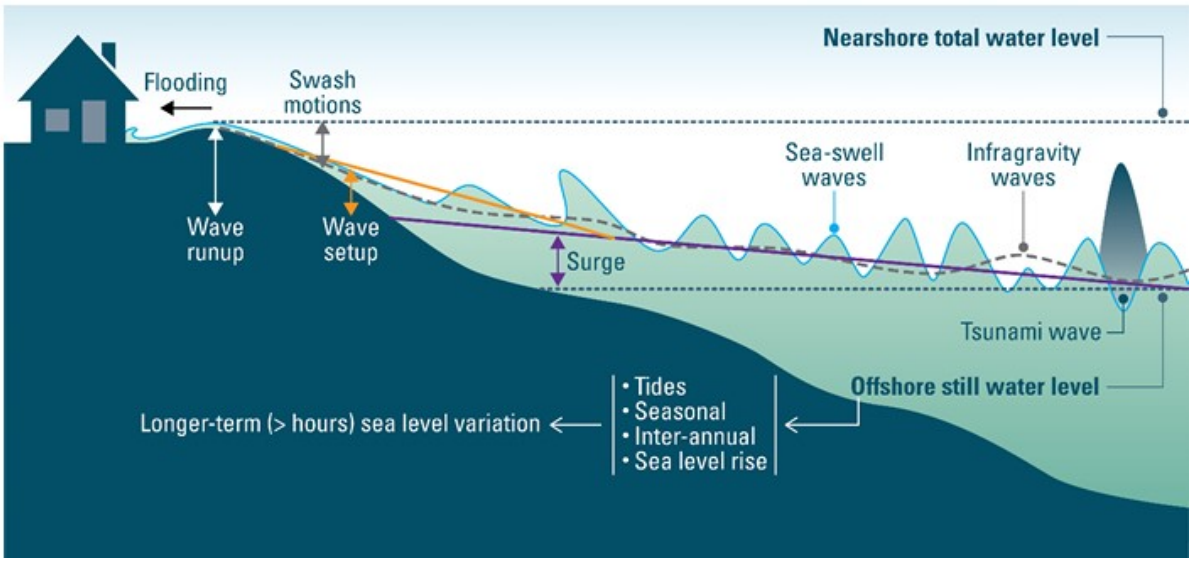


Figure 2.1: Schematic representation of the components contributing to shoreline total water level, including tides, longer-term mean sea-level variability, storm surge, and wave run-up. Wave run-up consists of wave set-up and swash motions at the shoreline. Adapted from Lowe (2021).

tation or roughness elements (Lowe et al. 2007). In addition, wave breaking over steep and shallow ecosystems, such as coral reefs, can effectively dissipate incident GW energy. Observations summarised by Ferrario et al. (2014) show that coral reefs reduce wave energy by an average of $97\,\%$, most of which is dissipated at the reef crest (on average $86\,\%$), where bathymetric changes lead to wave breaking and a subsequent reduction in wave height. However, part of this energy may be transferred into other forms, including enhanced wave set-up, increased LF wave heights, and mean currents, which can still contribute to increased flood risk and erosion (Lowe 2021).

2.2. Coral reef types and geomorphological characteristics

Coral reefs can be classified according to their geomorphological relationship with the adjacent coast into three main types, namely fringing reefs, barrier reefs and atolls. Fringing reefs are the most common reef type worldwide. They are directly attached to the shoreline and, owing to their geometry, can generate some of the highest shoreline water levels among reef types (Bruch et al. 2022). In contrast, barrier reefs are separated from land by a lagoon, and atolls are formed when a fringing reef continues to grow upward from a sunken volcanic island, forming a ring-shaped island that encircles a lagoon (National Oceanic and Atmospheric Administration (NOAA) 2024). These three main coral reef types are illustrated in Figure 2.2, together with the typical geomorphological structure of a coral reef. Roughly three parts can be defined within the coral reef profile, namely the outer reef (or reef slope), the reef flat (including the reef crest), and the inner reef (or lagoon). The reef flat and crest form the shallowest part of the reef and are covered by corals, macro-algae, or a combination of both. Wave energy dissipation mainly occurs across the reef crest and reef flat. As a result, the inner reef is generally characterised by lower-energy conditions than the outer reef and often includes a lagoon that can support corals, seagrasses, and mangroves. The outer reef, in contrast, is exposed to higher-energy wave conditions and is typically dominated by corals or algae that can resist stronger hydrodynamic forcing (Watanabe and Nakamura 2019).

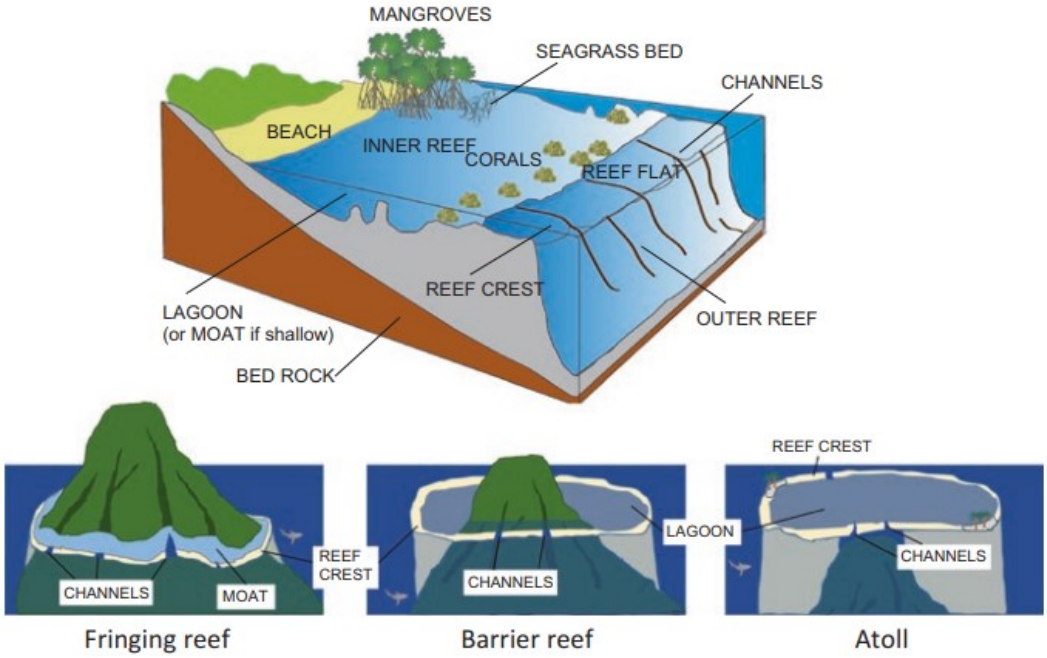


Figure 2.2: General reef geomorphology and the three main reef types: fringing reef, barrier reef, and atoll (Watanabe and Nakamura 2019).

2.3. Infragravity waves (IG) over reefs

IG waves are long-period waves, with frequencies typically between 0.004 and 0.04 Hz. They are generated primarily through non-linear interactions of groups of the incident GW and can be amplified in shallow coastal environments (Bertin et al. 2018; Bruch et al. 2022). This section discusses the generation mechanisms of IG waves. In addition, standing waves and resonance are discussed, together with the study by Winter et al. (2017) on two-dimensional IG wave variability.

2.3.1. IG wave generation

Three IG wave generation mechanisms are commonly described in literature, (i) bound IG waves, (ii) breakpoint forcing, and (iii) bore merging (Bertin et al. 2018). In this section, each mechanism will be described in more detail.

Bound and free IG waves

Ocean waves generally propagate in groups of larger and smaller waves, which can be conceptually understood from a bichromatic wave field (two GW components at discrete frequencies) (Figure 2.3). These short waves travel at slightly different celerities. When they are superimposed, their amplitudes locally reinforce or cancel each other out, resulting in the formation of wave groups. The frequency of these groups is equal to the difference between the frequencies of the two GW components considered. Variations in wave height within these groups cause spatial variations in radiation stresses, with the largest stresses occurring beneath the highest waves. This process is analogous to wave set-up and set-down, where changes in momentum flux are balanced by a pressure gradient, resulting in long-wave motions at the scale of the wave group. The resulting long wave is forced, meaning that it has the wavelength and frequency of the wave group and propagates with the group velocity (Bertin et al. 2018). Longuet-Higgins and Stewart (1962) showed that this mechanism leads to the generation of a bound long wave that is approximately $180°$ out of phase with the GW group envelope. They derived an equilibrium solution that is valid only for a horizontal bed. Over a sloping bottom, this equilibrium no longer holds. As wave groups propagate into shallower water, the phase difference between the wave groups and the bound long wave deviates from $180°$, causing the long wave to lag behind the wave groups. This phase shift allows a transfer of energy from the GW to the bound long wave, leading to

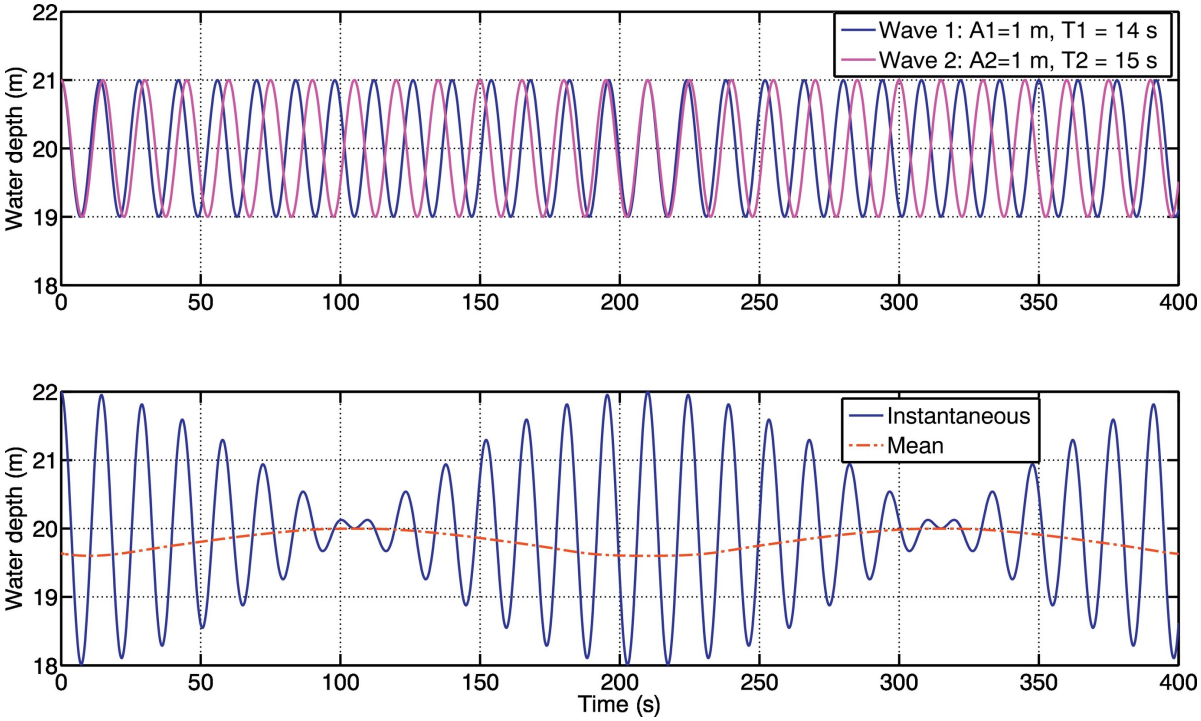


Figure 2.3: Sinusoidal waves with slightly different periods forming wave groups and a bound long IG wave (Bertin et al. 2018).

an increase in IG wave height. This mechanism is dominant for mild bottom slopes (Bertin et al. 2018). When the wave group enters the surf zone, the bound long wave is released following the breaking of the GW. This released wave can propagate independently as a free IG wave. The speed of free IG waves is no longer controlled by the propagation speed of short wave energy, but they propagate at a speed given by the dispersion relation (Bosboom and Stive 2023).

Breakpoint forcing

Symonds et al. (1982) proposed an additional mechanism for IG wave generation, in which the position of the breakpoint varies in time at the timescale of the wave groups. The moving breakpoint induces time-varying radiation stress gradients in the breaking region, which are balanced by corresponding fluctuations in wave set-up. This forcing releases a free long wave that propagates shoreward and a free long wave that propagates seaward, as illustrated in Figure 2.4.

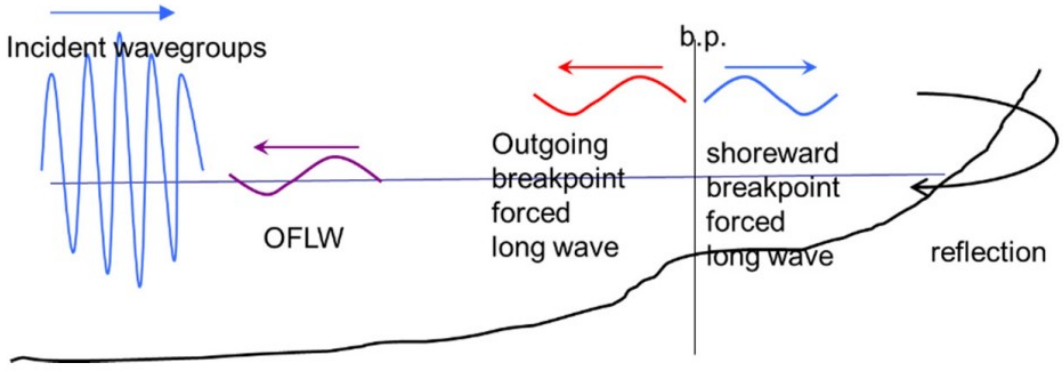


Figure 2.4: Illustration of the breakpoint forcing mechanism, with a shoreward and seaward free IG wave generated in the surfzone and an outgoing free long wave (OFLW) (Dongeren et al. 2016).

Field and numerical results for fringing reefs show that breakpoint forcing dominates IG wave generation

in such an environment, consistent with the theory that this mechanism becomes increasingly important in steep-slope environments (Pomeroy et al. 2012a; Contardo et al. 2025).

Bore merging

After breaking, short waves reorganise in the inner surf zone into bores, that is, breaking wave fronts resembling hydraulic jumps. Bore merging is a non-linear process in which these bores overtake and merge because larger bores propagate faster than smaller ones, a phenomenon known as amplitude dispersion. Bore merging is more likely to occur when the surf zone is wide, which is often the case on gently sloping, dissipative beaches. As a result, the mean wave period increases across the surf zone and energy is transferred from GW to IG frequencies. On gently sloping beaches, however, additional mechanisms besides amplitude dispersion may also play an important role. Tissier et al. (2015) suggested that IG waves can be important for bore merging to take place, because they modulate the local water depth and velocity, causing waves riding on IG crests to propagate faster than those in IG troughs. This strong non-linear interaction between wave fronts and IG waves is, however, still not fully understood. Although bore merging contributes to LF energy in the surf zone, it is generally considered a secondary mechanism for IG wave generation compared to bound waves and moving breakpoints (Bertin et al. 2018).

2.3.2. Standing waves

Once IG waves become free in the surf zone, either through release of the bound wave or through breakpoint forcing, they may lose energy through bottom friction, non-linear energy transfer to the GW band, IG wave breaking, or a combination of these processes. The energy that is not dissipated may be reflected. On a fringing reef this reflection can take place at the shoreline and potentially at other locations such as the reef crest (Figure 2.5). As a result, the IG wave field near the coast is made up of an incoming, shoreward-propagating component and an outgoing, seaward-propagating component. Although reflection and its consequences are described here in the context of IG waves, it is not confined to IG waves and the principles described here may therefore also be applied to the VLF range.

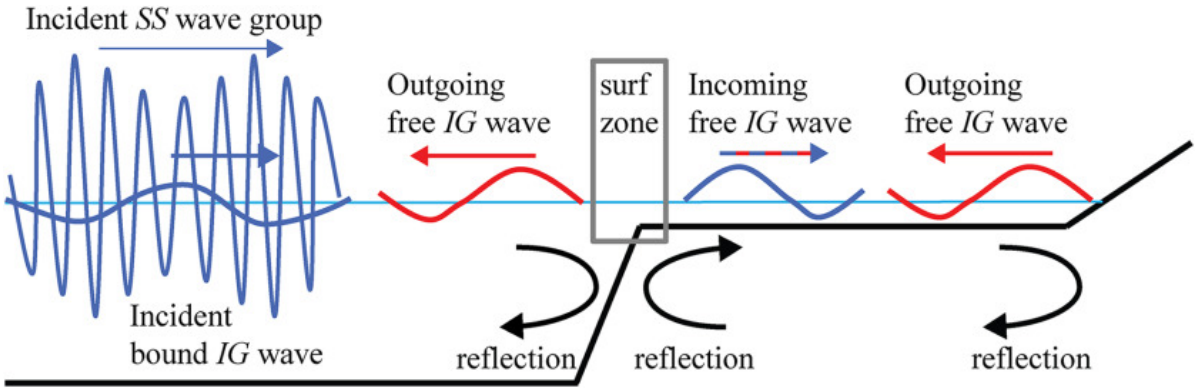


Figure 2.5: IG wave propagation on a fringing reef. An incident sea-swell (SS) group, the band referred to as GW in this report, generates a bound IG wave that propagates shoreward with the wave group. Upon short-wave breaking in the surf zone, the bound IG wave is released as a free IG wave. In addition, the breakpoint forcing mechanism generates both outgoing and incoming free IG waves. Free IG waves may reflect at the reef crest and the beach (Buckley et al. 2018).

Reflection is important because it allows standing waves to develop. A standing wave arises from the superposition of two progressive waves of similar frequency travelling in opposite directions, for example the shoreward-propagating incoming IG wave and its seaward-propagating reflection off the shoreline. Where the two components are of comparable amplitude, their superposition produces a spatial pattern that is fixed in position rather than one that travels across the reef flat (Figure 2.6a). The resulting wave height at each cross-shore position is set by the relative phase difference between the two components, defined as $\delta(x) = \phi_{\text{in}}(x) - \phi_{\text{out}}(x)$. Antinodes, at which the surface elevation variance is largest, form where the components are in phase ($\delta(x) = 0°$), and nodes, at which it is smallest, form where they are out of phase ($\delta(x) = \pm 180°$). Because the positions of the nodes and antinodes are set by the wavelength of the wave and by the location of the reflecting boundary, different

frequencies place their antinodes at different cross-shore positions along the reef flat. How clearly a standing pattern develops depends on how much of the incoming energy is reflected. This is quantified by the reflection coefficient, where a value of 1 corresponds to full reflection. Considering only the cross-shore direction, denoted as x, the reflection coefficient is defined as the square root of the ratio of offshore- to onshore-directed cross-shore IG energy fluxes (Sheremet et al. 2002):

$$K_r = \sqrt{\frac{F^-_{x,IG}}{F^+_{x,IG}}} \tag{2.1}$$

Two approaches exist to separate the incoming and outgoing wave components needed to evaluate Equation 2.1 from collocated surface elevation and cross-shore velocity measurements, namely a time-domain approach and a frequency-domain approach.

Time-domain approach Following Guza et al. (1984), the incoming and outgoing surface elevation time series, $\eta^+(t)$ and $\eta^-(t)$, can be obtained directly from collocated surface elevation $\eta(t)$ and cross-shore velocity $u(t)$ measurements, assuming shallow-water conditions:

$$\eta^{\pm}(t) = \frac{1}{2}\left(\eta(t) \pm u(t)\sqrt{\frac{h}{g}}\right) \tag{2.2}$$

where h is the local water depth and g the gravitational acceleration. The energy of each component follows from the variance of the resulting time series as $E^{\pm} = \rho g \,\mathrm{Var}\left(\eta^{\pm}(t)\right)$, in which ρ is the density of sea water (Bosboom and Stive 2023), so that the reflection coefficient in Equation 2.1 follows as $K_r = \sqrt{E^-/E^+}$.

Frequency-domain approach Alternatively, the incoming and outgoing components can be separated directly in the frequency domain, following Sheremet et al. (2002). The corresponding energy $\mathcal{E}$ of the shoreward- and seaward-propagating components at frequency f and cross-shore position x can be expressed as:

$$\mathcal{E}^{\pm}(f,x) = \frac{1}{4}\left[S_{\eta\eta}(f,x) + \left(\frac{h}{g}\right) S_{uu}(f,x) \pm 2\sqrt{\frac{h}{g}} S_{\eta u}(f,x)\right] \tag{2.3}$$

The associated cross-shore energy flux is defined as:

$$\mathcal{F}^{\pm}(f,x) = \mathcal{E}^{\pm}(f,x)\sqrt{gh} \tag{2.4}$$

Here, $S_{\eta u}$ denotes the cospectrum of η and u, and $S_{\eta\eta}$ and S_{uu} are the autospectra of surface elevation and cross-shore velocity, respectively. Unlike the time-domain approach, this method does not require $\eta^{\pm}(t)$ to be explicitly reconstructed, and yields energy fluxes resolved as a function of frequency. The bulk IG energy fluxes are subsequently obtained by integrating the spectral energy flux over the IG frequency range (Sheremet et al. 2002):

$$F^{\pm}(x) = \int_{f_{low,IG}}^{f_{high,IG}} \mathcal{F}^{\pm}(f,x)\, df \tag{2.5}$$

2.3.3. Resonance

If standing waves are present, resonance may occur depending on several factors. First of all, resonance requires that the frequency of the standing wave coincides with a natural frequency, or eigenmode, of the reef flat. Furthermore, the forcing must result in sufficient energy at a frequency that matches one of the eigenmodes (Péquignet et al. 2009). In addition, the frictional dissipation over the reef flat must be weak enough for the amplitude to build up, since strong bottom friction and wave breaking damp the oscillation, in particular at the higher modes (Gawehn et al. 2016; Shimozono et al. 2022). Because this dissipation is governed largely by the water depth and the width of the reef flat, resonance is most likely at higher water levels and is generally observed at the fundamental mode, that is, the mode with the lowest eigenfrequency (Péquignet et al. 2009; Gawehn et al. 2016).

The way in which a wave is reflected determines how the reef flat behaves as a potential resonator. Where an incoming wave meets a physical boundary such as the shoreline, it can be reflected and an antinode can form at that location. If this occurs at both the shoreline and the reef crest, the reef flat is bounded on both sides and the geometry can act as an enclosed basin, of which the eigenfrequencies are given by (Rabinovich 2009):

$$f_{n,\mathrm{th}} = \frac{n\sqrt{gh}}{2l_B}, \quad n = 1, 2, \ldots, N \tag{2.6}$$

where n is the mode number, g is the gravitational acceleration, h is the water depth over the reef flat, and l_B is the width of the reef flat . The fundamental mode corresponds to $n = 1$.

Reflection, however, need not originate from a solid barrier. Buckley et al. (2018) show that the abrupt change in wave celerity due to the depth change at the reef crest can also partially reflect a wave. Together with the reflection at the shoreline this traps part of the energy on the reef flat, and at a natural frequency the trapped waves arrive in phase with the incoming offshore waves, so resonant amplification can occur. Under this configuration a node forms at the reef crest and an antinode at the shoreline, corresponding to an open-ended basin, of which the eigenfrequencies are given by (Péquignet et al. 2009):

$$f_{n,\mathrm{th}} = \frac{(2n-1)\sqrt{gh}}{4l_B}, \quad n = 1, 2, \ldots, N \tag{2.7}$$

where the symbols are as defined above and the fundamental mode again corresponds to $n = 1$.

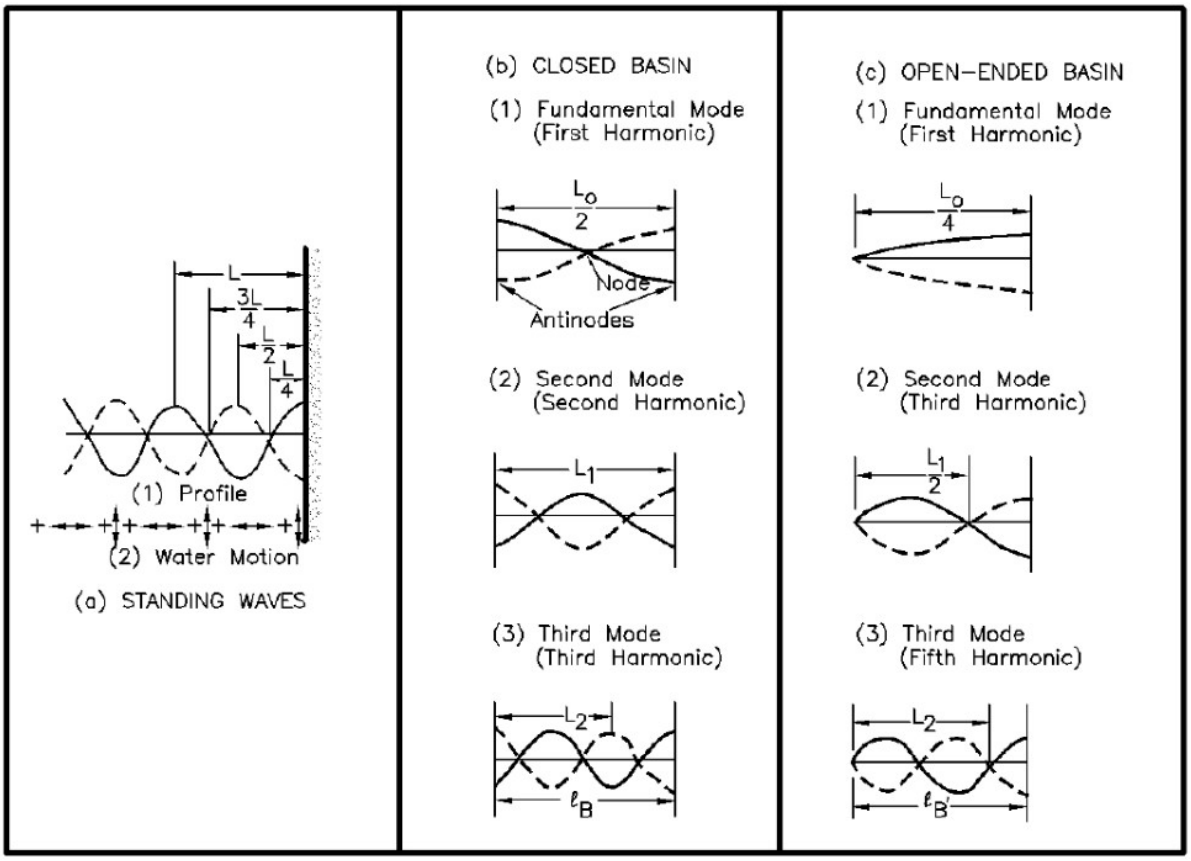


Figure 2.6: Standing wave profiles and resonant modes in a basin of uniform depth, adapted from Sabatier (2007). (a) General standing wave profile (1) and the associated water particle motion (2). (b) Enclosed basin, reflecting at both boundaries, with a fundamental mode of wavelength $L_0 = 2\ell_B$ (node at the centre, antinodes at both boundaries) and the second and third modes below. (c) Open-ended basin, reflecting at one boundary and open at the other, with a fundamental mode of wavelength $L_0 = 4\ell_B$ (antinode at the reflecting boundary, node at the open end) and the higher odd harmonics below.

2.3.4. Two-dimensional IG wave variability

Winter et al. (2017) investigated IG wave dynamics along a rocky reef-fringed coastline with alongshore bathymetric variability. Their study showed that the cross-shore standing pattern persisted along the entire reef despite the alongshore-irregular bathymetry, while the irregularity itself gave rise to a local alongshore standing pattern and to alongshore variability in IG wave height.

The classification of IG wave types in the study is primarily based on phase-lag analysis, which is used to distinguish between standing and progressive wave behaviour. In both the cross-shore and alongshore directions, phase relationships between signals measured by instruments aligned along the same arrays were analysed for this purpose (Winter et al. 2017). The phase lag ϕ was calculated from the cospectrum and quadrature spectrum (C_{ij} and Q_{ij} respectively) that contribute to the cross spectrum between two given instruments i and j (Emery and Thomson 2014):

$$\phi_{ij} = \tan^{-1}\left[\frac{-Q_{ij}(f)}{C_{ij}(f)}\right] \tag{2.8}$$

Progressive IG waves show phase differences between measurement locations that vary continuously with frequency, resulting in a saw-tooth pattern when plotting phase against frequency. In contrast, standing IG waves are characterised by signals that remain either in phase or in antiphase over a broad frequency band (Suhayda 1974).

As described in Section 2.3.2, incident IG waves are commonly reflected at the shoreline, and depending on the local bathymetry and the angle of incidence the reflected energy may either propagate seaward as leaky IG waves or remain confined near the shoreline as edge waves. Edge waves are trapped in the nearshore region through repeated refraction over a sloping seabed combined with shoreline reflection. Their cross-shore structure is described by discrete modal numbers n, which correspond to the number of zero crossings in surface elevation in the cross-shore direction before being refracted. Higher modes extend further offshore (Figure 2.7) (Herbers et al. 1995).

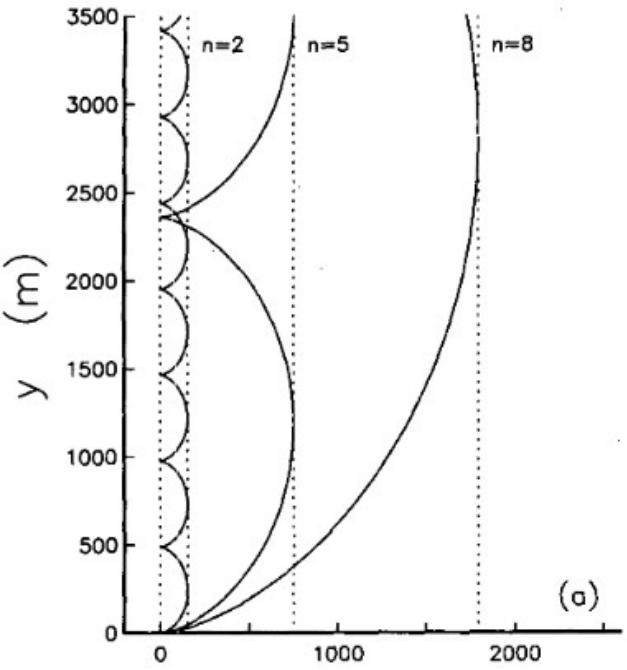


Figure 2.7: Approximate ray trajectories of edge waves for modes 2, 5, and 8, for an edge-wave frequency of $0.02\,\mathrm{Hz}$ and a beach slope of $\beta = 0.01$. The horizontal axis shows the cross-shore distance from the shoreline ($x = 0$), and y denotes the alongshore direction. Adapted from Herbers et al. (1995).

The phase relationships that distinguish these wave types are summarised in Table 2.1. As shown, edge waves are always standing in the cross-shore direction. However, phase relationships alone

do not uniquely distinguish cross-shore standing leaky waves from cross-shore standing edge waves. These wave types differ in their cross-shore amplitude structure, which is sinusoidal for leaky waves but follows a Laguerre polynomial for edge waves. Moreover, edge-wave theory assumes alongshore-uniform bathymetry (Ursell 1952), an assumption that is not satisfied in the case of an alongshore-irregular bathymetry. For this reason, Winter et al. (2017) proposed a conceptual model of cross-shore and locally alongshore standing leaky waves to explain the observed phase relationships.

Table 2.1: Phase relationships between IG surface elevation η and horizontal velocities (u cross-shore, v alongshore) used to distinguish leaky IG waves and edge waves. CS = cross-shore, LS = alongshore

Phase relationship	Leaky IG waves			Edge waves	
	CS + LS progressive	CS standing LS progressive	CS + LS standing	CS standing LS progressive	CS + LS standing
CS array	Nonconstant	$0^\circ / \pm 180^\circ$	$0^\circ / \pm 180^\circ$	$0^\circ / \pm 180^\circ$	$0^\circ / \pm 180^\circ$
LS array	Nonconstant	Nonconstant	$0^\circ / \pm 180^\circ$	Nonconstant	$0^\circ / \pm 180^\circ$
$\Delta\phi(u, v)$	$0^\circ / \pm 180^\circ$	$\pm 90^\circ$	$0^\circ / \pm 180^\circ$	$\pm 90^\circ$	$0^\circ / \pm 180^\circ$
$\Delta\phi(\eta, u)$	0°	$\pm 90^\circ$	$\pm 90^\circ$	$\pm 90^\circ$	$\pm 90^\circ$
$\Delta\phi(\eta, v)$	0°	0°	$\pm 90^\circ$	0°	$\pm 90^\circ$

In this conceptual model (Figure 2.8), the shore-normal components of incident and reflected IG waves form a cross-shore standing wave, similar to that expected over an alongshore-uniform beach. At the same time, refracted IG wave components propagate in opposite alongshore directions and locally form a standing pattern where they intersect over the reef platform. This alongshore standing behaviour is spatially confined and less energetic than the cross-shore mode. In the observations, the cross-shore and alongshore velocity components were $\pm 180^\circ$ out of phase, while surface elevation was $\pm 90^\circ$ out of phase with both velocity components (Table 2.1). Such two-dimensional standing leaky wave patterns are expected to occur preferentially in alongshore-variable environments, where bathymetric irregularities lead to wave refraction, such as along rocky reef-fringed coasts (Winter et al. 2017).

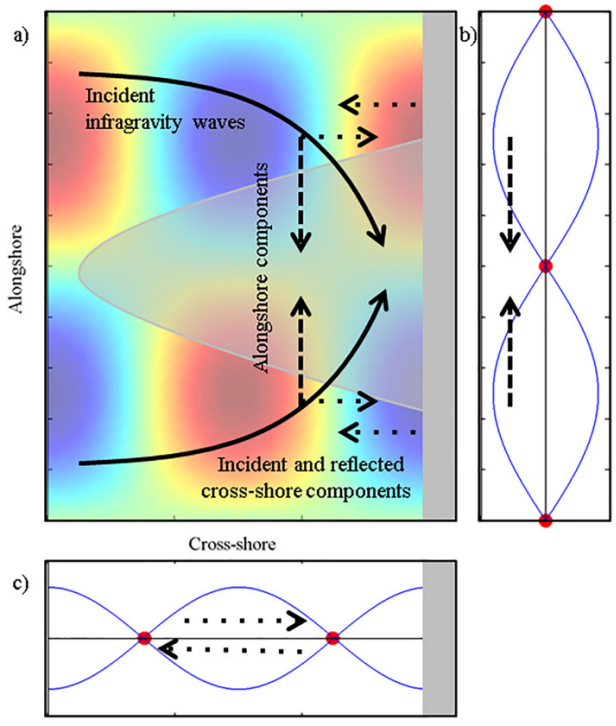


Figure 2.8: Conceptual model of the combined cross-shore and alongshore standing IG wave pattern over an alongshore-variable bathymetry, proposed by Winter et al. (2017). (a) Surface elevation field, with red and blue marking positive and negative elevation and thus regions in antiphase ($\pm 180^\circ$), resulting from the incident and reflected cross-shore components (bottom arrows) and the oppositely propagating refracted alongshore components (centre arrows). (b) The resulting alongshore and (c) cross-shore standing wave pattern.

2.4. Very low frequency (VLF) waves over reefs

VLF waves refer to waves with frequencies ranging from approximately 0.0006 to 0.004 Hz. They have been described as seiche-like, potentially resonant waves that develop and are amplified through non-linear wave transformation associated with wave-breaking processes (Péquignet et al. 2009; Pomeroy et al. 2012b; Shimozono et al. 2022; Cheriton et al. 2016; Bruch et al. 2022; Gawehn et al. 2016; Péquignet et al. 2014). In addition, they have been associated with shear instabilities of the mean alongshore current, which have only a weak signature in the surface elevation (Bowen and Holman 1989; Oltman-Shay et al. 1989).

Several studies have shown that VLF wave heights can account for a substantial fraction of the total wave height on reef flats (Péquignet et al. 2009; Shimozono et al. 2022; Belkadi et al. 2024; Bruch et al. 2022; Cheriton et al. 2016; Gawehn et al. 2016), yet the mechanisms responsible for their generation remain poorly understood. Findings from the literature on VLF wave energy in reef systems are discussed first, focusing on the relative contribution of VLF energy compared to IG and GW energy, followed by the current understanding of the conditions under which VLF waves are amplified over reef systems. In addition, the potential role of shear instabilities of the alongshore current that have also been linked to VLF motions is discussed.

2.4.1. Relative VLF wave height and energy contribution

Bruch et al. (2022) showed that on La Saline fringing reef, dissipation of the GW component across the reef was accompanied by an amplification of LF motions. In the mean offshore spectrum, computed over their full 53-day study period, the IG and VLF components represented approximately $7\,\%$ and $4\,\%$ of the total offshore incident wave energy, respectively. Across the reef flat, IG wave heights increased on average by about $150\,\%$, while VLF wave heights increased by about $260\,\%$, relative to values on the reef slope.

Cheriton et al. (2016) discussed the dominant role of LF waves and resonance along the fringing reef-lined coast of Roi-Namur, where LF waves were found to be the primary contributor to both overwash and shoreline run-up during large offshore wave events. During the largest observed event, IG and VLF wave heights of $1.0\,\mathrm{m}$ and $0.7\,\mathrm{m}$, respectively, were observed at the shoreline. Combined with elevated water levels, the resulting run-up reached $3.7\,\mathrm{m}$ above the toe of the beach at the inner edge of the reef flat, exceeding the height of the beach berm and leading to inundation.

Belkadi et al. (2024) similarly reported, using data from a reef–lagoon system in French Polynesia, that although wave energy was generally concentrated in the IG frequency domain, the energy spectrum could at times be dominated by the VLF range.

2.4.2. Conditions of VLF wave generation and amplification

For flood prediction purposes, it is important to understand under which conditions VLF wave heights amplify. Relevant findings from studies addressing this topic are therefore reviewed in this section, along with a comparison of how different studies have formulated and identified VLF resonance. Where appropriate, these findings are also compared with those for IG waves.

The fundamental frequency of a reef flat under the open-ended basin formulation (Equation 2.7) often falls within the VLF range rather than the IG range. In the section below, where the fundamental mode is referred to in the context of VLF resonance, it refers to the open-ended basin formulation.

Field observations

The field study by Shimozono et al. (2022) addressed the processes governing LF wave generation and dissipation on the southernmost atoll of the Maldives. They found that IG waves commonly develop under energetic conditions and propagate dissipatively across the reef flat. In contrast, large VLF waves are generated more occasionally, typically during the arrival of long-period swells from far-field sources. Because these are less dissipative over the reef flat, those with frequencies corresponding to the fundamental frequency of the reef basin were found to be amplified through resonance.

Bruch et al. (2022) observed a synchronicity between LF wave height variability on the reef flat (IG and VLF wave heights), and GW height variability on the reef slope. Based on this relationship, they suggested that LF wave heights on the reef flat may be primarily controlled by incident swell conditions.

Furthermore, the amplification ratio, defined here as the wave height on the reef flat relative to that on the reef slope, showed tidal modulation for IG waves up to an incident GW height threshold of approximately $2.5\,\mathrm{m}$, with IG wave height on the reef flat increasing with reef water level. Above this threshold, IG waves on the reef flat appeared to be primarily controlled by incident GW conditions rather than by tides. For VLF waves, the amplification ratio exhibited only weak tidal modulation, which became even less pronounced during energetic events.

Regarding the generation mechanisms of extreme VLF wave heights, Bruch et al. (2022) discussed several possible explanations. One possibility is that IG wave energy not dissipated across the reef flat is reflected seaward and may contribute to the formation of resonant VLF waves. In addition, an energy peak was found in the VLF spectrum at $9 \times 10^{-4}\,\mathrm{Hz}$ ($\approx 18.5\,\mathrm{min}$). This timescale is of the same order of magnitude as the period of the first seiche mode, estimated at approximately $15\,\mathrm{min}$ using Equation 2.7 ($n = 1$), based on the reef width ($l_B = 500\,\mathrm{m}$) and the mean reef-flat water depth ($h = 0.5\,\mathrm{m}$). Besides this first mode, Shimozono et al. (2022) suggested that higher-mode resonance may also occur in a fringing reef system, although it is less energetic than the fundamental mode.

Cheriton et al. (2016) further noted that the narrow reef width and low-friction characteristics of the Roi-Namur study site likely enhanced LF wave propagation and resonance on the reef flat. Throughout their study, both IG and VLF wave energies exhibited resonance patterns, particularly across the reef flat, and this resonance occurred more frequently under higher reef-flat water levels. Furthermore, a field study by Gawehn et al. (2016) classified VLF motions on the reef flat into four categories (resonant, standing, progressive-dissipative, and progressive-growing waves) and showed that the largest run-up heights, and ultimately flooding events, coincided with an increased occurrence of resonant VLF waves.

At Ipan reef, Guam, Péquignet et al. (2009) observed that near-resonant LF oscillations dominated the variance of the sea-surface elevation at the shoreline during tropical storm Man-Yi, driven by a storm-induced increase in water level that raised the reef's resonant frequency closer to the timescale of the incident wave-group forcing.

Resonant formulations by different studies

Although several studies have identified VLF resonance on reef flats, the criteria used to do so differ, indicating that its identification is not yet straightforward. The observations of Péquignet et al. (2009) were based on comparing the frequency of the dominant shoreline spectral peak to the theoretical open-ended basin eigenfrequency, noting that this frequency coincided with the timescale of incident wave-group forcing. Building on this approach, Pomeroy et al. (2012b) formalised resonance identification into three explicit indicators, evaluated between two spatially separated locations on the reef flat. These were (1) high coherence in surface elevation, (2) a phase difference close to 0° or 180°, and (3) amplification of the energy spectrum between the reef crest and the shoreline. All three criteria must be satisfied for a wave to be classified as resonant. The identified resonant frequencies were then compared to the same open-ended basin analytical estimate used by Péquignet et al. (2009). Shimozono et al. (2022) extended this comparison, tracking whether the tidally varying theoretical eigenfrequency coincided with the observed spectral peak continuously through time, as the reef water depth changed.

Gawehn et al. (2016) instead defined resonance using a resonance diagram, in which the reef flat is treated as a system forced by incident GW groups, whose envelope was obtained via a Hilbert transform. An energy transfer function between this forcing and the VLF motions on the reef flat was computed, and the frequency at which the transfer peaked, $f_{p,\mathrm{transfer}}$, was compared to the theoretical eigenfrequency $f_{0,\mathrm{th}}$. A VLF wave was classified as resonant when the two coincided. This forms one of four VLF classes distinguished by Gawehn et al. (2016) (resonant, standing, progressive-dissipative, and progressive-growing), identified using a decision tree that combines this resonance diagram with coherence, phase, and shoreward amplitude-growth criteria.

2.4.3. Shear instabilities of the alongshore current

In contrast to surface waves, with gravity being the restoring force, VLF motions have also been attributed to shear instabilities of a mean alongshore current, commonly referred to as shear waves (Oltman-Shay et al. 1989). These instabilities arise from horizontal shear in the alongshore current profile (Bowen and Holman 1989) and are characterised by predominantly rotational, vorticity-dominated motions with a comparatively weak pressure (or surface elevation) signature, in contrast to the largely

irrotational motions of gravity waves (edge and leaky waves) discussed in the preceding sections.

Because both mechanisms can, in principle, produce motions across a range of frequencies, distinguishing their relative contribution is relevant for interpreting the velocity field. Lippmann et al. (1999) proposed the normalised velocity-to-pressure variance ratio:

$$N = \left(\frac{\langle u^2 \rangle + \langle v^2 \rangle}{\langle p^2 \rangle} \right) \Big/ \frac{g}{h} \tag{2.9}$$

as an indicator for this purpose, where u and v are the cross-shore and alongshore velocity components, p is the pressure, and h is the local water depth. Gravity waves are expected to show $N \approx 1$, reflecting an equal partition of kinetic and potential energy independent of the wave mode mix, whereas shear waves, having a comparatively small pressure signature, are expected to show $N \gg 1$. It should be noted that Lippmann et al. (1999) applied this ratio to the IG band (0.004–0.05 Hz) on a sandy, barred beach, not to VLF motions on a reef flat. However, the contrast between pressure-coupled gravity waves and weakly pressure-coupled shear waves is not tied to the IG band or to a sandy beach. The same ratio could therefore, in principle, be applied to VLF motions on a reef flat, to assess whether VLF motions can be attributed to surface waves, shear waves, or a combination of both.

2.5. Research gaps

While IG processes and their generation mechanisms have been well studied and are now quite well understood (Longuet-Higgins and Stewart 1962; Symonds et al. 1982; Bertin et al. 2018), VLF motions remain less clear (Shimozono et al. 2022; Belkadi et al. 2024; Bruch et al. 2022). Observations suggest that large VLF groups are associated with energetic, long-period swell conditions and can substantially contribute to water level variability (Shimozono et al. 2022; Cheriton et al. 2016), yet the processes and parameters controlling these events are not fully understood.

For example, the relative importance of cross-shore energy transfer, reflection and trapping, and dissipation regarding the VLF component along the profile requires further quantification (Bruch et al. 2022; Buckley et al. 2018). Moreover, the influence of offshore wave height, period and direction, together with tidally varying reef-flat water depth, on VLF transformation needs more investigation for fringing reefs (Shimozono et al. 2022; Bruch et al. 2022). This is particularly relevant because resonant VLF motions have been reported to occur predominantly under larger reef-flat water depths and to elevate shoreline water levels (Gawehn et al. 2016; Pomeroy et al. 2012b). In the context of sea-level rise, increased mean reef-flat depths may therefore promote more frequent resonant conditions, potentially increasing shoreline water levels and flood risk (Gawehn et al. 2016).

Most existing studies focus on reef hydrodynamics from alongshore-uniform or quasi one-dimensional analyses along a single cross-shore transect (Bruch et al. 2022). However, alongshore-variable bathymetry can generate LF patterns that are not alongshore uniform (Winter et al. 2017), implying that VLF energy may also depend on reef morphology. As a result, alongshore differences in LF amplification and resonance occurrence may remain unresolved when relying only on one-dimensional transects (Winter et al. 2017). Therefore, it is important to consider both the cross-shore and alongshore direction.

3

Methodology

This study relies on observational data, as field measurements have proven an effective means of studying VLF dynamics over fringing reefs (Péquignet et al. 2009; Cheriton et al. 2016; Shimozono et al. 2022; Bruch et al. 2022; Gawehn et al. 2016). Section 3.1 introduces the study area and the experimental set-up. Section 3.2 then describes the methods used to process the data from pressure and velocity sensors to analyse the wave, reflection, and resonance characteristics of the reef. In addition, the method to process the run-up data is described.

3.1. Study area and experimental set-up

This section introduces the study site and its wave climate, tidal regime, and bathymetry, followed by the sensor set-up in both the cross- and longshore direction.

3.1.1. Study area

The study site is located on the La Saline fringing reef, on the western coast of La Réunion Island in the south-western Indian Ocean (Figure 3.1).

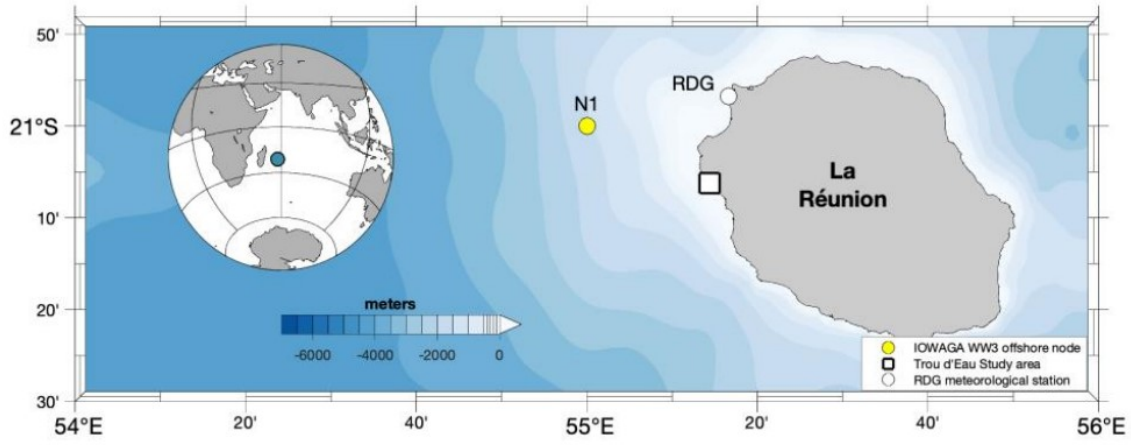


Figure 3.1: Location of La Réunion and indication of La Saline fringing reef (white box), the study site of this project. Figure adapted from Bruch et al. (2022).

La Saline fringing reef forms an $8\,\mathrm{km}$ stretch of convex coastline that narrows progressively toward the north. Over most of its length it maintains a width on the order of $500\,\mathrm{m}$ and fronts a narrow sandy beach (approximately $30\,\mathrm{m}$ wide) with a slope of $\approx$1:10. Cross-shore, the reef separates into a reef flat and a reef slope. The reef flat consists mainly of biodetrital sand punctuated by isolated coral colonies.

The water depth on the reef flat typically ranges between $0.5\,\mathrm{m}$ and $1\,\mathrm{m}$, with its shallowest parts falling dry during spring low tides. The reef slope has a gradient of ≈1:15 and descends toward the fore reef, where an irregular seabed of coral heads, boulders, and spur-and-groove structures extends to about $20\,\mathrm{m}$ depth. The reef crest, the boundary between the reef flat and the reef slope, lies approximately $0.3\,\mathrm{m}$ below mean sea level, and this is the location where incoming GW predominantly break (Bruch et al. 2022).

The reef is situated on the leeward side of the island and is exposed to a distinct seasonal wave climate. Southern Ocean swell, generated by storms at a distance of $3000\,\mathrm{km}$ to $4000\,\mathrm{km}$ from the island (Davy et al. 2016), dominates during the austral winter (April–October). Swell associated with tropical cyclones contributes during the austral summer (November–March) but predominantly affects the island's northern coastline. Based on a 30-year NCEP hindcast, the mean peak wave direction is south-westerly (approximately 225° N), with a peak period of $13.3\,\mathrm{s}$ and a mean significant wave height around $1.9\,\mathrm{m}$, but these values can reach $18.9\,\mathrm{s}$ and $4.2\,\mathrm{m}$ during the most energetic swell events (Bruch et al. 2022). The tidal regime is mixed and primarily semi-diurnal, with a mean tidal range (MTR) of $0.37\,\mathrm{m}$ (Cordier et al. 2013).

3.1.2. Sensor set-up and properties

This study uses pressure, velocity, and video-captured run-up data. Figure 3.2 shows the sensor locations.

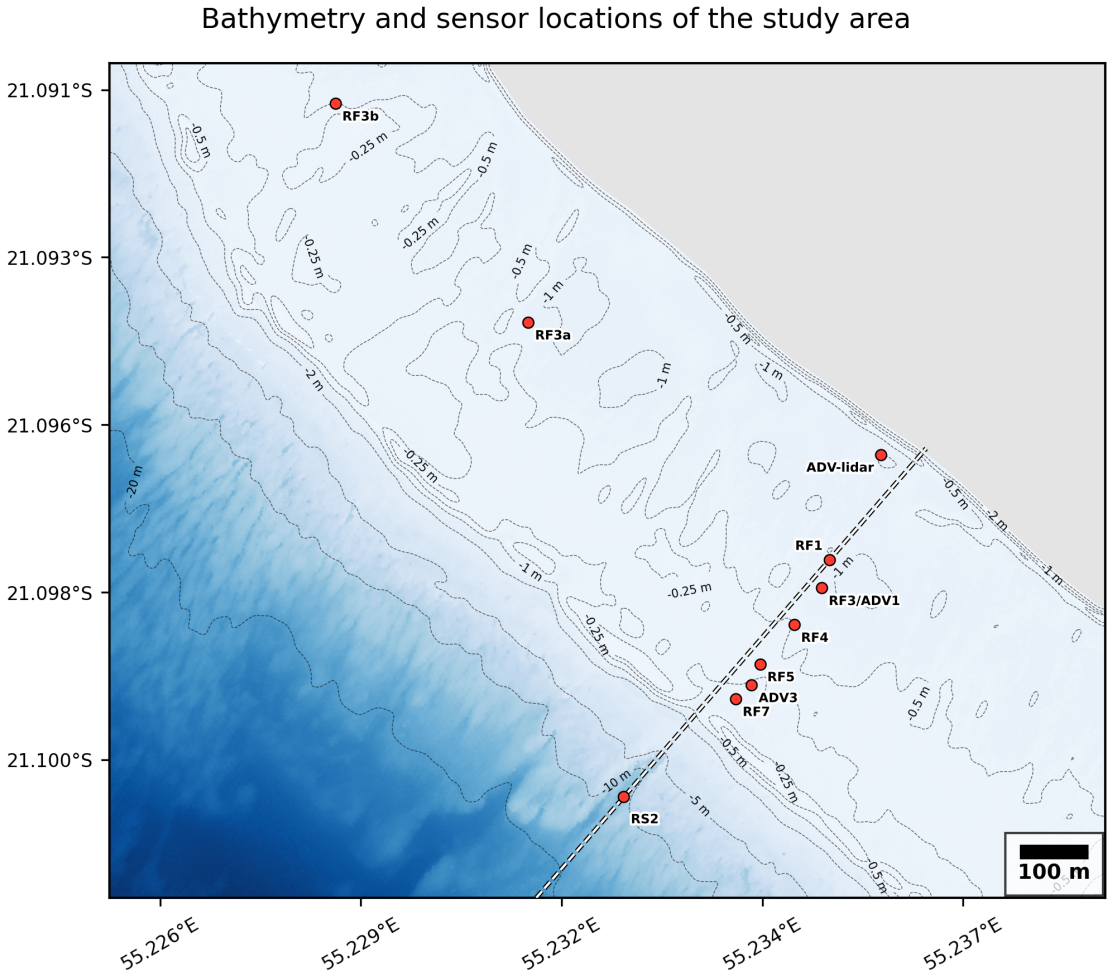


Figure 3.2: Bathymetry and sensor locations at the study site on La Saline fringing reef, projected in WGS 84 / UTM zone 40S (EPSG:32740). Background elevation and depth contours are given relative to the RGR92 datum and are derived from the $40\,\mathrm{cm}$ resolution bathymetric dataset of the HYSCORES project (Ifremer, UBO, Office de l'Eau Réunion) (Mouquet et al. 2016). Red markers indicate the sensor locations, and the dashed line the cross-shore transect.

For detailed data about the sensors, including their exact position, instrument type and brand, deployment period, and sampling frequency, refer to Appendix A. Table A.1 lists the pressure sensors and Table A.2 the velocity sensors. The sensor array consisted of six pressure sensors deployed along a single cross-shore transect spanning the reef slope to the reef flat (RS2, RF7, RF5, RF4, RF3, RF1), measuring between June and September 2024, though not all sensors were deployed over the exact same period. Two additional longshore sensors (RF3a, RF3b) were deployed at approximately the same cross-shore position as RF3, meaning at approximately the same distance from the shoreline. Their distance to the reef crest, however, differed between the three sensors, at approximately $250\,\mathrm{m}$ for RF3, $280\,\mathrm{m}$ for RF3a, and $230\,\mathrm{m}$ for RF3b. The array was complemented by two Nortek ADV current meters (ADV3, ADV1), measuring during July, and a third ADV (ADV-lidar) deployed over roughly the same period as a separate LiDAR and video camera, on 11 July. RS2, the most offshore sensor, was located on the reef slope at a mean depth of approximately $12\,\mathrm{m}$. RF7 was placed closest to the reef crest, marking the transition into the reef flat, with the remaining sensors distributed shoreward across the flat. The pressure sensors recorded continuously throughout their respective deployments, at sampling frequencies ranging from $2\,\mathrm{Hz}$ to $5\,\mathrm{Hz}$ depending on the sensor. The two ADVs were instead operated in burst mode, recording for $30\,\mathrm{min}$ at $8\,\mathrm{Hz}$ every $2\,\mathrm{h}$, while the ADV-lidar sampled continuously at $32\,\mathrm{Hz}$ on 11 July. All times reported in this study are in UTC (local time at La Réunion is UTC$+4$).

Figure 3.3 provides detailed bathymetry information around the cross-shore transect, along with an averaged cross-shore profile, based on Jaud et al. (2025).

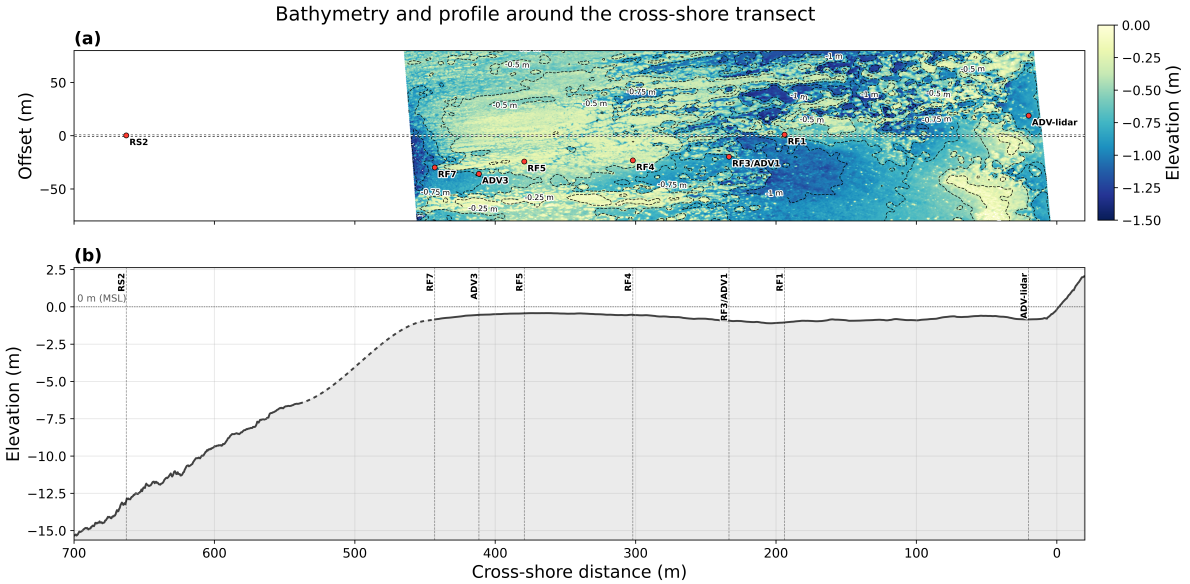


Figure 3.3: (a) Detailed top-view of the 160 m wide cross-shore transect relative to the RGR92 vertical datum, using bathymetry data from Jaud et al. (2025). (b) Averaged cross-shore bathymetric profile along the transect. The dotted line denotes the section of the profile where the bathymetry has high uncertainty.

3.2. Data analysis

The raw pressure, velocity, and run-up records were first corrected and filtered (Section 3.2.1). Section 3.2.2 then describes how the contribution of surface waves relative to shear waves was assessed, Section 3.2.3 how the energy density spectra and the wave parameters were obtained, and Section 3.2.4 how the tidal level and the wave set-up were derived. The relation between the offshore forcing and the reef-flat response was established with transfer functions (Section 3.2.5), the directional properties of the wave field with the band-passed velocity components (Section 3.2.6), and the reflective behaviour of the reef flat by combining pressure and velocity (Section 3.2.7). Section 3.2.8 then describes how resonance over the reef flat was assessed. Finally, Section 3.2.9 describes the analysis of the video-derived run-up.

3.2.1. Pre-processing

The data were first pre-processed so that they could be used directly in the subsequent analyses. The steps involved are described per data set below.

Pressure

The pressure records were first visually inspected, during which unphysical spikes were identified and removed using a threshold of eight standard deviations of the hourly running mean. Figure B.1 in Appendix B shows an example of a pressure record from which spikes were removed. Thereafter, the pressure data were corrected for atmospheric pressure ($P_{\text{corrected}}$) and subsequently converted to a pressure head using:

$$\eta_{\text{hyd}} = \frac{P_{\text{corrected}}}{\rho g} \tag{3.1}$$

where $\rho = 1025\,\mathrm{kg\,m^{-3}}$ is the seawater density and $g = 9.81\,\mathrm{m\,s^{-2}}$ is the gravitational acceleration.

The pressure head was separated into a low-frequency component, containing the tide and set-up, and a wave-induced residual. The low-frequency component, η_{low}, was obtained using a running $1\,\mathrm{h}$ mean of η_{hyd}, while the residual was defined as $\eta_{\text{res}} = \eta_{\text{hyd}} - \eta_{\text{low}}$. The hourly mean was used to determine the mean water depth at each sensor as $h(t) = \eta_{\text{low}}(t) + d_s$, where d_s is the elevation of the sensor above the bed, and to derive the tidal level and wave set-up (Section 3.2.4). The residual was retained for spectral analysis (Section 3.2.3).

Velocity

Raw velocity measurements obtained with an Acoustic Doppler Velocimeter (ADV) are often affected by Doppler noise, signal contamination, and instrument-related vibrations. In addition, spikes may occur due to aliasing of the Doppler signal. Pre-processing is therefore required before the data can be used for further analysis (Nikora and Goring 1998; Chanson 2008). This pre-processing was applied to each of the three velocity components measured by ADV1 and ADV3, and consisted of three steps, namely a running standard deviation filter, correlation-based filtering, and the phase-space despiking method of Goring and Nikora (2002). The ADV-lidar record was provided already processed and rotated into the cross-shore and longshore directions, and was therefore not treated further. An example of a filtered burst, with the points removed at each step highlighted, is shown in Figure B.2 in Appendix B. These three steps are discussed in more detail below.

The first step followed from a visual inspection of the raw signal. Within each $30\,\mathrm{min}$ burst, unphysical spikes were first identified using a threshold of four standard deviations from the burst mean, and replaced by linear interpolation between the neighbouring valid samples.

Signal contamination was subsequently addressed using the correlation coefficient recorded by the ADV for each sample. This coefficient reflects the quality of the acoustic return signal. Samples with a correlation below $80\,\%$ were considered unreliable, removed, and replaced by linear interpolation.

Remaining spikes were identified and removed using the phase-space thresholding method of Goring and Nikora (2002). Each demeaned velocity component was plotted against its first and second derivative, approximated by centred differences between consecutive samples, which yields three projections in which valid samples form a dense cloud while spikes fall outside it. In each projection an ellipse was fitted around this cloud, with its semi-axes set by the universal threshold $\lambda = \sqrt{2\ln(N_s)}\,\sigma$, where N_s is the number of samples and σ the standard deviation of the component. Points falling outside the ellipse were flagged as spikes and replaced by linear interpolation between the nearest valid samples on either side. This procedure was repeated iteratively until no further spikes were detected, up to a maximum of 50 iterations.

The procedure was applied to all three directions of the ADV's own (instrument-frame) coordinate system. These directions then had to be expressed in the cross-shore/longshore/vertical frame, in which the cross-shore direction was defined as the vector from RS2 to RF1 (onshore positive, Figure 3.2) and the longshore direction perpendicular to it (positive southwest). For that purpose, the surveyed head and bottom positions of each instrument were used (Appendix A, Table A.2). For each ADV, the pitch and yaw angles were derived from these surveyed positions. These angles were used to construct rotation matrices, which were applied to the instrument-frame velocity vector to obtain the cross-shore

(u), longshore (v), and vertical (w) velocity components, of which the first two are used in the remaining analysis.

Synchronisation

To separate the incoming and outgoing wave components (Section 3.2.7), the pressure and velocity signals need to be well synchronised. For ADV3 and ADV-lidar, pressure and velocity were recorded by the same instrument and were therefore already synchronised. For ADV1, however, the instrument's own pressure record was not reliable, as within many bursts the recorded pressure repeatedly dropped to zero or showed sudden, unphysical jumps. Although some bursts did show pressure fluctuations consistent with wave motion, the absolute pressure level could not be trusted over the full record. The pressure and water depth from the co-located OSSI sensor RF3 were therefore used instead.

To align the two records in time, the OSSI and ADV pressure signals at RF3 were synchronised separately for each ADV burst, using cross-correlation. Both signals were first resampled to a common sampling frequency of $8\,\mathrm{Hz}$, then standardised by subtracting their mean and dividing by their standard deviation. The standardised signals were cross-correlated over a range of time lags. The lag giving the highest correlation was taken as the time offset between the two records, and this maximum correlation value (normalised by the number of samples) was used as a quality measure of the synchronisation. Only bursts with a maximum correlation of at least 0.9 were kept. For these bursts, RF3's pressure data were shifted by the identified time offset (ranging from $59\,\mathrm{s}$ to $74\,\mathrm{s}$) and matched to the ADV1 velocity timestamps.

Run-up

The provided run-up data were derived from video observations of the shoreline, and expressed as a shoreline elevation time series relative to the RGR92 vertical datum.

The raw signal, including these gaps, is shown in Figure B.3 in Appendix B. To obtain larger continuous segments, small gaps (below a threshold of $3\,\mathrm{s}$) were linearly interpolated. The method used to analyse the run-up data is described in Section 3.2.9.

3.2.2. Surface versus shear waves

To assess the extent to which velocity fluctuations in a given frequency band are associated with surface waves as opposed to shear instabilities of the current, the normalised velocity-to-pressure variance ratio of Lippmann et al. (1999) was computed as:

$$N = \left(\frac{\langle \hat{u}^2 \rangle + \langle \hat{v}^2 \rangle}{\langle \hat{\eta}^2 \rangle} \right) \Big/ \frac{g}{h(t)} \tag{3.2}$$

where $\langle \hat{u}^2 \rangle$, $\langle \hat{v}^2 \rangle$, and $\langle \hat{\eta}^2 \rangle$ are the band-passed cross-shore velocity, longshore velocity, and pressure head variances within the band of interest, and $h(t)$ is the mean water depth at that sensor. For surface waves, for which gravity is the restoring force, the kinetic and potential energy are equally partitioned and $N \approx 1$. Shear waves, by contrast, are rotational motions that develop from the horizontal shear, and show only a small surface-elevation signature relative to their velocity fluctuations, so that $N \gg 1$ where their contribution is significant. A ratio below 1 is not expected for a progressive wave, but can occur for (partially) standing waves near an antinode, where the partitioning between kinetic and potential energy varies with position within the standing-wave pattern (Lippmann et al. 1999).

Assuming statistically independent surface and shear-wave fluctuations, the fraction of the velocity variance attributable to shear motions can be estimated as (Lippmann et al. 1999):

$$\alpha = 1 - \frac{1}{N} \tag{3.3}$$

This fraction is 0 for a pure surface-wave field ($N = 1$) and approaches 1 as the shear contribution dominates ($N \gg 1$).

For ADV3, N was calculated over $30\,\mathrm{min}$ bursts for all frequency bands. For the ADV-lidar, N was calculated over $3\,\mathrm{h}$ windows, and in addition over the same $30\,\mathrm{min}$ windows as the ADV3 bursts. This allowed direct comparison between the stations and assessment of the influence of the shorter analysis window, which is particularly relevant for the VLF band, whose longest periods are not fully resolved within a single burst.

3.2.3. Spectral analysis

This section describes the method used to compute the energy density spectra from the corrected pressure records, the band limit choice based on the average spectra, and the resulting wave parameters.

Energy density spectra

The high-frequency residual η_{res} was used for spectral analysis. Power spectral densities (PSDs) were calculated using Welch's method with a Hamming window and $50\,\%$ overlap. Spectra were computed over consecutive $3\,\mathrm{h}$ windows using $55\,\mathrm{min}$ segments, i.e. nfft $= 55 \cdot 60 \cdot f_s$, where f_s is the sampling frequency of the sensor.

A segment length of $55\,\mathrm{min}$ was chosen to obtain sufficient frequency resolution to resolve the VLF band, and an averaging window of $3\,\mathrm{h}$ to minimise non-stationarity within that window, caused for example by tidal conditions and changing incoming wave conditions. It is acknowledged that this leaves a small number of degrees of freedom (10), and therefore a relatively large error on the individual spectral estimates. This is discussed further in Section 5.1. However, the trade-off was deliberately made in favour of frequency resolution, since the VLF band cannot be resolved with shorter segments. The same segment length and averaging window were used by Bruch et al. (2022) for the IG and VLF bands at this site. In this study these settings were also applied to the GW band. A comparison with the shorter segments and averaging window that Bruch et al. (2022) used for that band showed little effect on the resulting GW parameters, so the same settings were retained for all three bands. However, this choice was made based on the trade-off between resolution and non-stationarity described above. The resulting pressure-derived spectra $S_{\eta_p}(f)$ were corrected for non-hydrostatic pressure attenuation using a pressure response factor $K_p(f)$, following linear wave theory (Bishop and Donelan 1987):

$$S_\eta(f) = \frac{S_{\eta_p}(f)}{|K_p(f)|^2}, \qquad K_p(f) = \frac{\cosh\left(k(f)\, d_s\right)}{\cosh\left(k(f)\, h(t)\right)} \tag{3.4}$$

where d_s is the elevation of the pressure sensor above the bed, $h(t)$ is the mean water depth over the corresponding window, and the wave number $k(f)$ was obtained from the linear dispersion relation (Holthuijsen 2007):

$$(2\pi f)^2 = g k \tanh\left(k\, h(t)\right) \tag{3.5}$$

At high frequencies, k becomes large and K_p approaches zero, which can produce unrealistic amplification of high-frequency energy. To prevent this, the wave number was capped such that the ratio between the vertical distance from the sensor to the water surface, $h_p = h(t) - d_s$, and the wavelength $L = 2\pi/k$ did not exceed a maximum value $(h_p/L)_{\max}$, which corresponds to $k_{\max} = 2\pi (h_p/L)_{\max}/h_p$. A ratio of $(h_p/L)_{\max} = 0.3$ was used, selected as the highest ratio for which no unphysical amplification of the high-frequency spectrum was observed at the reef slope sensor.

Band limit choice

The boundaries between the GW, IG, and VLF bands were determined from the power spectral density at each sensor, averaged over the longest period shared by all sensors (Figure 3.4). These mean spectra were used to identify the local minima that separate each band. The resulting limits were chosen as follows.

- $f_{GW} = [0.04\,\mathrm{Hz}, 0.25\,\mathrm{Hz}]$
- $f_{IG} = [0.0025\,\mathrm{Hz}, 0.04\,\mathrm{Hz})$
- $f_{VLF} = [0.0003\,\mathrm{Hz}, 0.0025\,\mathrm{Hz})$

Given that most of the GW-band energy is present at RS2, with a smaller part remaining at RF7, these two locations were used to determine the GW–IG boundary. Based on the local minima, $0.04\,\mathrm{Hz}$ was chosen for this boundary. This value is consistent with the GW–IG limit of $0.04\,\mathrm{Hz}$ adopted by Bruch et al. (2022) at La Saline fringing reef. Some studies instead define the boundary between GW and IG relative to the peak frequency of the offshore GW, i.e. $f_{p,GW}/2$ (Roelvink and Stive 1989). This study used fixed limits, identical for every time step, so that the energy contained within each frequency range could be consistently compared over time.

For the IG–VLF boundary, the local minimum shifts across the reef flat (Figure 3.4), from $0.0025\,\mathrm{Hz}$ at RF7 and RF5 to $0.004\,\mathrm{Hz}$ at RF1, the latter being the limit adopted by Bruch et al. (2022). This

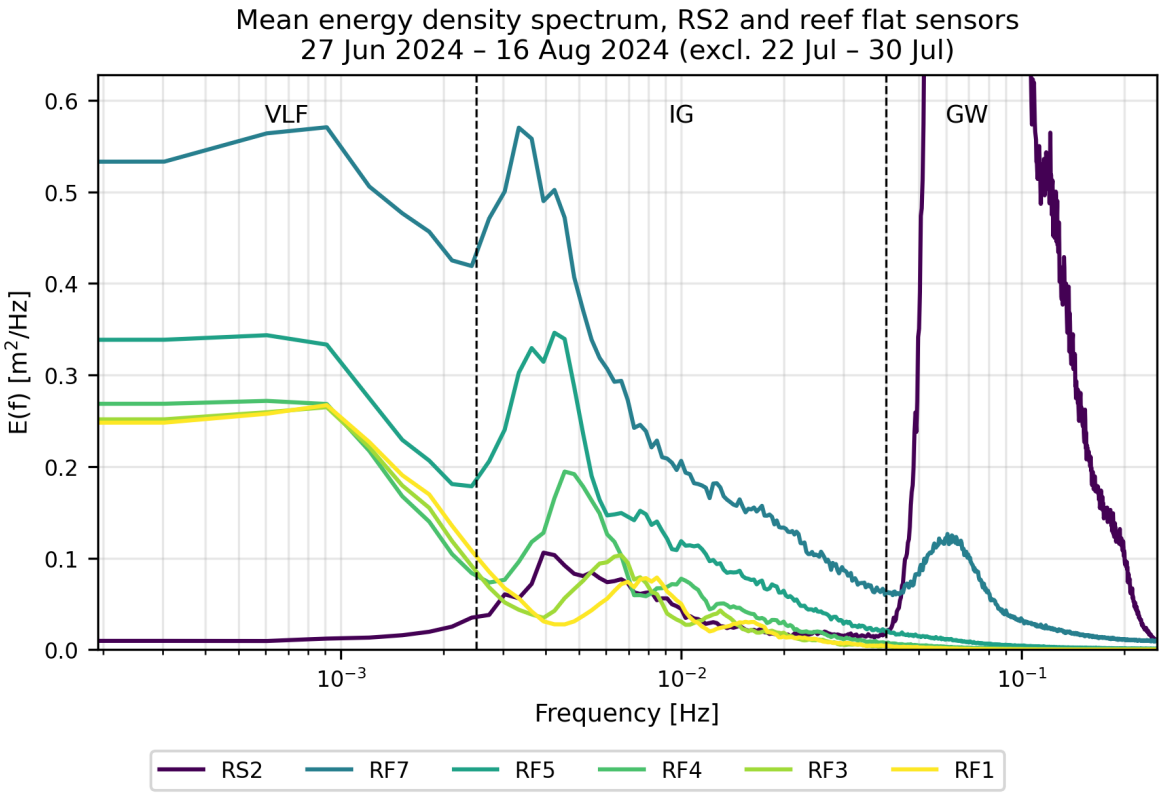


Figure 3.4: Campaign mean energy density spectra at RS2 and the reef flat sensors (RF7, RF5, RF4, RF3, RF1).

shift is attributed to standing wave patterns over the reef flat and is addressed in Section 3.2.7, with the results in Section 4.3.3. The boundary was set at the lowest observed minimum of $0.0025\,\mathrm{Hz}$. A higher limit would include part of the adjacent spectral peak near the reef crest and prevent a consistent comparison across the reef flat.

Furthermore, the lower limit of the VLF band is determined by the spectral resolution, $f = 1/(55 \times 60) = 0.0003\,\mathrm{Hz}$.

Wave parameters

With the band limits defined, the wave parameters for each band (GW, IG, and VLF) were determined from the non-hydrostatically corrected spectrum $S_\eta(f)$ of each individual $3\,\mathrm{h}$ window (Section 3.2.3). The n-th order spectral moment was computed by numerical integration over the band-limited frequency range $[f_{\min}, f_{\max}]$:

$$m_n = \int_{f_{\min}}^{f_{\max}} f^n S_\eta(f)\, df \tag{3.6}$$

The significant wave height was obtained from the zeroth moment as $H_s = 4\sqrt{m_0}$, and the mean period as $T_{m01} = m_0/m_1$. The peak frequency f_p was obtained as the frequency at which $S_\eta(f)$ is maximum within the band, and the corresponding peak period as $T_p = 1/f_p$.

3.2.4. Water level parameters

The tidal level and the wave-induced set-up were determined from the mean water depth $h(t)$ at each sensor. All elevations are referenced to the local vertical datum of RGR92. The water-surface elevation at each sensor was expressed as $z_b + h(t)$, with z_b the bed elevation, obtained from the GNSS-surveyed instrument elevation minus its height above the bed d_s. The elevation of the offshore station RS2 was not surveyed but derived from its nominal deployment depth. This was verified against the regression approach of Vetter et al. (2010) and Bruch et al. (2022), as described in Appendix C.

The tidal level was taken as the offshore still water level (SWL) at RS2:

$$\tilde{\eta}_{\text{tide}}(t) = \text{SWL}_{\text{offshore}}(t) = z_{b,\text{RS2}} + h_{\text{RS2}}(t) \tag{3.7}$$

and assumed spatially uniform across the study area.

The wave set-up at each reef-flat sensor followed as its water-surface elevation minus the offshore still water level:

$$\bar{\eta}(t) = \big[z_b + h(t)\big] - \text{SWL}_{\text{offshore}}(t) \tag{3.8}$$

The resulting set-up across the reef flat is presented in Appendix C.

3.2.5. Transfer functions

To relate the significant wave height of the IG and VLF bands at each sensor to offshore and local variables, transfer functions were constructed using multiple linear regression. The following predictors were tested: the offshore GW significant wave height $H_{s,GW}$, the peak period $T_{p,GW}$, and the mean period $T_{m01,GW}$ at RS2, the wave power proxies $H_{s,GW}^2\,T_{p,GW}$ and $P_{Tm01} = H_{s,GW}^2\,T_{m01,GW}$, and the local water level, represented either by the local water depth, its tidal component, or its wave set-up component. Both individual predictors and combinations of predictors were tested, and the best-performing combination was selected based on the performance metrics defined below.

For a set of predictor variables $x_1, \ldots, x_M$, matched in time to the response variable y, the transfer function takes the form:

$$\hat{y} = \sum_{j=1}^{M} a_j x_j + b \tag{3.9}$$

where the coefficients a_j and intercept b were obtained by least-squares regression of y against the predictors, using only time steps for which both the predictors and the response variable were available.

The performance of each transfer function was evaluated using the coefficient of determination (R^2) and the root-mean-square error (RMSE):

$$R^2 = 1 - \frac{\sum_{j=1}^{N_s}(y_{\text{obs},j} - y_{\text{pred},j})^2}{\sum_{j=1}^{N_s}(y_{\text{obs},j} - \overline{y_{\text{obs}}})^2}, \qquad \text{RMSE} = \sqrt{\frac{1}{N_s}\sum_{j=1}^{N_s}(y_{\text{obs},j} - y_{\text{pred},j})^2} \tag{3.10}$$

where y_{obs} and y_{pred} are the observed and predicted values, respectively, $\overline{y_{\text{obs}}}$ is the mean observed value, and N_s is the number of time steps.

3.2.6. Wave direction analysis

To characterise the directionality of the wave field, the band-passed cross-shore and longshore velocity components were used to estimate the mean propagation direction and the directional spread.

Mean direction

The energy-weighted mean direction was calculated based on Herbers et al. (1999) as:

$$\bar{\theta} = \frac{1}{2}\tan^{-1}\left(\frac{2\langle\hat{u}\hat{v}\rangle}{\langle\hat{u}^2\rangle - \langle\hat{v}^2\rangle}\right) \tag{3.11}$$

where $\langle\cdot\rangle$ denotes an average over the analysis window, and $\hat{u}$ and $\hat{v}$ are the cross-shore and longshore velocity components, respectively, band-pass filtered to the frequency band of interest. In contrast to Herbers et al. (1999), the absolute value in the denominator was omitted to allow the dominant axis of motion to extend beyond $\pm 45^\circ$ from the cross-shore direction.

For ADV1 and ADV3, $\bar{\theta}$ was calculated over $30\,\text{min}$ bursts for all frequency bands. For the ADV-lidar, $\bar{\theta}$ was calculated over $3\,\text{h}$ windows, and in addition over the same $30\,\text{min}$ windows as the ADV1 and ADV3 bursts. This allowed direct comparison between the stations and assessment of the influence of the shorter analysis window.

Directional spread

Correspondingly, the energy-weighted directional spread was calculated as:

$$\bar{\delta} = \left(\frac{\langle \hat{v}'^2 \rangle}{\langle \hat{u}'^2 \rangle + \langle \hat{v}'^2 \rangle} \right)^{1/2} \tag{3.12}$$

where $\hat{u}'$ is the component of band-passed velocity in the direction $\bar{\theta}$, and $\hat{v}'$ is the component perpendicular to $\hat{u}'$ (Herbers et al. 1999). The spread was evaluated over the same windows as the corresponding $\bar{\theta}$.

3.2.7. Standing wave analysis

To evaluate whether the reef flat can support standing-wave behaviour, the mean spectra at the reef-flat sensors were examined first (Figure 3.4). The wavelengths of the peak and valley frequencies in these spectra were determined and compared with the cross-shore geometry of the reef, following the discrete-frequency approach described below. In addition, on 11 July both pressure and velocity measurements were available near the shoreline (ADV-lidar) and closer to the reef crest (ADV3). These were combined to obtain the incoming and outgoing spectra and the resulting wave reflection coefficient using the approach described below.

Discrete frequency analysis

To investigate the wavelength of a discrete frequency, the shallow water wavelength was used:

$$L = \frac{\sqrt{g\bar{h}}}{f} \tag{3.13}$$

with $\bar{h}$ the water depth averaged over the reef-flat profile. This is valid under the assumption that the water depth is small relative to the wavelength, as is generally the case for IG and VLF waves propagating over the reef flat.

The wavelengths of the peak and valley frequencies in the mean spectra were computed and compared with the distance of each sensor from the shoreline. For a standing wave with an antinode at the shoreline, antinodes are expected at $x = L/2,\ L,\ 3L/2, \ldots$ and nodes at $x = L/4,\ 3L/4, \ldots$ from the shoreline, so that a peak frequency at a given sensor should correspond to $x = L/2$ and a valley frequency to $x = L/4$ if this can be attributed to standing waves.

In addition, to examine how the energy associated with a discrete frequency evolves across the reef, the significant wave height corresponding to that frequency was calculated, denoted H_{eq}. It follows the same definition as H_s (Section 3.2.3), but with the integration limited to a bandwidth of twice the spectral resolution around the frequency of interest, so that it represents the energy associated with that single frequency (Henderson et al. 2001).

Incoming and outgoing wave separation

A cross-shore standing wave pattern can only develop when the outgoing wave energy is comparable in magnitude to the incoming energy, that is, when the reflection coefficient approaches 1 (Winter et al. 2017). To determine this coefficient, the pressure and velocity signals were combined to split the record into an incoming and an outgoing component. This requires co-located, synchronised pressure and cross-shore velocity measurements at a common sampling rate. Only the shore-normal direction is considered here, and the limitations of this are addressed in Section 5.1.

The two components were separated following the approach of Guza et al. (1984), in which the incoming and outgoing components are obtained as time series:

$$\hat{\eta}_{\mathrm{inc}} = \frac{1}{2}\left(\hat{\eta}_{\mathrm{res}} + \hat{u}\sqrt{h/g}\right), \qquad \hat{\eta}_{\mathrm{ref}} = \frac{1}{2}\left(\hat{\eta}_{\mathrm{res}} - \hat{u}\sqrt{h/g}\right) \tag{3.14}$$

where $\hat{\eta}_{\mathrm{res}}$ and $\hat{u}$ are the pressure head residual and the cross-shore velocity, band-pass filtered for every band (GW, IG, and VLF), and h is the mean water depth at that sensor over the burst or analysis window.

The time-domain approach was used because the velocity records consist of $30\,\mathrm{min}$ bursts recorded every $2\,\mathrm{h}$, so that the reflection coefficient has to be obtained from an individual burst. For ADV1 and ADV3, the $30\,\mathrm{min}$ burst length was used for all bands. For the continuous ADV-lidar record, $3\,\mathrm{h}$ windows were used, and in addition the same $30\,\mathrm{min}$ windows as the ADV1 and ADV3 bursts, so that the stations can be compared directly and the influence of the shorter window can be assessed.

Following Sheremet et al. (2002), the reflection coefficient was calculated for each burst or window and frequency band as:

$$K_r = \sqrt{\frac{E_{\mathrm{ref}}}{E_{\mathrm{inc}}}} \tag{3.15}$$

where E_{inc} and E_{ref} are the energies of the incident and reflected time series, for which their variances are used as a proxy, as $E_{\mathrm{inc}} \propto \mathrm{Var}(\hat{\eta}_{\mathrm{inc}})$ and $E_{\mathrm{ref}} \propto \mathrm{Var}(\hat{\eta}_{\mathrm{ref}})$.

3.2.8. Resonance assessment

To assess possible resonance, the time-varying fundamental frequency of the reef flat was estimated from the bathymetric profile and compared with the IG and VLF peak frequencies. Two idealised configurations were considered based on the seaward boundary condition. For an open-ended basin, reflection occurs at the shoreline while a node forms at the reef crest (Buckley et al. 2018; Péquignet et al. 2009; Gawehn et al. 2016). The frequency of mode n is then given by:

$$f_n^{\mathsf{open}} = \frac{1}{4}(2n-1)\left(\int_{x_{\mathsf{reef\ crest}}}^{x_{\mathsf{shoreline}}} \frac{dx}{\sqrt{g\,h(x,t)}}\right)^{-1}, \qquad n = 1, 2, 3, \ldots \tag{3.16}$$

For an enclosed basin, both the shoreline and the reef crest act as reflecting physical boundaries, forming an antinode at each boundary (Rabinovich 2009). The frequency of mode n is then given by:

$$f_n^{\mathsf{closed}} = \frac{1}{2}n\left(\int_{x_{\mathsf{reef\ crest}}}^{x_{\mathsf{shoreline}}} \frac{dx}{\sqrt{g\,h(x,t)}}\right)^{-1}, \qquad n = 1, 2, 3, \ldots \tag{3.17}$$

The seaward boundary was taken at the reef crest, where there is a rapid change in slope ($x_{\mathsf{reef\ crest}} = 450\,\mathrm{m}$), and $h(x,t)$ is the mean water depth, consisting of the tide and set-up, as a function of cross-shore position. This was reconstructed for each $3\,\mathrm{h}$ window, matching the temporal resolution of the IG and VLF wave parameters (Section 3.2.3). Within each window, a spatially uniform water level was assumed across the reef flat, taken from the RF1 record. This assumption is consistent with previous reef modelling studies (Lowe et al. 2009) and with the roughly constant wave set-up over the reef flat reported by Vetter et al. (2010), which was also found here (Section 4.3.1). The water level was combined with the fixed cross-shore bed profile (Figure 3.3) to obtain $h(x,t)$ throughout the domain. In both formulations the fundamental frequency is obtained for $n = 1$. This frequency falls in the IG range for the enclosed configuration and in the VLF range for the open-ended configuration (Section 4.3.4).

The response was assessed by comparing, for every spectrum, the peak frequency in the band with the corresponding fundamental frequency and relating this ratio to the band-integrated significant wave height. To separate a resonant response from the offshore forcing, the wave height was also normalised by the transfer-function prediction for that sensor (Section 3.2.5). Records for which the peak frequency coincided with a band boundary without showing a distinct peak were excluded.

For the enclosed configuration, the peak frequency and band-integrated IG response were evaluated at all reef-flat sensors. For the open-ended configuration, the VLF response at RF1 was used. RF1 is the pressure sensor closest to the shoreline, where the open-ended basin antinode and largest response are expected. The offshore VLF peak at RS2 was used as the reference frequency. This peak can represent the offshore VLF forcing of the reef flat. Alternatively, it may represent energy radiated seaward through the open boundary at the reef crest. In both cases, it provides a reference frequency for comparison with the open-basin eigenfrequency.

In addition to the band-integrated response, individual spectra were examined using the narrow-band wave height H_{eq} around the peak frequency at RF1 (Section 3.2.7). This was used to assess whether the cross-shore response shows a node near the reef crest and an antinode towards the shoreline, as expected for the open-ended basin configuration.

3.2.9. Run-up analysis

Wave run-up is the vertical excursion of the waterline relative to the offshore still water level, i.e. in this study the SWL at RS2, and consists of a set-up component and a time-varying swash component (Stockdon et al. 2006). To separate these contributions and to determine the $2\,\%$ exceedance levels, the approach of Pearson et al. (2017) was followed. The video-derived run-up time series R was first split into its record mean and the three band components (GW, IG, and VLF):

$$R = R_0 + R_{GW} + R_{IG} + R_{VLF} \tag{3.18}$$

where R_0 is the mean waterline elevation over the analysis window. The set-up at the shoreline follows from this mean component by subtracting the offshore still water level, defined in Equation 3.7:

$$\bar{R} = R_0 - \tilde{\eta}_{\text{tide}} \tag{3.19}$$

Subsequently, the $2\,\%$ exceedance level of the run-up was determined. Averaging each band component over the time steps at which this level was exceeded gives its contribution to that level, $\overline{R}_{2\%,GW}$, $\overline{R}_{2\%,IG}$, and $\overline{R}_{2\%,VLF}$, determined by:

$$\overline{R}_{2\%} = \frac{1}{0.02N_s} \sum_{j=1}^{0.02N_s} R_j \tag{3.20}$$

where N_s is the number of samples in the record. The index j runs over the samples sorted by descending total run-up, so that the summation covers the highest $2\,\%$ of the record, and R_j is the value of the band component at the corresponding time step. The evaluation window was set to $1\,\mathrm{h}$, starting at the beginning of the longest continuous run-up segment. The same calculation was applied to the surface elevation η measured by the sensor close to the shoreline (ADV-lidar), giving $\eta_{2\%}$ over the same time window as R, together with its components $\bar{\eta}$, $\overline{\eta}_{2\%,GW}$, $\overline{\eta}_{2\%,IG}$, and $\overline{\eta}_{2\%,VLF}$. As run-up is expressed relative to the still water level, $R_{2\%}$ and $\eta_{2\%}$ are reported as the elevation above $\tilde{\eta}_{\text{tide}}$. Adding $\tilde{\eta}_{\text{tide}}$ gives the corresponding elevation relative to the RGR92 vertical datum. The decomposition of both R and η is shown in Appendix D.

3.2.10. Overview of analysis windows

The analyses described in the sections above use different averaging windows, set by the sampling scheme of each instrument and by the frequency resolution required per band. Table 3.1 summarises the window used for each parameter.

Table 3.1: Analysis window used for each parameter. Where two windows are given for the ADV-lidar, the record was analysed over the longer window and, in addition, over the same $30\,\mathrm{min}$ windows as the ADV bursts, so that the stations can be compared over an identical window length.

Parameter	Symbol	Record	Window	Section
Water depth	$h(t)$	all pressure sensors	$1\,\mathrm{h}$ running mean	3.2.1
Tidal level	$\tilde{\eta}_{tide}$	RS2 only	$1\,\mathrm{h}$ running mean	3.2.4
Wave set-up	$\bar{\eta}$	all reef-flat pressure sensors	$1\,\mathrm{h}$ running mean	3.2.4
Energy density spectrum	$S_\eta(f)$	all pressure sensors	$3\,\mathrm{h}$ ($55\,\mathrm{min}$ segments)	3.2.3
Wave parameters	H_s, T_{m01}, T_p	all pressure sensors	$3\,\mathrm{h}$	3.2.3
Narrow-band wave height	H_{eq}	reef-flat pressure sensors	$3\,\mathrm{h}$	3.2.7
Transfer functions	R^2, RMSE	reef-flat pressure sensors, ADV-lidar	$3\,\mathrm{h}$	3.2.5
Fundamental mode	f_n	bed profile with RF1 water level	$3\,\mathrm{h}$	3.2.8
Variance ratio	N, α	ADV3 only	$30\,\mathrm{min}$ burst	3.2.2
		ADV-lidar	$3\,\mathrm{h}$ and $30\,\mathrm{min}$	
Wave direction	$\bar{\theta}$, $\bar{\delta}$	ADV1, ADV3	$30\,\mathrm{min}$ burst	3.2.6
		ADV-lidar	$3\,\mathrm{h}$ and $30\,\mathrm{min}$	
Reflection coefficient	K_r	ADV1, ADV3	$30\,\mathrm{min}$ burst	3.2.7
		ADV-lidar	$3\,\mathrm{h}$ and $30\,\mathrm{min}$	
Run-up levels	$\bar{R}$, $R_{2\%}$	video camera	$1\,\mathrm{h}$	3.2.9
Shoreline water level	$\bar{\eta}$, $\eta_{2\%}$	ADV-lidar	$1\,\mathrm{h}$	3.2.9

4

Results

This chapter presents the results of the data analyses of the field measurements carried out at the La Saline fringing reef. Section 4.1 characterises the offshore forcing conditions during the campaign. Section 4.2 assesses to what extent the observed LF motions can be attributed to surface waves. Section 4.3 presents the hydrodynamic parameters across the reef system, the dependence of the LF wave heights ($H_{s,IG}$ and $H_{s,VLF}$) on the offshore forcing conditions, and the occurrence of standing-wave patterns and resonance. Section 4.4 then considers 11 July 2024 in detail, when the surface elevation and velocities near the shoreline, as well as run-up data, were available.

4.1. Offshore forcing conditions during measurement period

Measurements on the reef slope took place between 4 June and 17 September 2024. Figure 4.1 shows conditions at RS2 during this period, which represent the offshore forcing conditions.

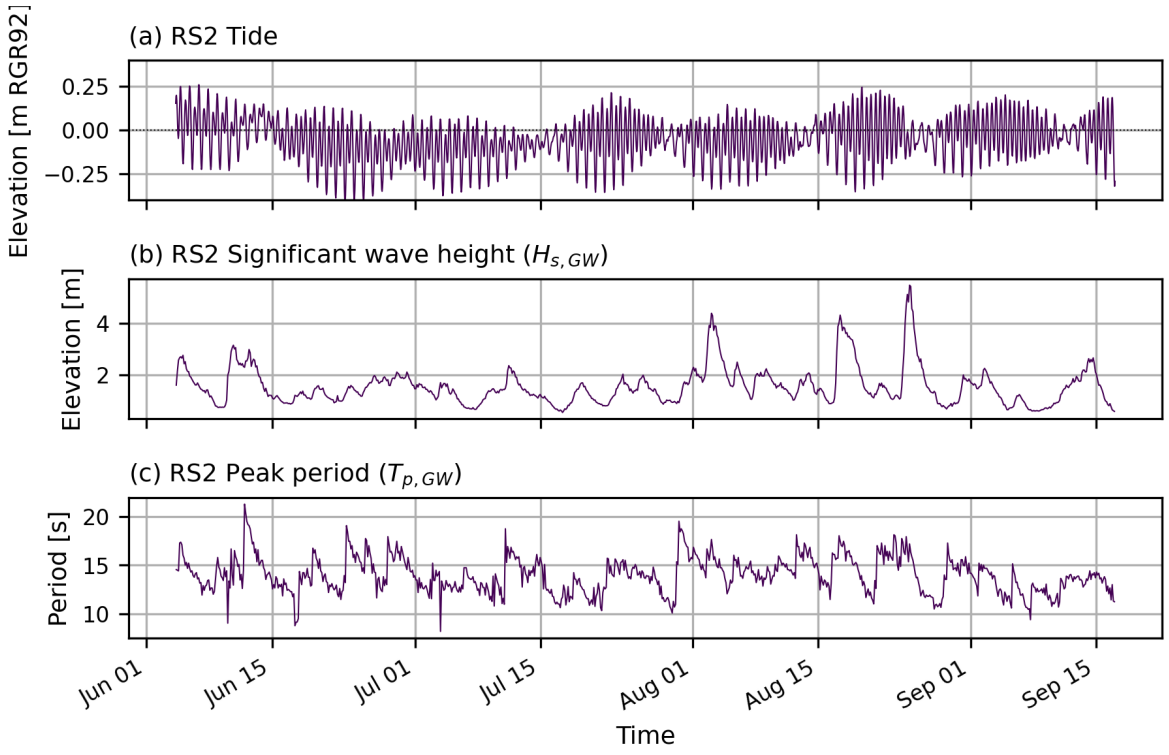


Figure 4.1: Offshore forcing conditions measured at the reef slope station RS2 over the study period: (a) tide, referenced to RGR92 vertical datum, (b) GW significant wave height $H_{s,GW}$, (c) GW peak period $T_{p,GW}$.

Figure 4.1a shows the tide. The tide is semi-diurnal, with a clear spring–neap modulation. The tide ranged from $-0.41\,\mathrm{m}$ to $0.26\,\mathrm{m}$ relative to RGR92 (MSL), with a mean tidal range (MTR) of $0.26\,\mathrm{m}$ (std. dev. $0.12\,\mathrm{m}$, reflecting the spring–neap spread).

The GW significant wave height $H_{s,GW}$ at RS2 (Figure 4.1b) ranged from $0.54\,\mathrm{m}$ to $5.46\,\mathrm{m}$ (mean $1.55\,\mathrm{m}$) over the study period, with the maximum occurring on 25 August 2024, accompanied by a peak period of $17.2\,\mathrm{s}$ (Figure 4.1c). GW peak period $T_{p,GW}$ ranged from $8.2\,\mathrm{s}$ to $21.3\,\mathrm{s}$ (mean $14.0\,\mathrm{s}$). Together, the small tidal range and relatively large wave heights classify the site as microtidal and wave-dominated.

In the subsequent sections, the offshore forcing conditions refer to the conditions in the GW band measured at RS2 (Figure 4.1). In addition to these, other GW-band parameters measured at RS2 are also used in the subsequent analysis, such as the mean period $T_{m01,GW}$, which is used in the offshore wave power proxy $P_{Tm01} = H_{s,GW}^2\, T_{m01,GW}$. This wave power proxy is always used in the context of offshore conditions and is therefore given without the RS2 subscript.

4.2. Nature of the low-frequency energy: surface versus shear waves

To assess whether the LF motions observed at the La Saline fringing reef are surface waves or result from other processes such as shear instabilities of the mean current (Section 2.4.3), the normalised velocity-to-pressure variance ratio N was computed. This analysis was restricted to ADV3 over the period from 29 June to 17 July 2024, complemented by the ADV-lidar located $20\,\mathrm{m}$ from the shoreline, which recorded on 11 July.

Because LF wave heights on reefs have been reported to scale with the offshore forcing, both at this site (Bruch et al. 2022) and on other fringing reefs (Cheriton et al. 2016; Shimozono et al. 2022), it is also investigated whether the ratio is forcing-dependent. Figure 4.2 presents the temporal evolution of N at ADV3 for the IG (a) and VLF (c) bands together with its dependence on the offshore wave power proxy P_{Tm01} (b, d), and Figure 4.3 compares ADV3 with the ADV-lidar record near the shoreline on 11 July.

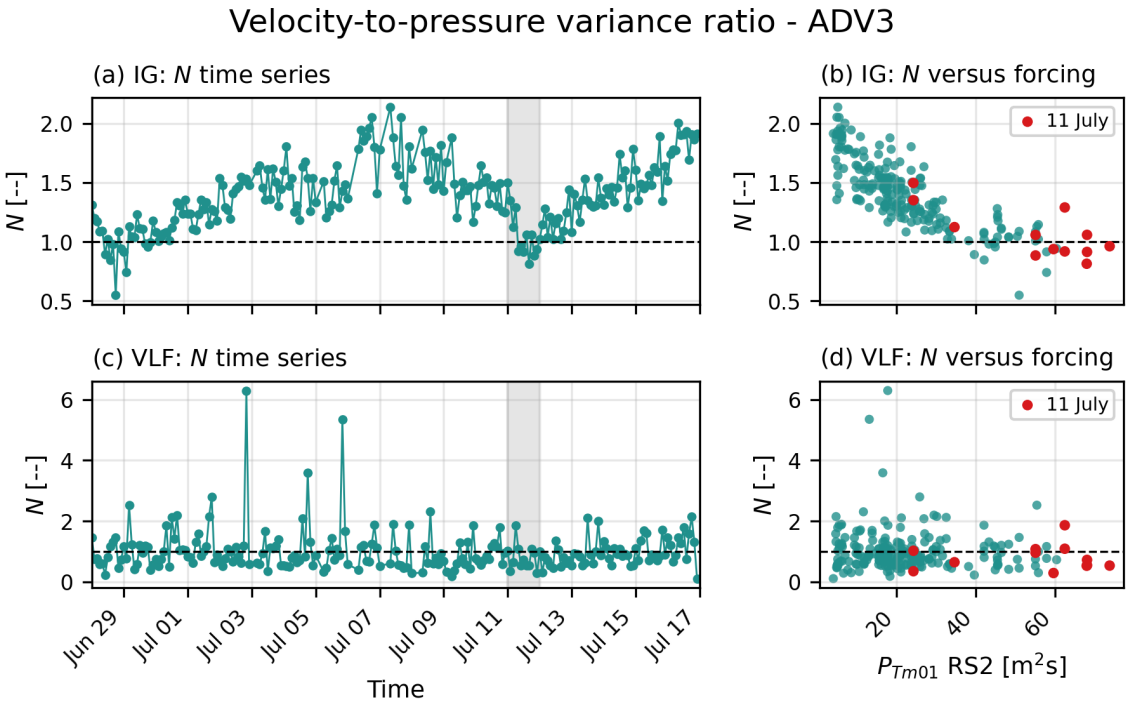


Figure 4.2: Normalised velocity-to-pressure variance ratio N at ADV3. The left column shows the N time series for the IG (a) and VLF (c) bands from 29 June to 17 July, with the shaded band marking 11 July. The right column shows N against the offshore wave power proxy $P_{Tm01} = H_{s,GW}^2\, T_{m01,GW}$ measured at RS2, for the IG (b) and VLF (d) bands, with the 11 July bursts in red. The dashed horizontal line marks $N = 1$.

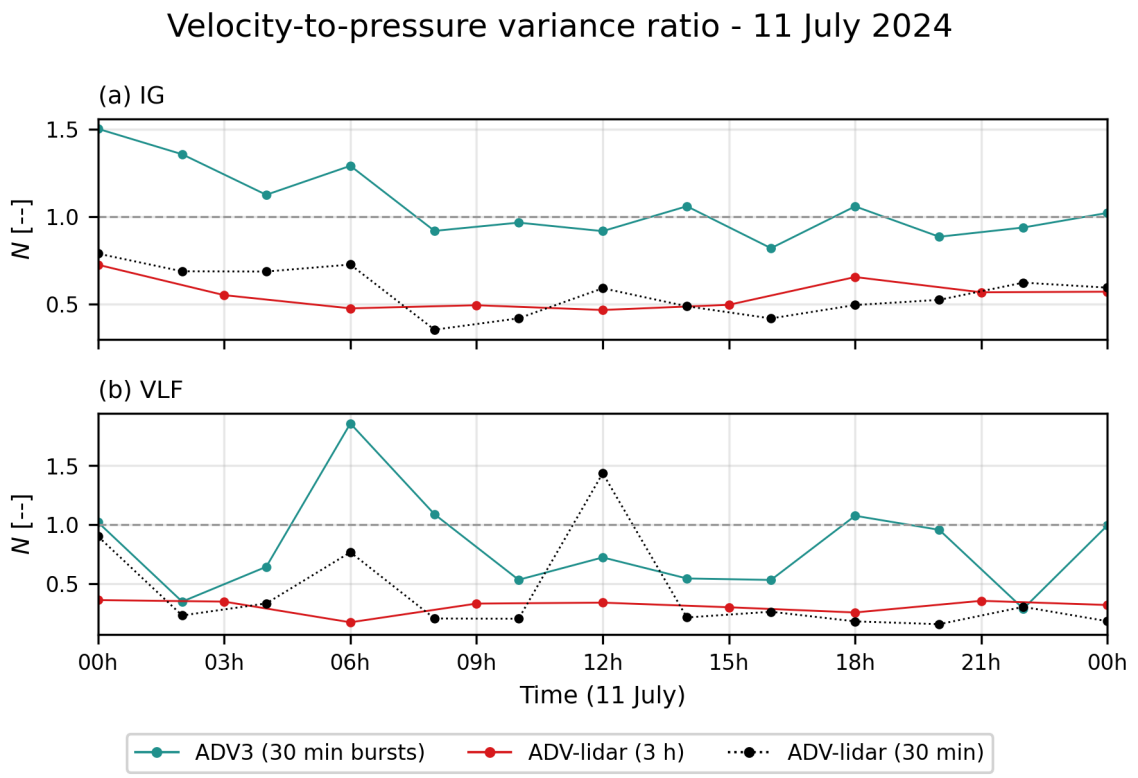


Figure 4.3: Normalised velocity-to-pressure variance ratio N at ADV3 and ADV-lidar on 11 July 2024, for the IG (a) and VLF (b) bands. ADV3 is given per $30\,\mathrm{min}$ burst, and the ADV-lidar over $3\,\mathrm{h}$ windows as well as over the same $30\,\mathrm{min}$ windows as the ADV3 bursts. The dashed horizontal line marks $N = 1$.

Figure 4.2a shows that the IG ratio predominantly lies between approximately 1 and 2, and decreases towards 1, and occasionally below it, as the offshore forcing increases (Figure 4.2b). Values below 1 can be associated with (partially) standing waves, which is investigated further in Section 4.3.3. The maximum IG ratio of approximately 2.2 corresponds to a shear fraction $\alpha \approx 0.55$, well below the ratios of up to about 4 ($\alpha \approx 0.75$) reported by Lippmann et al. (1999) inside the surf zone. On 11 July, when the offshore forcing was strongest (red markers in Figure 4.2b and d), the IG ratio remained close to 1 at ADV3 (mean 1.07) and dropped to 0.56 at ADV-lidar over $3\,\mathrm{h}$ windows (Figure 4.3a).

For the VLF band, most values are also of order 1, generally ranging between approximately 0.1 and 2 (Figure 4.2c), and no clear dependence on the offshore forcing is apparent (Figure 4.2d). On 11 July, the VLF ratio also decreases towards the shoreline, from a mean of 0.80 at ADV3 to 0.31 at ADV-lidar (Figure 4.3b). The ratios below 1 at ADV-lidar may again indicate an antinode of a (partially) standing wave field, which is examined for 11 July in more detail in Section 4.4.2.

Figure 4.2c also shows a limited number of considerably higher VLF ratios, reaching a maximum of $N = 6.29$. The burst with this highest ratio is examined in Figure 4.4 and compared with the subsequent low-ratio burst ($N = 0.57$).

The GW component at RS2 (Figure 4.4a, b) shows low forcing conditions during both records. The mean current (Figure 4.4c, d) shows a negligible alongshore velocity and a cross-shore velocity of about $-0.1\,\mathrm{m\,s^{-1}}$ and $-0.02\,\mathrm{m\,s^{-1}}$ during the high- and low-ratio bursts, respectively. Moreover, the difference in the N values is specific to the VLF band, as the IG ratios are similar for both bursts ($N = 1.53$ and $N = 1.47$, Figure 4.4e, f).

Given that the mean alongshore velocity is small during both bursts (Figure 4.4c, d), there is little indication of the alongshore-current shear instability described in Section 2.4.3. Other slowly varying or rotational motions can nonetheless not be excluded. An alongshore-variable cross-shore current, for example, could contribute to the observed velocity fluctuations, but resolving such variability would

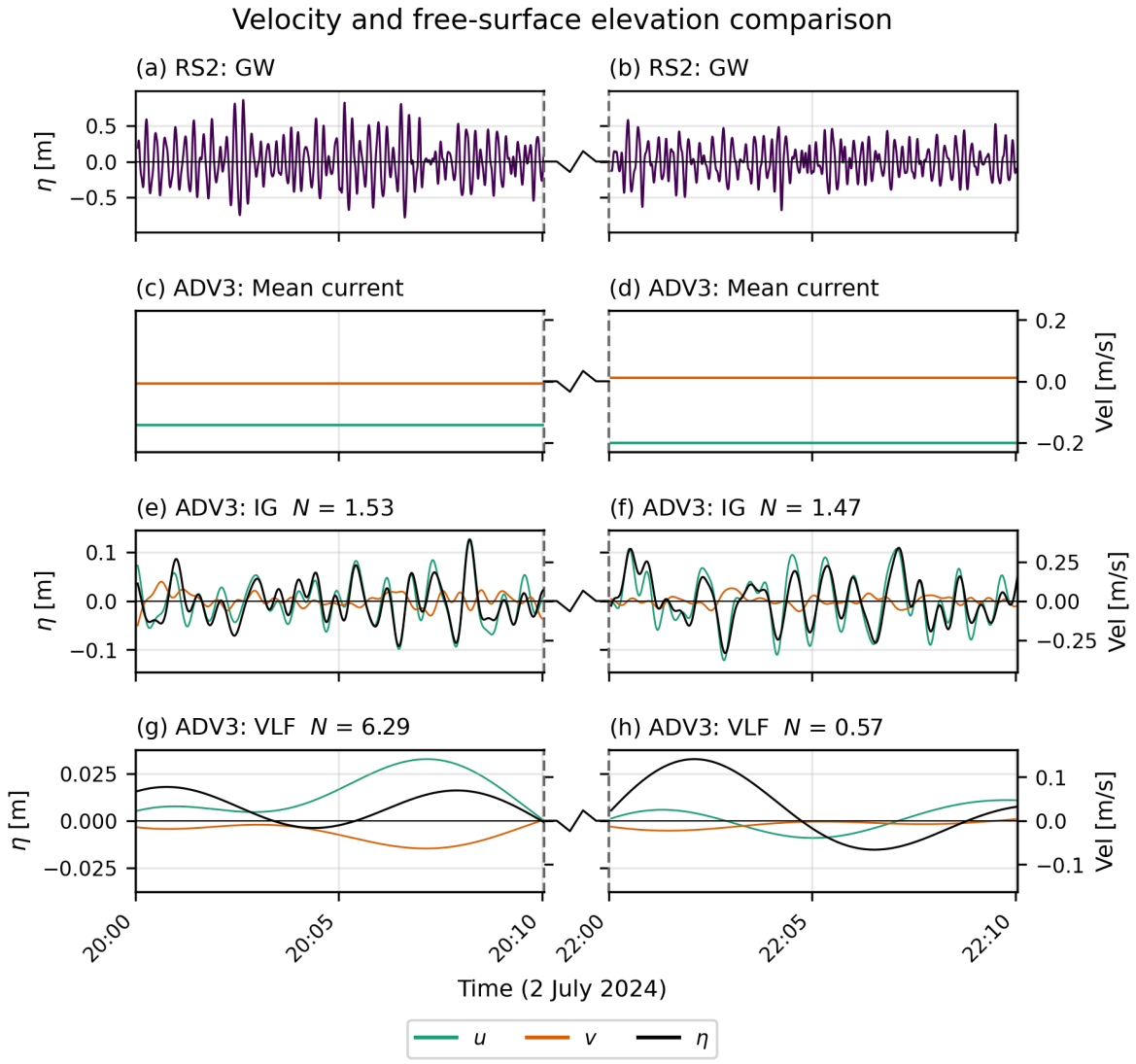


Figure 4.4: Comparison of two ADV3 bursts on 2 July 2024, one with a high VLF ratio ($N = 6.29$, 20:00) and one with a low VLF ratio ($N = 0.57$, 22:00). From top to bottom the rows show the GW-band surface elevation at RS2, the ADV3 mean current, and the IG and VLF band-passed surface elevation η and horizontal velocities. The left column shows the high-ratio burst and the right column the low-ratio burst.

require spatially separated velocity measurements, which were not available for these bursts.

The ratios are also subject to the limitations of the method itself. Noyes et al. (2002) showed that such methods can ascribe a shear fraction of $\alpha \approx 0.33$ to the IG velocity variance even when the mean alongshore current is weak and shear waves are most likely absent. The weak alongshore velocities observed here therefore fall in this least-reliable regime, so that ratios moderately above 1 are not, by themselves, evidence of a shear-wave contribution.

The interpretation of the VLF ratios is further limited by the ADV burst duration of $30\,\mathrm{min}$, which is shorter than the longest VLF periods. The lowest-frequency VLF motions are therefore not fully resolved within a single burst, and the variance is based on only a few wave cycles. This makes the calculated ratio sensitive to slowly varying fluctuations within the measurement window. At the ADV-lidar, where both window lengths could be applied to the same record, the VLF ratio over $30\,\mathrm{min}$ windows has a mean of 0.43 and a standard deviation of 0.40, against 0.31 and 0.06 over $3\,\mathrm{h}$ windows (Figure 4.3b).

Overall, the results indicate that a mixture of contributions is most likely present, and that the observed LF motions cannot be attributed entirely to surface waves. Under the energetic forcing that is of primary

interest in this study the ratio is nonetheless around or below 1, with the time series showing a clear signature in the surface elevation. This study focuses on the surface component of the LF motions, while recognising that additional velocity variability attributed to other processes is likely present.

4.3. General observations during measurement campaign

This section examines the hydrodynamic bulk parameters derived from the wave spectra, following the procedure described in Section 3.2.3, and the water level parameters obtained following the method described in Section 3.2.4. The spatial variability of the bulk parameters is examined by first assessing the limited longshore variability and then focusing on the cross-shore evolution, starting with the distribution of energy across the frequency bands and followed by the water levels, wave periods, and wave heights (Section 4.3.1). The influence of the offshore forcing on $H_{s,IG}$ and $H_{s,VLF}$ is subsequently quantified (Section 4.3.2), after which standing wave patterns (Section 4.3.3) and resonance are assessed (Section 4.3.4).

4.3.1. Spatial variability of bulk hydrodynamic parameters

The spatial variability of the bulk parameters was considered both alongshore and cross-shore. Since, as described below, no significant alongshore variability was found with the sensor set-up, the cross-shore variability forms the main focus of this section.

Appendix E provides the temporal evolution of the significant wave heights and the water depth at each station along the longshore transect (RF3, RF3a, and RF3b). It was found that, within each band, the significant wave heights were of comparable magnitude across the three longshore stations during the whole measurement campaign. The small differences that are present cannot be attributed to physical processes, but instead reflect the spatial setting of the stations, namely their differing distance to the reef crest and the cross- and longshore inhomogeneous bathymetry (Figure 3.2). This inhomogeneity is also reflected in the mean water depth over the period during which all stations were simultaneously deployed, which differed between the stations, at $1.07\,\mathrm{m}$ (RF3), $1.24\,\mathrm{m}$ (RF3a), and $0.98\,\mathrm{m}$ (RF3b).

The cross-shore evolution is examined below, beginning with the distribution of wave energy across the frequency bands before turning to the water levels, wave periods, and wave heights. The latter three are shown in Figure 4.5. The average values reported in these sections are taken over the period during which all stations were simultaneously deployed (27 June to 16 August 2024, excluding the RF7 gap of 22 to 30 July), with the band fractions obtained from the mean energy density spectrum over this period (Section 3.2.3). Their temporal variability, obtained from the individual $3\,\mathrm{h}$ spectra, is given as the standard deviation in parentheses after each mean. For detailed information during 11 July, which includes a sensor close to the shoreline, see Section 4.4.

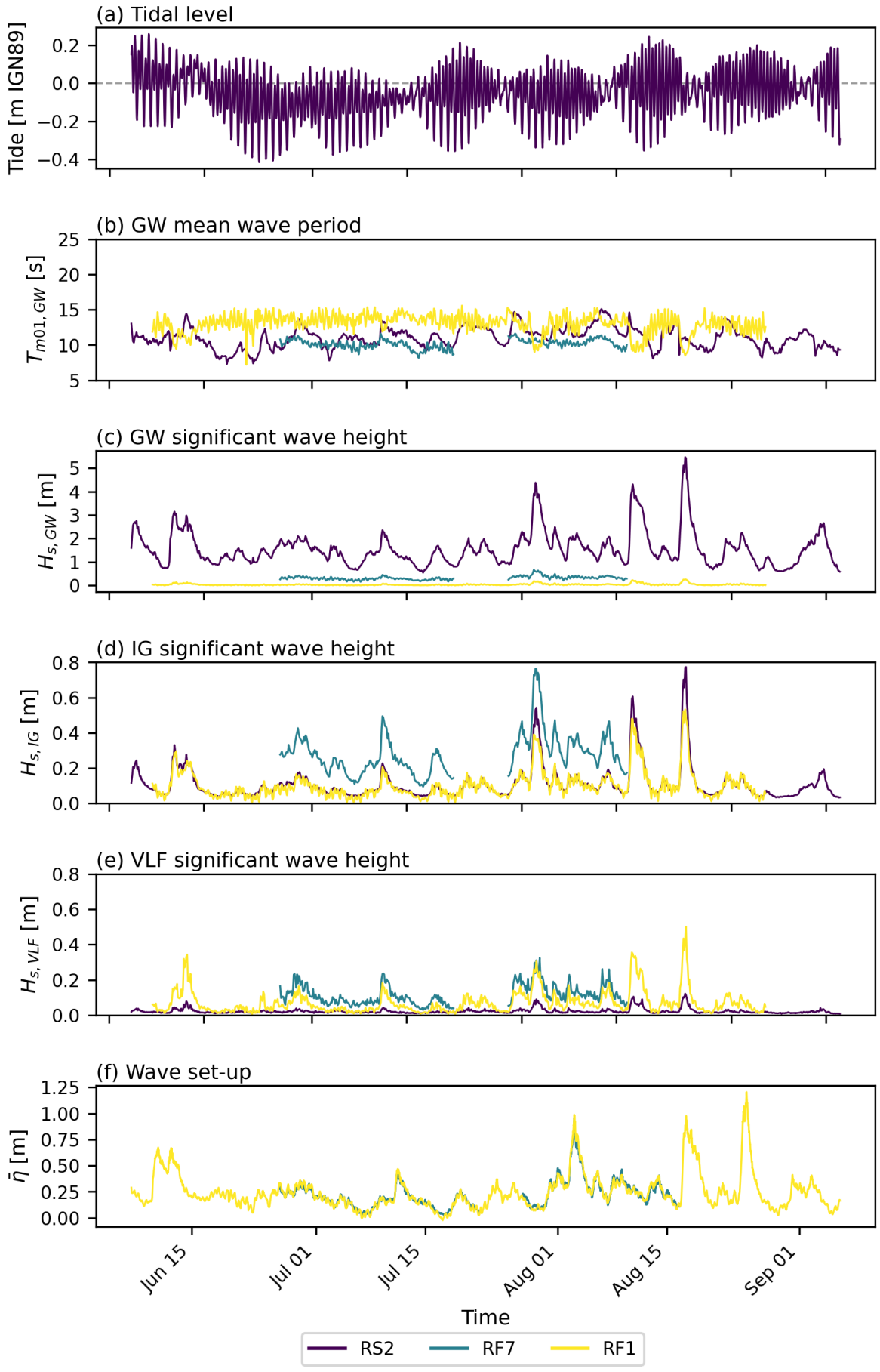


Figure 4.5: Hydrodynamic parameters at RS2, RF7, and RF1 over the full study period: (a) tide, (b) $T_{m01,GW}$, (c) $H_{s,GW}$, (d) $H_{s,IG}$, (e) $H_{s,VLF}$, (f) wave set-up $\bar{\eta}$ at RF7 and RF1.

Energy

The distribution of energy across the three frequency bands is examined from the reef slope (RS2), across the reef crest (RF7), to the mid-reef station (RF1). The full temporal evolution of the wave spectra can be found in Appendix F. The mean energy fraction per band, and the change in the absolute band energy relative to RS2, are summarised in Table 4.1.

Table 4.1: Mean band energy fractions at the reef slope (RS2), reef crest (RF7), and mid-reef (RF1), obtained from the mean energy density spectrum, with the standard deviation of the individual $3\,\mathrm{h}$ fractions in parentheses. The last three columns give the change in the absolute band energy relative to RS2. All values are computed over the period during which all stations were simultaneously deployed (27 June to 16 August 2024, excluding the RF7 gap of 22 to 30 July).

	Energy fraction [%]			Abs. energy change vs RS2 [%]		
Station	GW	IG	VLF	GW	IG	VLF
RS2 (reef slope)	99.35 ($\pm$0.2)	0.62 ($\pm$0.2)	0.02 ($\pm$0.0)	—	—	—
RF7 (reef crest)	49.5 ($\pm$11)	42.0 ($\pm$9)	7.6 ($\pm$4)	-96	$+490$	$+2900$
RF1 (mid-reef)	8.2 ($\pm$3)	59.0 ($\pm$9)	30.7 ($\pm$10)	-99.9	-20	$+1060$

At RS2, the spectrum is dominated by GW energy, which on average accounts for $99.35\,\%$ of the total energy, so that the IG and VLF contributions are negligible there. These fractions were nearly constant in time. Moving onto the reef flat, the energy distribution changes. At RF7, GW energy is strongly reduced relative to RS2, consistent with dissipation through depth-limited breaking over the reef crest, while the IG and VLF fractions increase to $42.0\,\%$ and $7.6\,\%$. At RF1, further onshore, the GW contribution is reduced to $8.2\,\%$, against $59.0\,\%$ for IG and $30.7\,\%$ for VLF. In contrast to RS2, these fractions fluctuated strongly between individual spectra on the reef flat, and became increasingly variable toward the mid-reef, with the VLF fraction the most variable of all.

Although the IG and VLF fractions are largest at RF1, the absolute IG and VLF energy is on average lower than at RF7, since both bands peaked at the reef crest before decreasing again toward the mid-reef, and the absolute IG energy at RF1 is thereby of comparable magnitude to that at RS2. Two mechanisms may explain this maximum. Shoaling of the free long waves over the reef slope follows Green's law ($H \propto h^{-1/4}$) and increases their height toward shallower water (Battjes et al. 2004), and at the crest the energy has not yet been dissipated over the reef flat. Shoreward of the crest, bottom friction progressively decreases LF energy, which explains the decrease toward the mid-reef.

Water levels

This section presents the temporal variation of the water levels across the reef, comprising the tide and wave-induced set-up. The tide was determined from the RS2 record (Section 3.2.4) and already presented in Section 4.1. The tide is assumed spatially uniform across the study area and is presented again in Figure 4.5a. The wave-induced set-up is shown in Figure 4.5f for RF7 and RF1. The RF1 and RF7 set-up are nearly uniform, so only the RF1 values are reported here. The wave set-up at RF1 reached a maximum of $1.20\,\mathrm{m}$, with a mean value of $0.25\,\mathrm{m}$. The maximum set-up of $1.20\,\mathrm{m}$ occurred on 25 August 2024, corresponding to the maximum incident GW wave height during the measurement period, $H_{s,GW} = 5.46\,\mathrm{m}$, with a mean period $T_{m01,GW} = 11.1\,\mathrm{s}$ and a tide level of $-0.07\,\mathrm{m}$.

Regarding the set-up across the whole reef flat, the set-up time series of all five reef-flat stations (RF7, RF5, RF4, RF3, RF1) is shown in Appendix C. The set-up varied slightly across the reef flat. The mean set-up varied from $0.22\,\mathrm{m}$ at RF7 and $0.25\,\mathrm{m}$ at RF1 to about $0.33\,\mathrm{m}$ at the mid-reef stations (RF5, RF4, RF3). However, the set-up can reach up to $1.20\,\mathrm{m}$ during the most energetic event, so the relative difference across the reef flat becomes smaller during energetic events. The set-up is expected to be relatively uniform across the reef flat. Unlike a sloping beach, where wave breaking and the associated radiation-stress gradients continue up to the shoreline, a fringing reef has a shallow platform shoreward of the surf zone across which these gradients, and thus any further change in set-up, are limited (Becker et al. 2014). This is in line with Vetter et al. (2010), who also found the reef-flat set-up to be approximately uniform. The small differences in mean set-up between the stations are therefore not necessarily a systematic cross-shore trend, as they may also result from the slightly different positions of the sensors along the cross-shore transect (Figure 3.2), from local bathymetric effects, or from the uncertainty in the surveyed sensor elevations, which is further explained in Appendix C. A constant

water level, equal to the RF1 value, is therefore assumed across the reef flat in the subsequent analysis and in the fundamental-mode calculation (Section 3.2.8, with the results in Section 4.3.4).

Wave periods

Figure 4.5b shows the mean period in the GW band. At RS2, $T_{m01,GW}$ fluctuated more over time than at the reef-flat stations ($11.04\,\mathrm{s} \pm 1.47\,\mathrm{s}$), reflecting the variability of the offshore wave climate. Moving onto the reef flat, $T_{m01,GW}$ decreased slightly at RF7 ($10.16\,\mathrm{s} \pm 0.65\,\mathrm{s}$) before increasing again toward RF1 ($13.01\,\mathrm{s} \pm 1.36\,\mathrm{s}$).

In addition, the mean peak frequency in the IG band shifts across the reef flat, occurring at a different frequency at each reef-flat station, as visible in the mean energy density spectra (Figure 3.4 in Section 3.2.3) and in the spectral evolution over the campaign (Appendix F). This cross-shore shift of the IG peak may indicate the presence of standing-wave patterns over the reef flat, which is examined following Section 3.2.7, with the results given in Section 4.3.3.

Wave heights

Figure 4.5c–e shows the temporal evolution of the significant wave height. The cross-shore pattern is consistent with the energy distribution described before. The mean $H_{s,GW}$ decreased by $97.6\,\%$ from RS2 to RF1, whereas $H_{s,IG}$ remained of comparable magnitude (a net change of $-7.8\,\%$) and $H_{s,VLF}$ increased by $234.8\,\%$. Over the full study period, mean $H_{s,GW}$ decreased from $1.55\,\mathrm{m}$ at RS2 to $0.04\,\mathrm{m}$ at RF1, while mean $H_{s,IG}$ and $H_{s,VLF}$ both peaked at RF7 ($0.28\,\mathrm{m}$ and $0.12\,\mathrm{m}$, respectively) before decreasing toward RF1 ($0.10\,\mathrm{m}$ and $0.08\,\mathrm{m}$). The remaining reef-flat stations (RF5, RF4, RF3), not shown in Figure 4.5, lay between RF7 and RF1.

Figure 4.6 shows the cross-shore evolution pattern of the significant wave height in more detail, including the effect of the offshore forcing, with each band normalised by its value at RF7 and coloured by the offshore forcing, represented by the wave power proxy ($P_{Tm01} = H_{s,GW}^2\, T_{m01,GW}$). Independent of the forcing, $H_{s,GW}$ decreases from RF7 toward the mid-reef, and the same holds for $H_{s,IG}$. For the VLF waves, the behaviour differs. As the offshore forcing increases, $H_{s,VLF}$ first decreases toward RF5 but then increases again toward RF1. At two timestamps during the energetic event around 2 August, $H_{s,VLF}$ at RF1 exceeded the value at RF7. These two timestamps are examined further in the resonance assessment (Section 4.3.4).

In addition, Figure 4.7 shows the band decomposition for an interval on 3 August between 01h30 and 01h45 at RF7, RF4, and RF1, where this increase in VLF wave height is also shown in the time series.

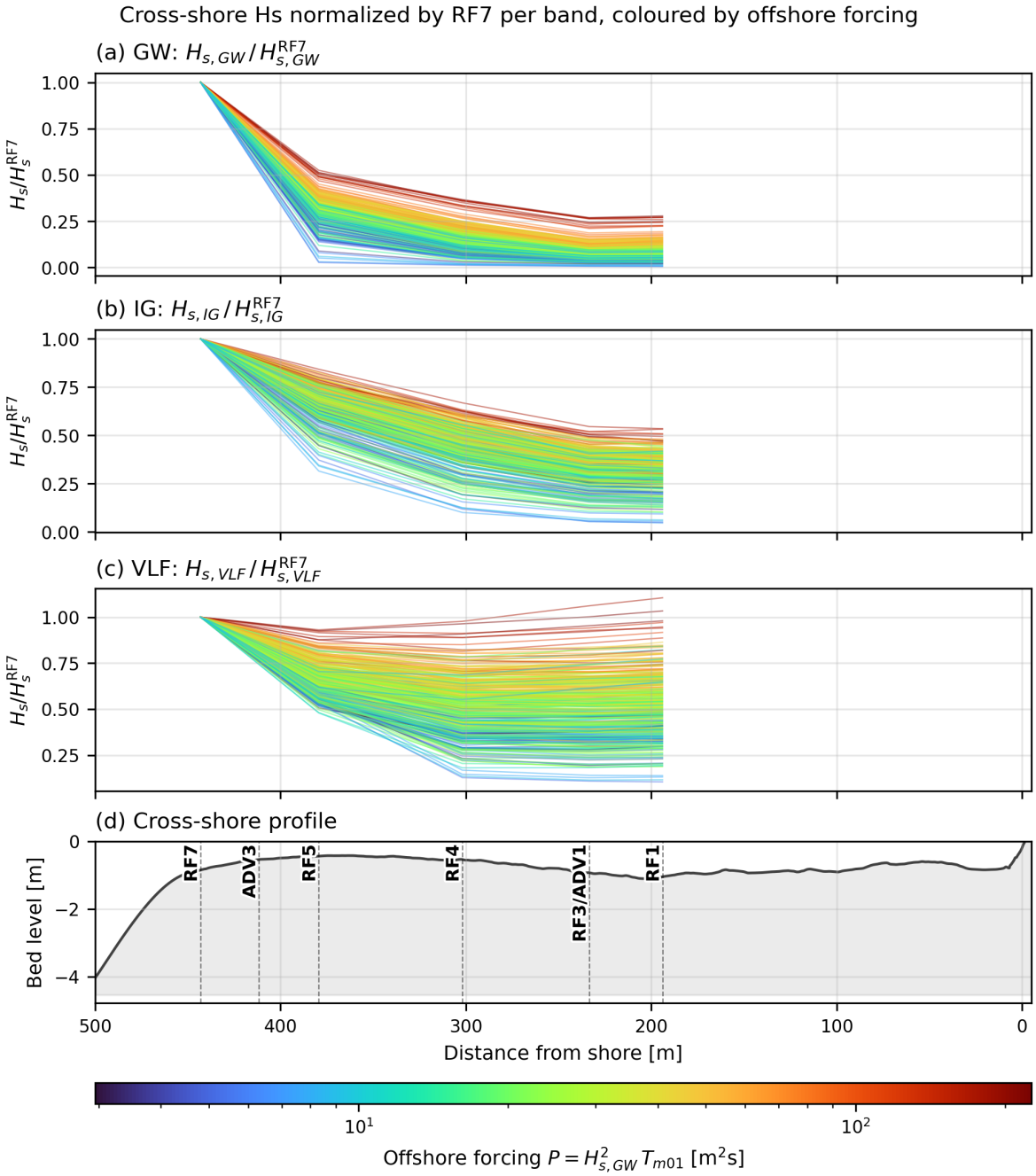


Figure 4.6: Cross-shore evolution of the significant wave height per band, normalised by the value at RF7 ($H_{s,\mathrm{band}}/H_{s,\mathrm{band}}^{\mathrm{RF7}}$). Only $3\,\mathrm{h}$ windows during which all sensors were simultaneously present in the array are included, which covers 27 June–16 August 2024, excluding 22–30 July 2024. Each line is one $3\,\mathrm{h}$ window, coloured by the offshore forcing $P_{Tm01} = H_{s,GW}^2\, T_{m01,GW}$: (a) GW, (b) IG, (c) VLF, and (d) the cross-shore bed profile.

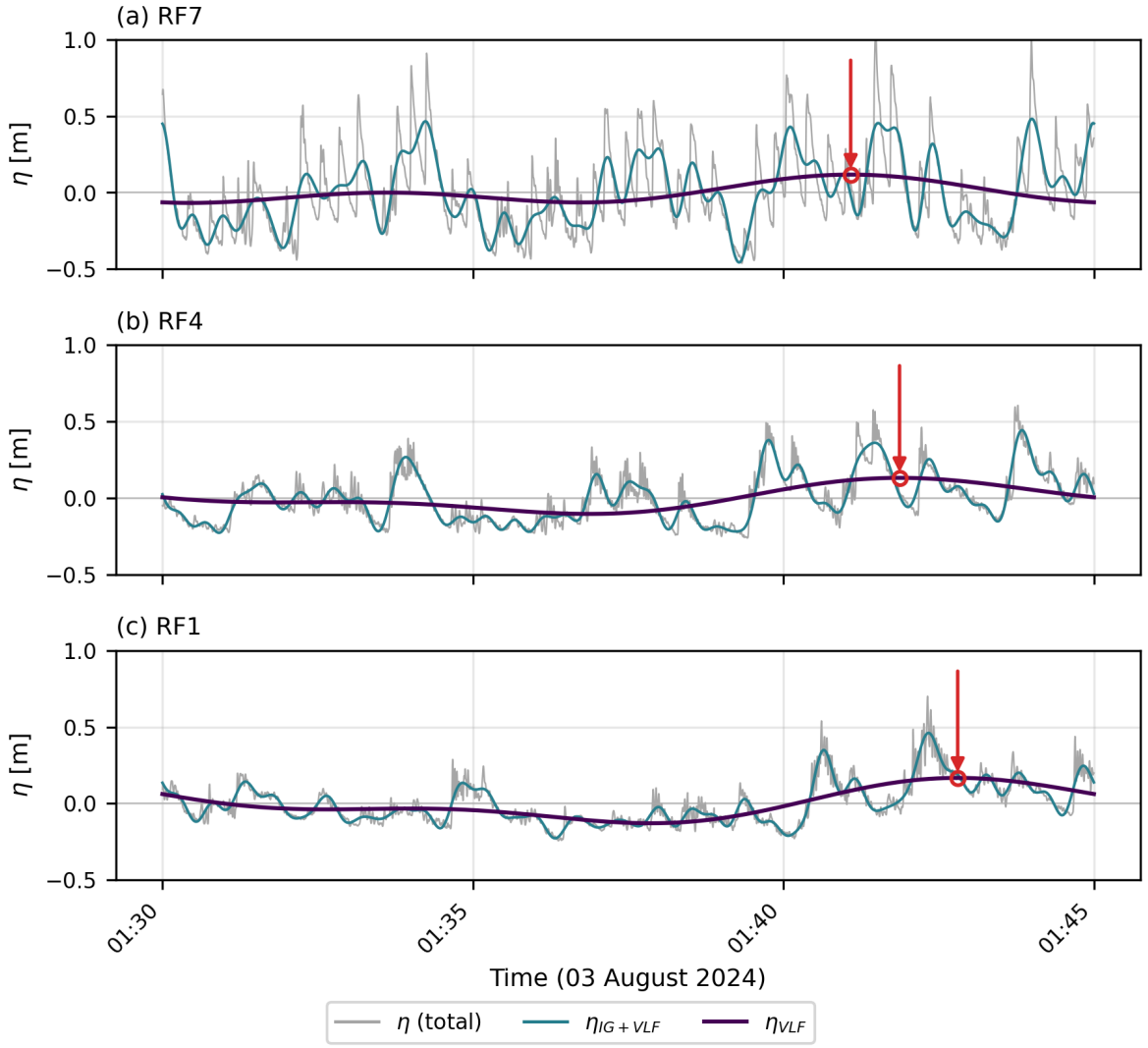


Figure 4.7: Free-surface elevation and its low-frequency components at (a) RF7, (b) RF4, and (c) RF1 on 3 August 2024 between 01h30 and 01h45, showing the demeaned total free-surface elevation η, the combined IG+VLF component η_{IG+VLF}, and the VLF component η_{VLF}, all on the same vertical scale. The red arrows indicate the maximum of the VLF component, which is $0.12\,\mathrm{m}$ at RF7, $0.13\,\mathrm{m}$ at RF4, and $0.17\,\mathrm{m}$ at RF1.

4.3.2. Influence of offshore forcing on $H_{s,IG}$ and $H_{s,VLF}$

With the hydrodynamic parameters characterised across the reef flat (see Section 4.3.1), transfer functions were constructed to identify which offshore and local parameters most strongly govern the IG and VLF wave height, following the multiple linear regression approach described in Section 3.2.5, where the tested predictors are also listed. For both $H_{s,IG}$ and $H_{s,VLF}$, the best-performing transfer function combined the wave power proxy based on T_{m01}, $P_{Tm01} = H^2_{s,GW}\, T_{m01,GW}$, with the tidal component of the water level. The resulting transfer functions for every station for IG can be found in Table 4.2 and for VLF in Table 4.3.

Figure 4.8 shows the corresponding fits at the two reef-flat sensors furthest apart across the array (RF7, RF1), together with the ADV-lidar record near the shoreline. The intercept in each transfer function is not a physical quantity but follows from the least-squares fit, and is therefore not interpreted further.

Table 4.2: Transfer functions for $H_{s,IG}$ at each reef-flat sensor, with the coefficient of determination R^2 and the root-mean-square error (RMSE). The last two columns give the ratio of explained variability attributed to each predictor, as a percentage of the total explained variance.

				Explained var. [%]	
Sensor	Transfer function	R^2	RMSE [cm]	P_{Tm01}	$\tilde{\eta}_{tide}$
RF7	$H_{s,IG} = 0.004P_{Tm01} + 0.039\tilde{\eta}_{tide} + 0.163$	0.90	3.6	100	0
RF5	$H_{s,IG} = 0.003P_{Tm01} + 0.163\tilde{\eta}_{tide} + 0.099$	0.93	3.2	97	3
RF4	$H_{s,IG} = 0.002P_{Tm01} + 0.174\tilde{\eta}_{tide} + 0.060$	0.95	2.2	95	5
RF3	$H_{s,IG} = 0.002P_{Tm01} + 0.159\tilde{\eta}_{tide} + 0.038$	0.97	1.3	93	7
RF1	$H_{s,IG} = 0.002P_{Tm01} + 0.161\tilde{\eta}_{tide} + 0.040$	0.97	1.5	94	6
ADV-lidar*	$H_{s,IG} = 0.003P_{Tm01} + 0.169\tilde{\eta}_{tide} + 0.016$	0.97	1.1	97	3

* Based on $n = 10$ spectra (11 July 2024 only).

Table 4.3: Transfer functions for $H_{s,VLF}$ at each reef-flat sensor, with the coefficient of determination R^2 and the root-mean-square error (RMSE). The last two columns give the ratio of explained variability attributed to each predictor, as a percentage of the total explained variance.

				Explained var. [%]	
Sensor	Transfer function	R^2	RMSE [cm]	P_{Tm01}	$\tilde{\eta}_{tide}$
RF7	$H_{s,VLF} = 0.002P_{Tm01} - 0.048\tilde{\eta}_{tide} + 0.069$	0.65	3.5	98	2
RF5	$H_{s,VLF} = 0.001P_{Tm01} + 0.026\tilde{\eta}_{tide} + 0.037$	0.83	2.7	100	0
RF4	$H_{s,VLF} = 0.001P_{Tm01} + 0.069\tilde{\eta}_{tide} + 0.022$	0.87	2.4	98	2
RF3	$H_{s,VLF} = 0.002P_{Tm01} + 0.080\tilde{\eta}_{tide} + 0.019$	0.86	2.4	97	3
RF1	$H_{s,VLF} = 0.002P_{Tm01} + 0.081\tilde{\eta}_{tide} + 0.021$	0.88	2.4	98	2
ADV-lidar*	$H_{s,VLF} = 0.002P_{Tm01} + 0.023\tilde{\eta}_{tide} - 0.008$	0.96	0.9	100	0

* Based on $n = 10$ spectra (11 July 2024 only).

Role of offshore forcing

At every reef-flat sensor, both $H_{s,IG}$ and $H_{s,VLF}$ increase with the offshore wave power indicator P_{Tm01} (Tables 4.3 and 4.2). The variance decomposition suggests that offshore forcing is the main driver of both $H_{s,IG}$ and $H_{s,VLF}$ at every sensor (Tables 4.2 and 4.3). For IG this can be explained by breakpoint forcing, the dominant generation mechanism at a fringing reef, in which the generated long-wave energy scales with the amplitude of the incident wave groups (Symonds et al. 1982; Pomeroy et al. 2012a; Contardo et al. 2025).

Role of water depth

Tidal level, rather than local water depth or wave set-up, was selected as the water-level predictor in order to keep the two predictors independent. Local water depth includes the wave-induced set-up, which is itself dependent on the offshore wave height, whereas the tide is not. Using tidal level in combination with offshore wave power additionally keeps the transfer function applicable for short-term predictive purposes, since the tide is known in advance.

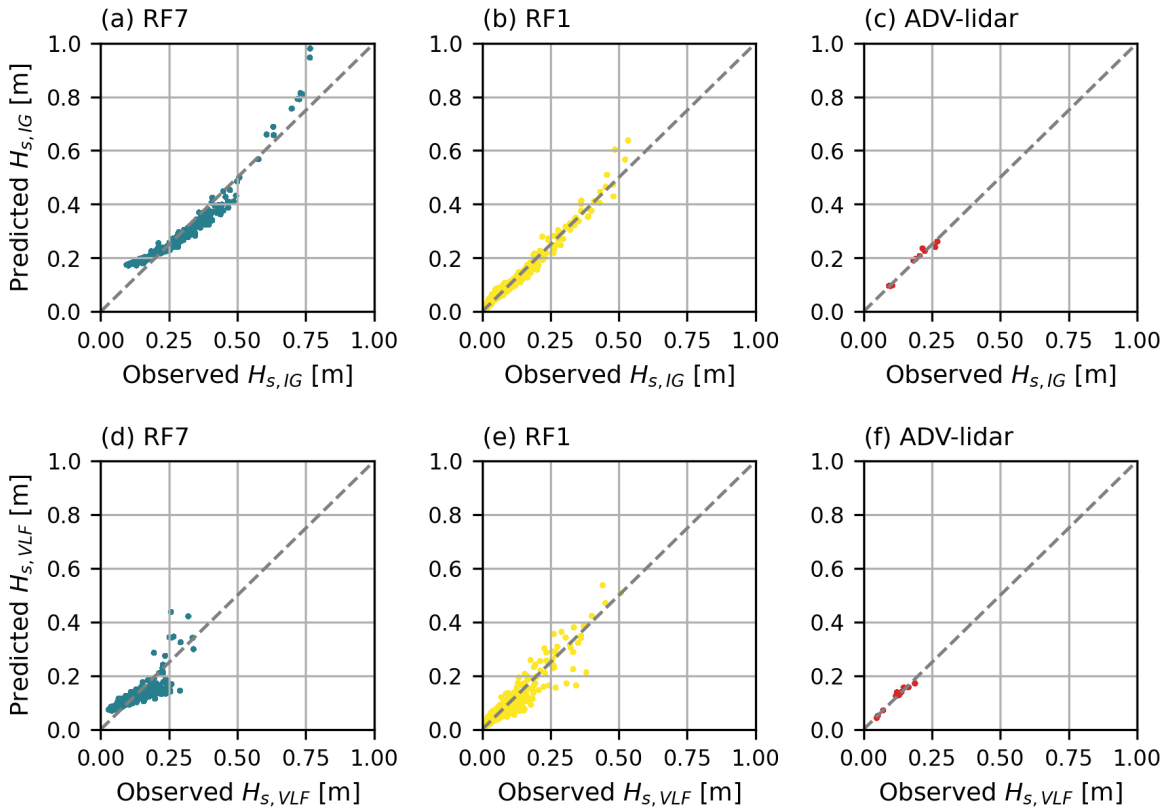


Figure 4.8: Observed versus predicted (a–c) $H_{s,IG}$ and (d–f) $H_{s,VLF}$ at RF7, RF1, and ADV-lidar, using the transfer function based on offshore wave power P_{Tm01} and tidal level. Grey dashed line indicates the 1:1 relation.

The tidal-level coefficient is positive at nearly every reef-flat sensor for both bands, indicating that, for a given offshore wave power, both $H_{s,IG}$ and $H_{s,VLF}$ increase with water depth. This does not hold at RF7, where the tidal-level coefficient for $H_{s,VLF}$ is negative (-0.048), in contrast to all other reef-flat sensors.

This dependence can be linked to dissipation, which is reduced across the reef flat at higher water levels (Bruch et al. 2022; Shimozono et al. 2022). In addition, it should be noted that the water level is incorporated in both predictors, directly through the tide and indirectly through P_{Tm01}, since a higher offshore forcing produces a higher set-up.

Predictive performance across the reef flat

R^2 and RMSE values for each transfer function are reported in Table 4.2 and Table 4.3. R^2 ranges from 0.90 to 0.97 for $H_{s,IG}$ and from 0.65 to 0.96 for $H_{s,VLF}$, with RMSE values between $0.9\,\mathrm{cm}$ to $3.6\,\mathrm{cm}$. At every sensor, the $H_{s,IG}$ transfer function attains a higher R^2 than the corresponding $H_{s,VLF}$ transfer function. Moving from RF7 toward RF1, transfer function performance improves for both bands (R^2 increasing from 0.65 to 0.88 for $H_{s,VLF}$ and from 0.90 to 0.97 for $H_{s,IG}$ across the reef-flat sensors). Performance is lowest for both bands at RF7, especially for the higher observed wave heights, see Figure 4.8a and d. This is also the location with the highest observed wave heights (for both VLF and IG).

4.3.3. Standing patterns

The cross-shore shift of the IG spectral peak identified in Section 4.3.1 suggests that the LF waves over the reef flat may be (partly) standing. In a standing wave field the frequency whose antinode coincides with a given position changes with distance from the shoreline, so each sensor records its maximum energy at a different frequency, unlike in a purely progressive wave field (Section 2.3.2). In addition to the general assessment using the mean spectrum below, it is examined in more detail for 11 July in Section 4.4. There the reflection at the shoreline is considered together with the incoming and outgoing spectra further offshore on the reef flat at ADV3.

The mean spectrum at each reef-flat sensor is shown in Figure 4.9, in which the identified IG-band peak and valley frequencies are indicated. Their values are listed in Table 4.4. The assessment compares the shallow water wavelength of these peak and valley frequencies to the node-antinode spacing expected from linear standing wave theory. The shallow water wavelength was calculated using the mean reef-flat depth $\bar{h}$, averaged spatially over the reef-flat bathymetric profile and temporally over the same period as the mean spectrum. This gives a mean water depth of $\bar{h} = 1.02\,\mathrm{m}$.

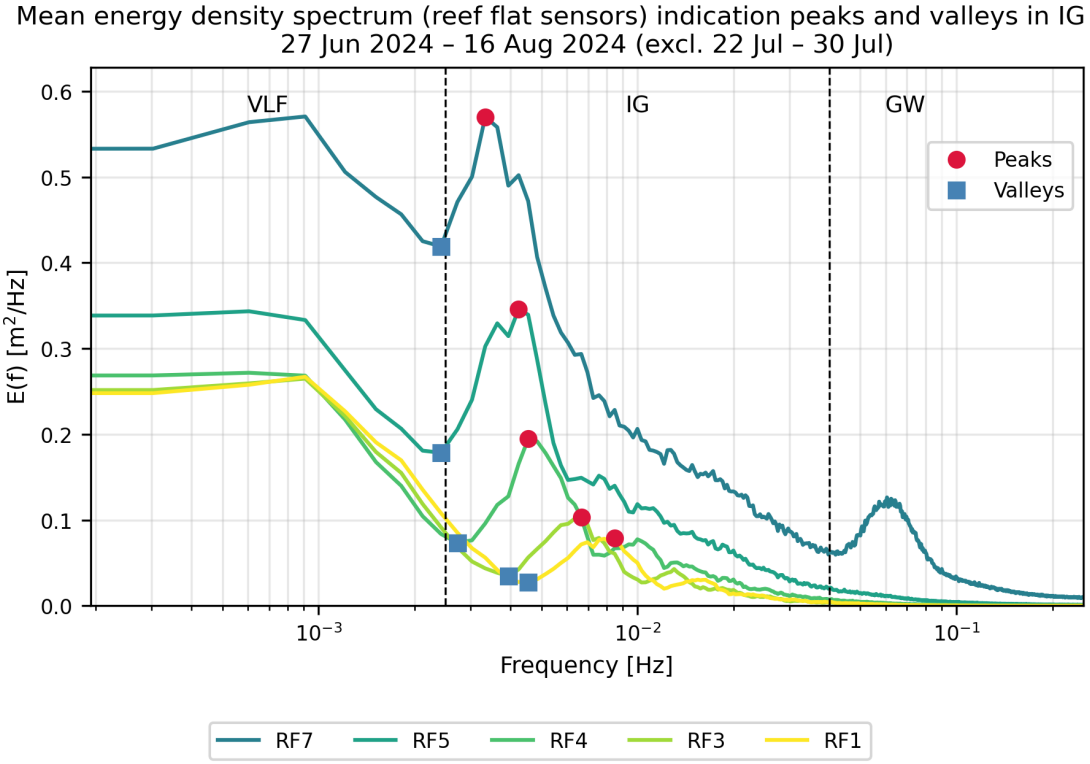


Figure 4.9: Mean energy density spectrum at each reef-flat sensor over the study period, with the selected IG-band peak (antinode) and valley (node) frequencies marked by red circles and blue squares, respectively.

Table 4.4: IG-band peak and valley frequency at each reef-flat sensor.

Sensor	Peak frequency [Hz]	Valley frequency [Hz]
RF7	0.0033	0.0024
RF5	0.0042	0.0024
RF4	0.0045	0.0027
RF3	0.0067	0.0039
RF1	0.0085	0.0045

For a wave with an antinode at the shoreline, antinode locations are expected at $x = L/2,\ L,\ 3L/2,\ \ldots$ and nodes at $x = L/4,\ 3L/4,\ \ldots$ from the shoreline. Figure 4.10 compares the peak (antinode) and

valley (node) wavelengths against these expected distances. The agreement is close at every reef-flat sensor, which supports a node and antinode structure at these IG frequencies.

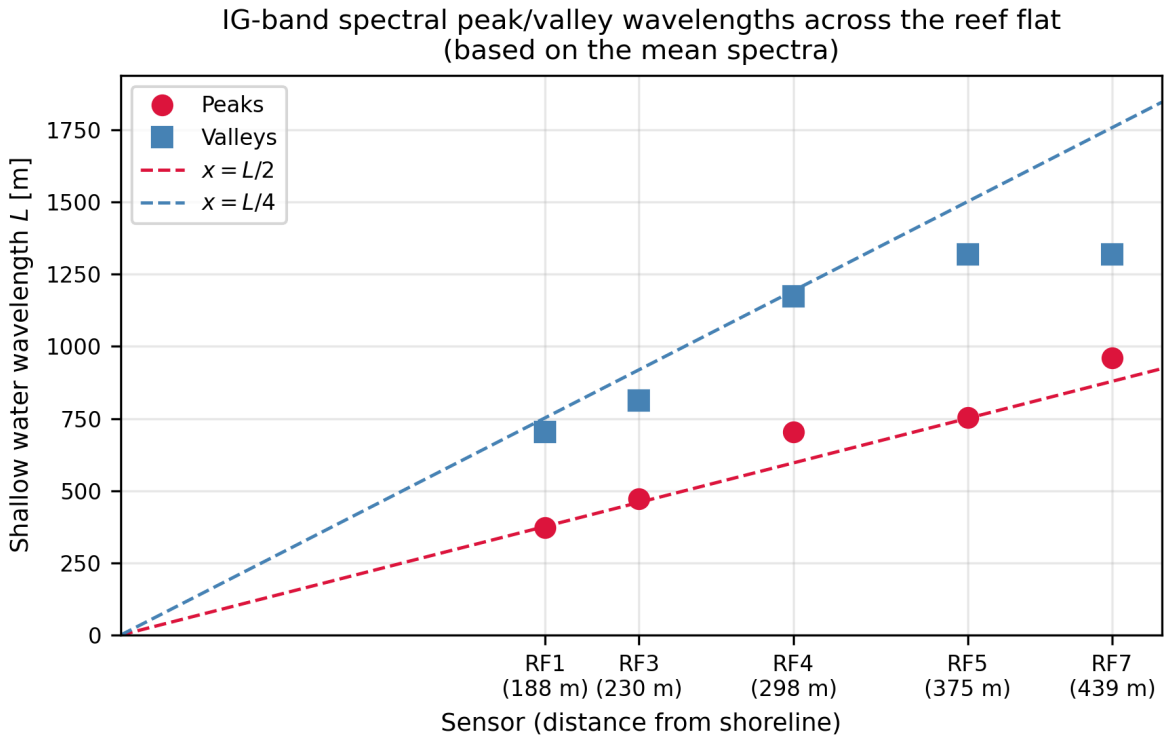


Figure 4.10: Shallow water wavelength of the IG-band peak and valley frequencies at each reef-flat sensor, plotted against distance from the shoreline. Peaks (antinodes) are compared against the $x = L/2$ line and valleys (nodes) against the $x = L/4$ line, both expected for a standing wave with an antinode at the shoreline.

4.3.4. Resonance

The mean spectrum indicated standing waves over the reef flat (Section 4.3.3), which is examined in more detail for 11 July (Section 4.4). This section assesses whether some frequencies may in addition be resonating, by comparing the fundamental mode frequencies of the open- and enclosed-basin configurations with the observed peak frequencies, and by examining whether the wave height is elevated relative to the transfer-function prediction (Section 3.2.8).

Fundamental period

Figure 4.11 shows the temporally varying fundamental period of the reef flat for the open-ended and enclosed-basin configurations over the full deployment period. The open-ended basin fundamental period has a mean of $575.5\,\mathrm{s}$ (range $423.8\,\mathrm{s}$ to $772.9\,\mathrm{s}$, mean $f_1^{\text{open}} = 0.001\,75\,\mathrm{Hz}$) and therefore falls in the VLF range. The enclosed-basin fundamental period has a mean of $287.8\,\mathrm{s}$ (range $211.9\,\mathrm{s}$ to $386.4\,\mathrm{s}$, mean $f_1^{\text{closed}} = 0.003\,51\,\mathrm{Hz}$) and falls in the IG range.

This temporal variability of the fundamental modes reflects changes in water depth across the reef flat. Given the comparatively small tidal range at the site, this variability is dominated by wave set-up, which can reach up to $1.20\,\mathrm{m}$ during the most energetic events, as shown in Section 4.3.1. This leads to a decrease in the fundamental period, as seen in Figure 4.11.

The assessment in this study is limited to the fundamental mode for the open-ended basin formulation. Higher-order modes may also be present, but the fundamental mode is expected to be the dominant resonant frequency (Gawehn et al. 2016), and therefore only this mode is considered here as a first assessment. It is, however, acknowledged that higher-order open-ended basin modes may fall in the IG range, so this configuration is not necessarily confined to the VLF range.

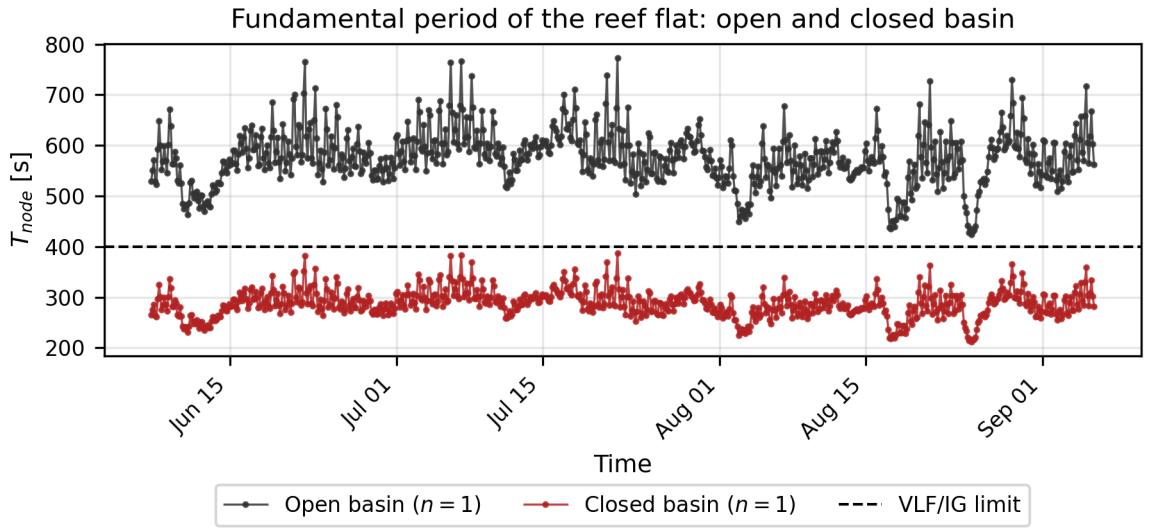


Figure 4.11: Temporally varying fundamental period T_{node} of the reef flat, for the open-ended basin and closed-basin configurations, over the full deployment period.

IG peak frequency comparison

The IG peak frequency of every spectrum was compared with the enclosed-basin mode (Section 3.2.8), with the results shown in Appendix G.

It was found that, as expected from the peak shift in Section 4.3.1, the dominant cluster shifts between modes across the reef flat, lying near $n = 1$ at RF5 and RF7 furthest from the shoreline, near $n = 2$ at RF1 and RF3, and between $n = 1$ and $n = 2$ at RF4. A slight elevation is present in $H_{s,IG}$ where the peak coincides with an eigenmode, but after normalisation by the transfer function this disappears, and the normalised wave height shows no pronounced maximum at an integer ratio. There is therefore no clear indication of resonant amplification in the IG band for this enclosed-basin formulation.

VLF peak frequency comparison

For the VLF band the reef flat is treated as an open-ended basin (Section 3.2.8). Figure 4.12 plots observed and normalised $H_{s,VLF}$ at RF1 against the ratio of the RS2 peak frequency to the fundamental.

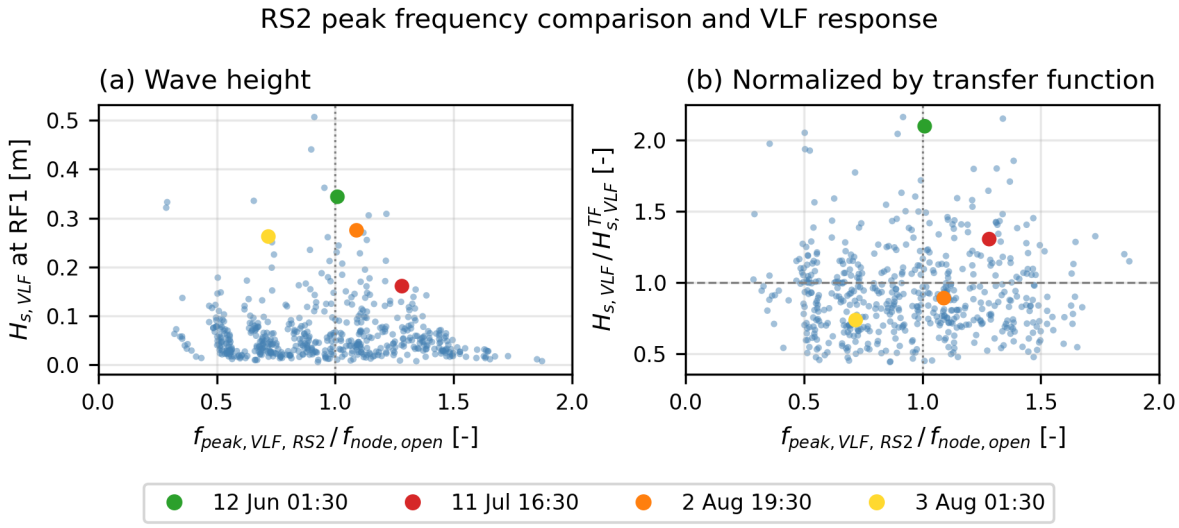


Figure 4.12: $H_{s,VLF}$ at RF1 against the ratio of the offshore VLF peak frequency at RS2 to the open-basin fundamental. (a) shows the raw $H_{s,VLF}$ and (b) shows $H_{s,VLF}$ normalised by the transfer-function prediction $H^{TF}_{s,VLF}$. The four cases examined in more detail are highlighted.

Figure 4.12(a) shows that the largest $H_{s,VLF}$ values occur near a ratio of one. After normalisation by the transfer function in (b), these higher values largely disappear, so they are for a large part explained by the offshore forcing.

Four cases are highlighted for closer examination below. The first two, on 2 and 3 August, were selected because Section 4.3.1 showed that at these times the band-integrated $H_{s,VLF}$ was higher at RF1 than at RF7. Such an onshore increase is typical of a resonant response in an open-ended basin, with a node at the crest and an antinode at the shoreline. These two show elevated values in the wave-height response, but this elevation does not emerge after normalisation by the transfer function. The third case, on 12 June, was included because its normalised wave height was clearly elevated and its frequency ratio lies close to one. The fourth, on 11 July 16:30, is the day examined in detail in Section 4.4, and is included to show where that day sits in this figure.

Spectral indications for VLF resonant behaviour

For the highlighted cases, the cross-shore spectra were examined together with the band-integrated $H_{s,VLF}$ and the narrow-band H_{eq} around the RF1 peak frequency, to see whether a node-antinode structure is present.

Figure 4.13 shows the case of 2 August 19:30. The spectral valley near the reef crest at RF7 coincides with the open-ended basin eigenfrequency, and the energy around this frequency grows onshore to a peak at RF1. This node near the crest and antinode further onshore matches the structure expected for a standing wave at the fundamental mode. Both peaks lie close to the fundamental, with a ratio of 1.09 for the RS2 peak and 0.95 for the RF1 peak.

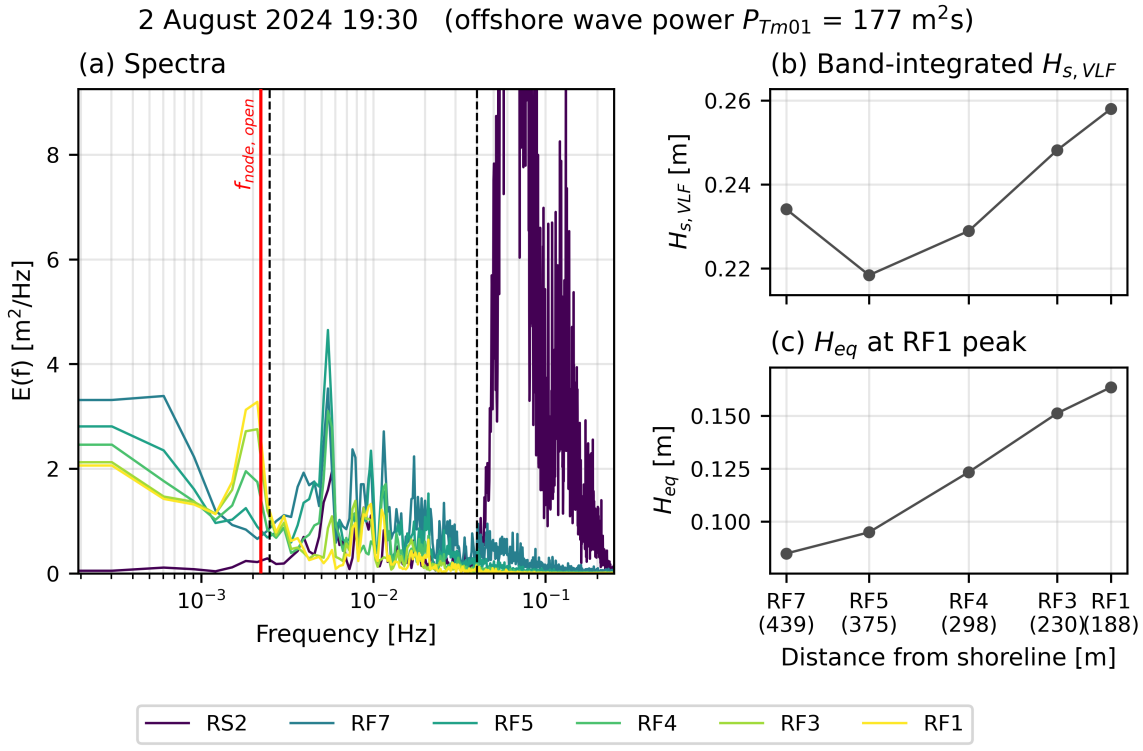


Figure 4.13: Cross-shore VLF response on 2 August 2024 19:30. (a) shows the energy density spectrum at each reef-flat sensor, with the red line marking the open-ended basin eigenfrequency $f_{node,open} = 0.002\,22\,\mathrm{Hz}$ at that moment. (b) shows the band-integrated $H_{s,VLF}$ (top) and the narrow-band H_{eq} around the RF1 peak frequency (bottom) at each reef-flat sensor. Together they show whether the energy at the eigenfrequency grows toward the shoreline, as expected between a node at the reef crest and an antinode at the shoreline. The offshore peak at RS2 lies at $0.002\,42\,\mathrm{Hz}$ and the RF1 peak at $0.002\,12\,\mathrm{Hz}$, giving ratios to the fundamental of 1.09 and 0.95, respectively.

Shortly after this response, on 3 August (Figure H.1 in Appendix H), a similar pattern may still be roughly visible, although with ratios of 0.72 for the RS2 peak and 0.43 for the RF1 peak it lies further from the fundamental mode.

Figure 4.14 shows the case of 12 June, which had a high normalised wave height. Little energy is present in the IG range, and the energy that is generated instead falls in the VLF range. Here the offshore peak coincides with the fundamental mode (ratio of 1.01), whereas the RF1 peak gives 0.72. RF7 was not available during this record, but the cross-shore structure still suggests a possible resonant response. For the fourth case, on 11 July 16:30 (Figure H.2 in Appendix H), the spectrum shows no indication of a resonant response. This holds for all spectra of that day, so resonance is not considered further in Section 4.4.

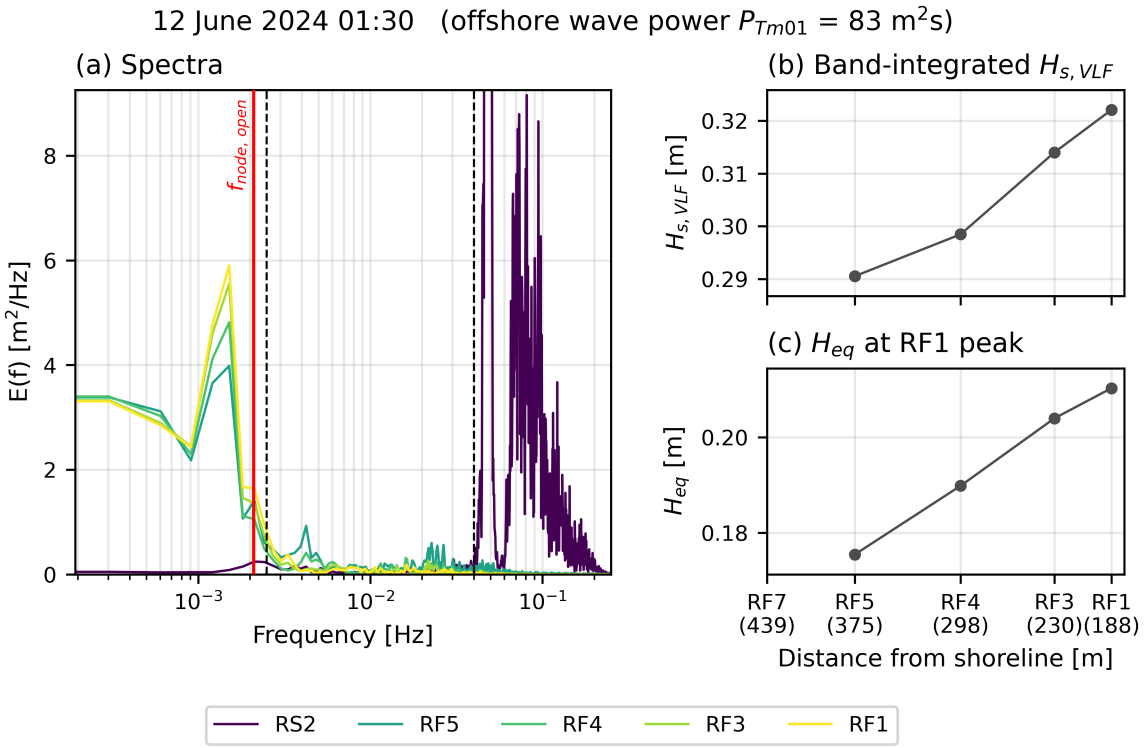


Figure 4.14: Cross-shore VLF response on 12 June 2024 01:30. (a) shows the energy density spectrum at each reef-flat sensor, with the red line marking the open-ended basin eigenfrequency $f_{node,open} = 0.002\,10\,\mathrm{Hz}$ at that moment. (b) shows the band-integrated $H_{s,VLF}$ (top) and the narrow-band H_{eq} around the RF1 peak frequency (bottom) at each reef-flat sensor. The offshore peak at RS2 lies at $0.002\,12\,\mathrm{Hz}$ and the RF1 peak at $0.001\,52\,\mathrm{Hz}$, giving ratios to the fundamental of 1.01 and 0.72, respectively. RF7 was not available during this record, so the sensor closest to the reef crest is RF5.

In all cases the ratio based on the RF1 peak is lower than the ratio based on the RS2 peak. A possible explanation for this is discussed in Section 5.5.1.

4.4. Detailed observations on 11 July 2024

On 11 July 2024 two additional records were available. The cross-shore array extended to $20\,\mathrm{m}$ from the shoreline through the ADV-lidar, and run-up data were obtained from the video camera during several intervals of that day. This section therefore examines this day in detail, with a focus on the hydrodynamics close to and at the shoreline. Section 4.4.1 presents the hydrodynamic parameters, including the wave directional properties, Section 4.4.2 addresses reflection near the shoreline together with the standing-wave patterns, and Section 4.4.3 presents the run-up analysis.

4.4.1. Hydrodynamic parameters during 11 July

This subsection characterises the wave field and the water levels on 11 July. The offshore forcing and the temporal evolution of the bulk wave parameters across the transect are presented first, followed by the wave directional properties and, finally, the cross-shore evolution averaged over a near-stationary part of the day (Section 4.4.1).

Offshore forcing

Figure 4.15 shows the hydrodynamic parameters at RS2, RF7, RF1, and the ADV-lidar over 11 July 2024. The offshore GW significant wave height at RS2 varied between approximately $1.48\,\mathrm{m}$ and $2.36\,\mathrm{m}$ over the course of the day (Figure 4.15c). Over part of the day the conditions were near-stationary. This was the case between approximately 9h and 21h, indicated by the shaded area in Figure 4.15, and this window was therefore selected for further analysis. Unless stated otherwise, all values reported in this section are averages over this window.

Over this window the offshore $H_{s,GW}$ at RS2 was $2.24\,\mathrm{m}$, with a GW peak period of $16.3\,\mathrm{s}$, which falls within the highest $15\,\%$ of the $H_{s,GW}$ values recorded at RS2 during the study period. On the reef flat, $H_{s,IG}$ and $H_{s,VLF}$ at RF1 both fall within the highest $10\,\%$ of their respective study-period records. The 11 July record is therefore considered moderately energetic, lying well above the study-period mean but well below the most energetic event of the campaign, during which $H_{s,GW}$ reached $5.46\,\mathrm{m}$.

Wave periods

The mean GW period across the transect is shown in Figure 4.15b. $T_{m01,GW}$ was similar at the reef crest and at the shoreline, at $10.8\,\mathrm{s}$ at RF7 and $11.4\,\mathrm{s}$ at the ADV-lidar.

The IG peak period, in contrast, varied across the transect (not shown in Figure 4.15). $T_{p,IG}$ was highest at the reef crest ($297\,\mathrm{s}$ at RF7), decreased to $180\,\mathrm{s}$ at RF1, and was $262\,\mathrm{s}$ at the ADV-lidar. This IG peak shift is consistent with the cross-shore shift observed over the full study period (Section 4.3.1) and with the presence of standing-wave patterns, which is examined further for this day in Section 4.4.2.

Water levels

The tidal level varied between $-0.13\,\mathrm{m}$ and $-0.06\,\mathrm{m}$ (mean $-0.09\,\mathrm{m}$) relative to the RGR92 datum (Figure 4.15a). The wave set-up increased towards the shoreline (Figure 4.15f), from $0.34\,\mathrm{m}$ to $0.41\,\mathrm{m}$ at RF7 (mean $0.38\,\mathrm{m}$) to $0.36\,\mathrm{m}$ to $0.45\,\mathrm{m}$ at RF1 (mean $0.42\,\mathrm{m}$), and was $0.35\,\mathrm{m}$ to $0.44\,\mathrm{m}$ at the ADV-lidar (mean $0.40\,\mathrm{m}$). In absolute terms, the mean water depth over the reef flat was $1.2\,\mathrm{m}$.

Wave heights

The cross-shore evolution of the significant wave height in each band is shown in Figure 4.15c–e. $H_{s,GW}$ decreased monotonically across the array, from a mean of $2.24\,\mathrm{m}$ at RS2 to $0.42\,\mathrm{m}$ at RF7, $0.06\,\mathrm{m}$ at RF1, and $0.05\,\mathrm{m}$ at the ADV-lidar, a reduction of $97.8\,\%$ between RS2 and the shoreline, consistent with depth-limited breaking over the reef slope and continued dissipation across the reef flat.

$H_{s,IG}$ and $H_{s,VLF}$, in contrast, both peaked at the reef crest (RF7), at $0.47\,\mathrm{m}$ and $0.23\,\mathrm{m}$ respectively, well above their offshore values at RS2 ($0.21\,\mathrm{m}$ and $0.04\,\mathrm{m}$). Both then decreased toward the mid-reef, to $0.18\,\mathrm{m}$ ($H_{s,IG}$) and $0.16\,\mathrm{m}$ ($H_{s,VLF}$) at RF1, after which $H_{s,IG}$ increased again toward the shoreline ($0.23\,\mathrm{m}$ at the ADV-lidar) while $H_{s,VLF}$ remained comparatively constant ($0.16\,\mathrm{m}$ at the ADV-lidar). The cross-shore pattern thus follows the campaign-mean behaviour described in Section 4.3.1, except that $H_{s,IG}$ increases again toward the shoreline.

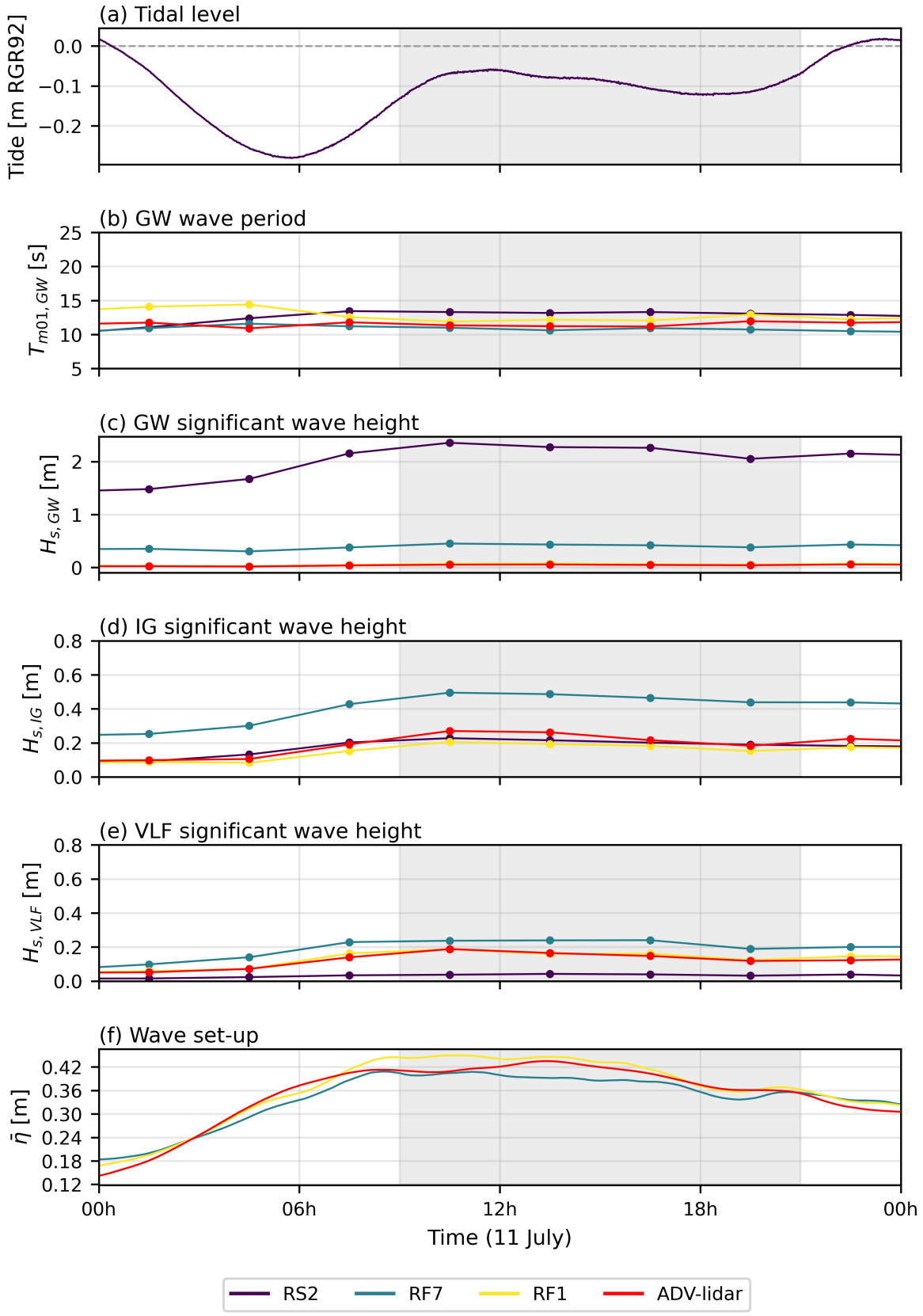


Figure 4.15: Hydrodynamic parameters at RS2, RF7, and RF1, and the ADV-lidar record near the shoreline (red), on 11 July 2024: (a) tidal level relative to the RGR92 datum, (b) mean GW period $T_{m01,GW}$, the significant wave height in each band, (c) $H_{s,GW}$, (d) $H_{s,IG}$ and (e) $H_{s,VLF}$, and (f) wave set-up $\bar{\eta}$ at the three reef-flat sensors. In (c), and over part of the record in (e), the RF1 (yellow) and ADV-lidar (red) lines coincide. The shaded area marks the near-stationary window (9h–21h) used in the subsequent analysis, during which the mean offshore wave power was $P_{Tm01} = 66.2\,\mathrm{m^2\,s}$.

Wave directional properties

The directional properties on 11 July were analysed at three cross-shore stations, ADV3 near the reef crest, ADV1 at the mid-reef (co-located with RF1), and the ADV-lidar near the shoreline. Figure 4.16 shows the temporal evolution of the mean wave angle $\bar{\theta}$ per band, and Table 4.5 lists the station means of $\bar{\theta}$ and of the directional spread $\bar{\delta}$ over the near-stationary window (Section 3.2.6). Here $\bar{\theta} = 0°$ denotes cross-shore and $\bar{\theta} = \pm 90°$ alongshore motion, with positive values indicating rotation toward the southeast-directed longshore direction.

The ADV-lidar was analysed over $3\,\mathrm{h}$ windows, and in addition over the same $30\,\mathrm{min}$ burst windows as ADV3 and ADV1, shown as the black dashed line in Figure 4.16. The $30\,\mathrm{min}$ estimates are more variable than the $3\,\mathrm{h}$ estimates, most clearly in the IG band, where they scatter by about $\pm 18°$ about the $3\,\mathrm{h}$ line and include one outlier of roughly $50°$. The mean values are nonetheless comparable between the two window lengths, so the shorter window mainly adds scatter rather than shifting the result. This should be kept in mind when interpreting the individual $30\,\mathrm{min}$ bursts at ADV3 and ADV1.

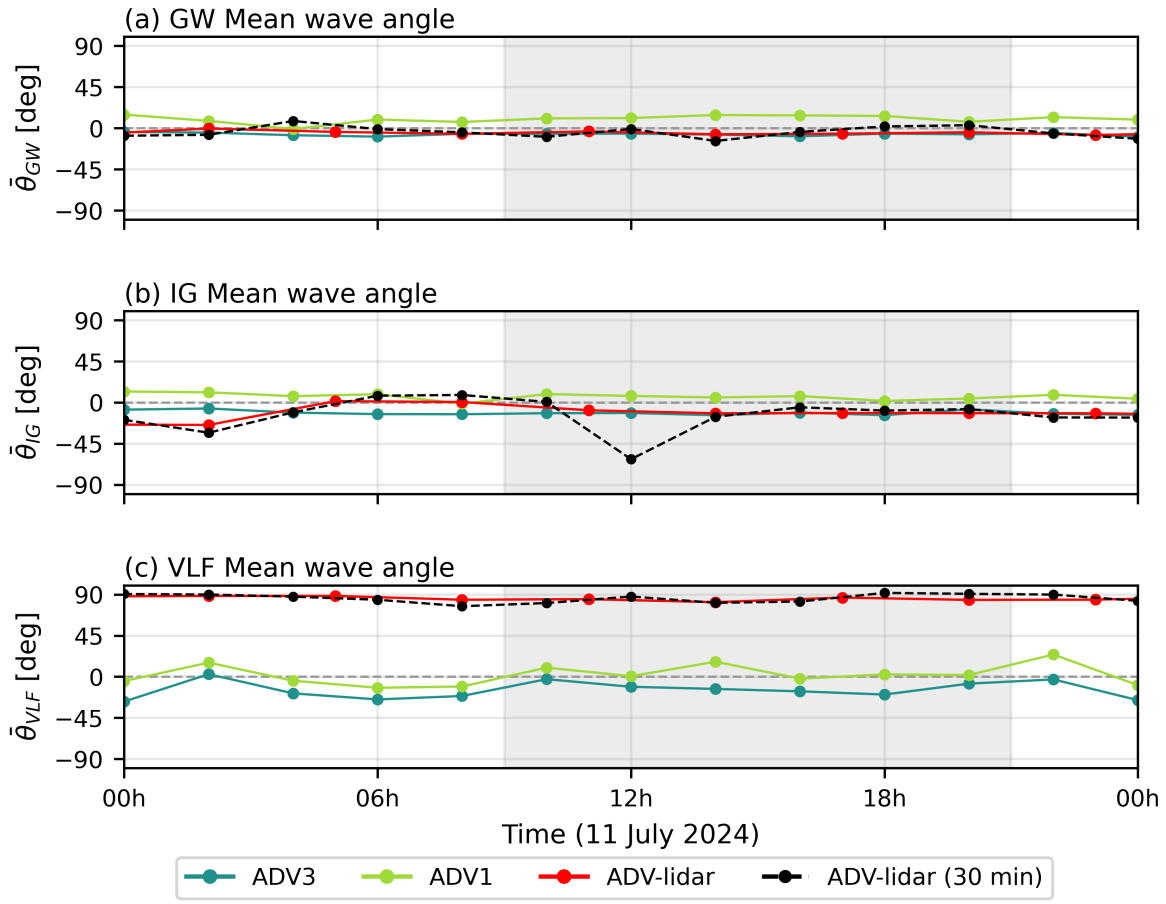


Figure 4.16: Mean wave angle $\bar{\theta}$ for the (a) GW, (b) IG, and (c) VLF bands at ADV3, ADV1, and the ADV-lidar on 11 July 2024. For ADV1 and ADV3 each point is a $30\,\mathrm{min}$ burst; for the ADV-lidar the estimates (red) use $3\,\mathrm{h}$ windows, with an additional $30\,\mathrm{min}$ estimate over the same burst windows as the other stations shown as the black dashed line. $\bar{\theta}$ is measured relative to the cross-shore direction (positive values indicate rotation towards the southeast longshore direction). The shaded area marks the near-stationary window (9h–21h).

In the GW band, $\bar{\theta}_{GW}$ was $-6.8°$ at ADV3, $11.7°$ at ADV1, and $-5.2°$ at the ADV-lidar (Figure 4.16a). The IG band behaved similarly, with $\bar{\theta}_{IG}$ of $-11.6°$ at ADV3, $5.8°$ at ADV1, and $-11.0°$ at the ADV-lidar (Figure 4.16b). In both bands the differences between the stations are plausibly related to refraction over the cross- and longshore irregular reef bathymetry (Figure 3.2), and possibly to local flow perturbations around individual coral heads, since the ADVs were mounted close to the bed ($0.25\,\mathrm{m}$ to $0.30\,\mathrm{m}$ above bed, Table A.2).

Table 4.5: Mean $\bar{\theta}$ and $\bar{\delta}$ per band and station, averaged over the near-stationary window (9h–21h) on 11 July 2024. The angles are circular means over the doubled angle, since $\bar{\theta}$ defines an axis.

Band	Sensor	$\bar{\theta}$ [deg]	$\bar{\delta}$ [–]
GW	ADV3	-6.8	0.3
GW	ADV1	11.7	0.5
GW	ADV-lidar	-5.2	0.6
IG	ADV3	-11.6	0.3
IG	ADV1	5.8	0.3
IG	ADV-lidar	-11.0	0.6
VLF	ADV3	-11.7	0.3
VLF	ADV1	4.8	0.3
VLF	ADV-lidar	84.2	0.2

The VLF band behaved differently (Figure 4.16c). At ADV3 and ADV1, $\bar{\theta}_{VLF}$ was $-11.7°$ and $4.8°$, so mainly cross-shore directed. Close to the shoreline at the ADV-lidar, however, $\bar{\theta}_{VLF}$ was $84.2°$, so directed almost entirely alongshore. This alongshore motion corresponds to a narrow directional distribution ($\bar{\delta} = 0.2$). Near the shoreline the VLF motion is therefore a well-defined alongshore oscillation.

An alongshore-directed VLF motion near the shoreline raises the question whether it reflects a shear instability of the mean current rather than a free-surface wave. However, the velocity-to-pressure variance ratio found in Section 4.2 does not support a purely shear-driven interpretation, as the VLF ratio at the ADV-lidar was well below 1 (mean 0.31), possibly indicating an antinode of a (partially) standing wave field.

Cross-shore overview over the near-stationary window

The cross-shore evolution of all parameters, averaged over the near-stationary window, is summarised in Figure 4.17, which also shows the cross-shore evolution of the peak period.

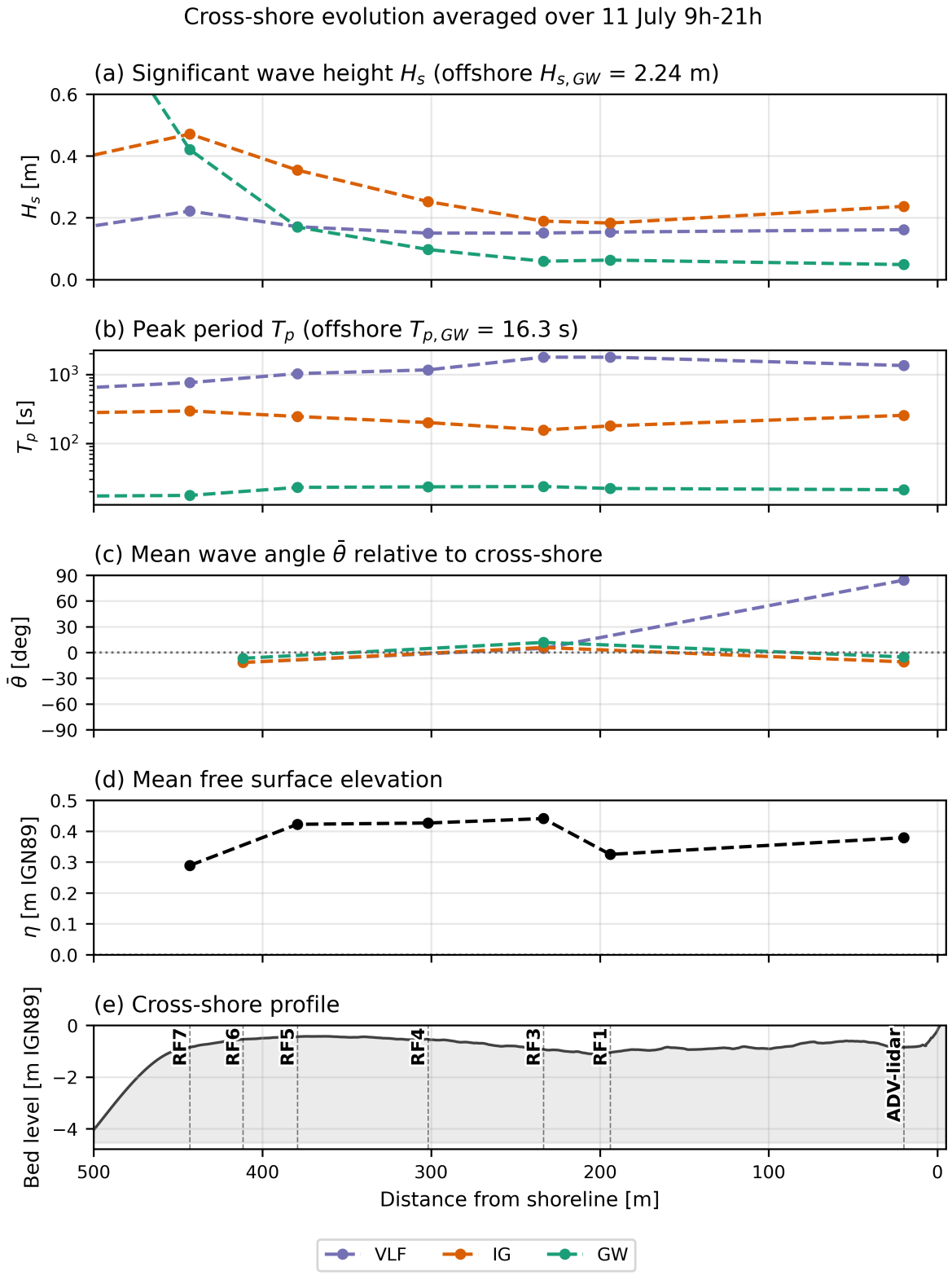


Figure 4.17: Cross-shore evolution of (a) significant wave height H_s, (b) peak period T_p, (c) mean wave angle $\bar{\theta}$, (d) mean free surface elevation η relative to the RGR92 datum, and (e) the cross-shore bed profile, averaged over the near-stationary window (9h–21h) on 11 July 2024. The averaging windows differ between bands and stations (Table 3.1), which should be kept in mind when comparing them directly.

4.4.2. Reflection and standing wave patterns

This section builds on Section 4.3.3, where standing patterns over the reef flat were already identified, now by including the reflection up to the shoreline. For ADV1 only two bursts are shown, as these were the only ones for which the pressure and velocity records were properly synchronised.

Figure 4.18 shows the temporal evolution of the reflection coefficient. The mean values reported here are again taken over the near-stationary window identified in Section 4.4.1, although K_r is largely constant throughout the day. Reflection is high in both the IG and VLF bands close to the shoreline (ADV-lidar), with a mean K_r of 1.06 and 1.03 respectively. K_r decreases with distance offshore in every band, dropping at ADV3 to 0.26 for IG and 0.38 for VLF. The GW band shows the lowest reflection of the three bands at both stations, with a mean K_r of 0.84 at the ADV-lidar and 0.21 at ADV3.

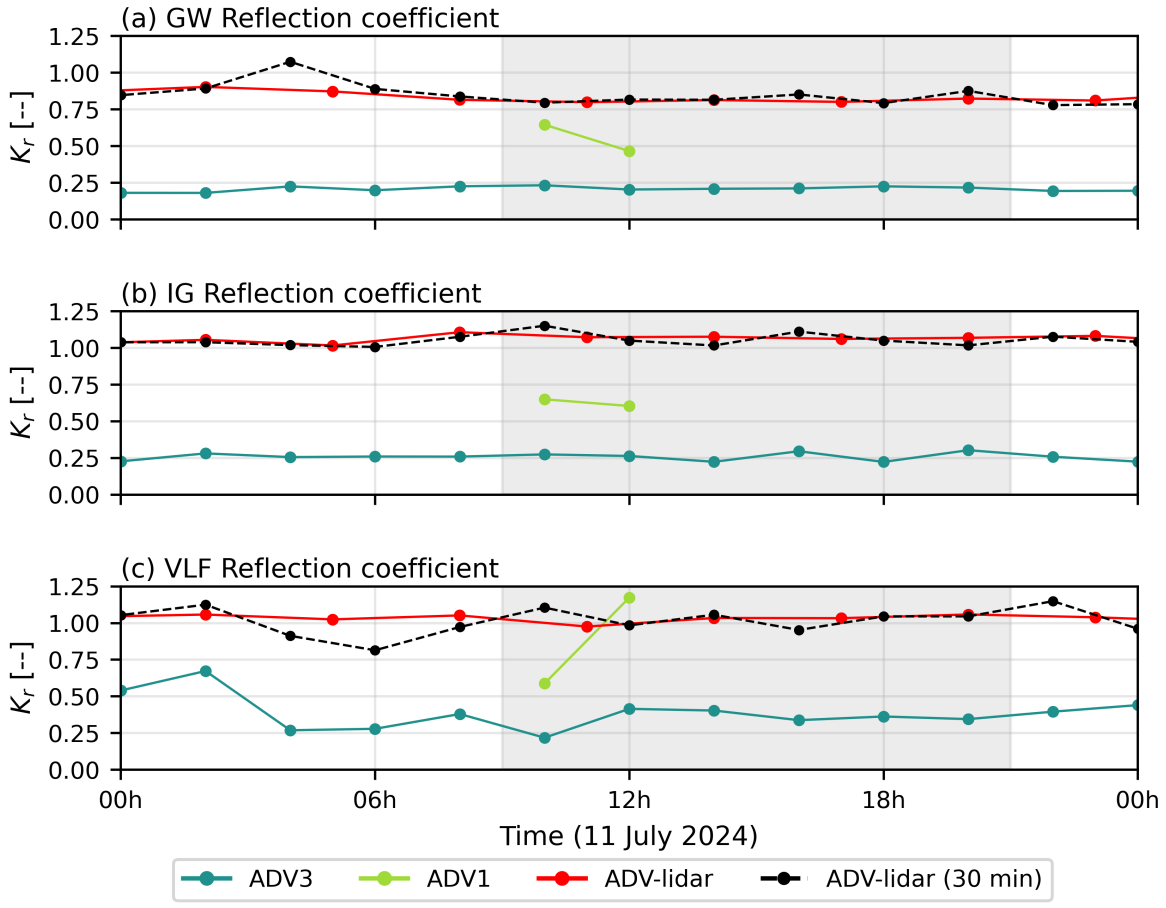


Figure 4.18: Reflection coefficient K_r for the (a) GW, (b) IG, and (c) VLF bands at ADV3, ADV1, and the ADV-lidar on 11 July 2024. For ADV1 and ADV3 each point is a $30\,\mathrm{min}$ burst; for the ADV-lidar the estimates use $3\,\mathrm{h}$ windows, with an additional $30\,\mathrm{min}$ estimate over the same burst windows as the other stations shown as the black dashed line. The shaded area marks the near-stationary window (9h–21h).

Figure 4.19 shows the incoming and outgoing spectra underlying these mean K_r values, together with a comparison of the total spectrum against the incoming spectrum and their sum.

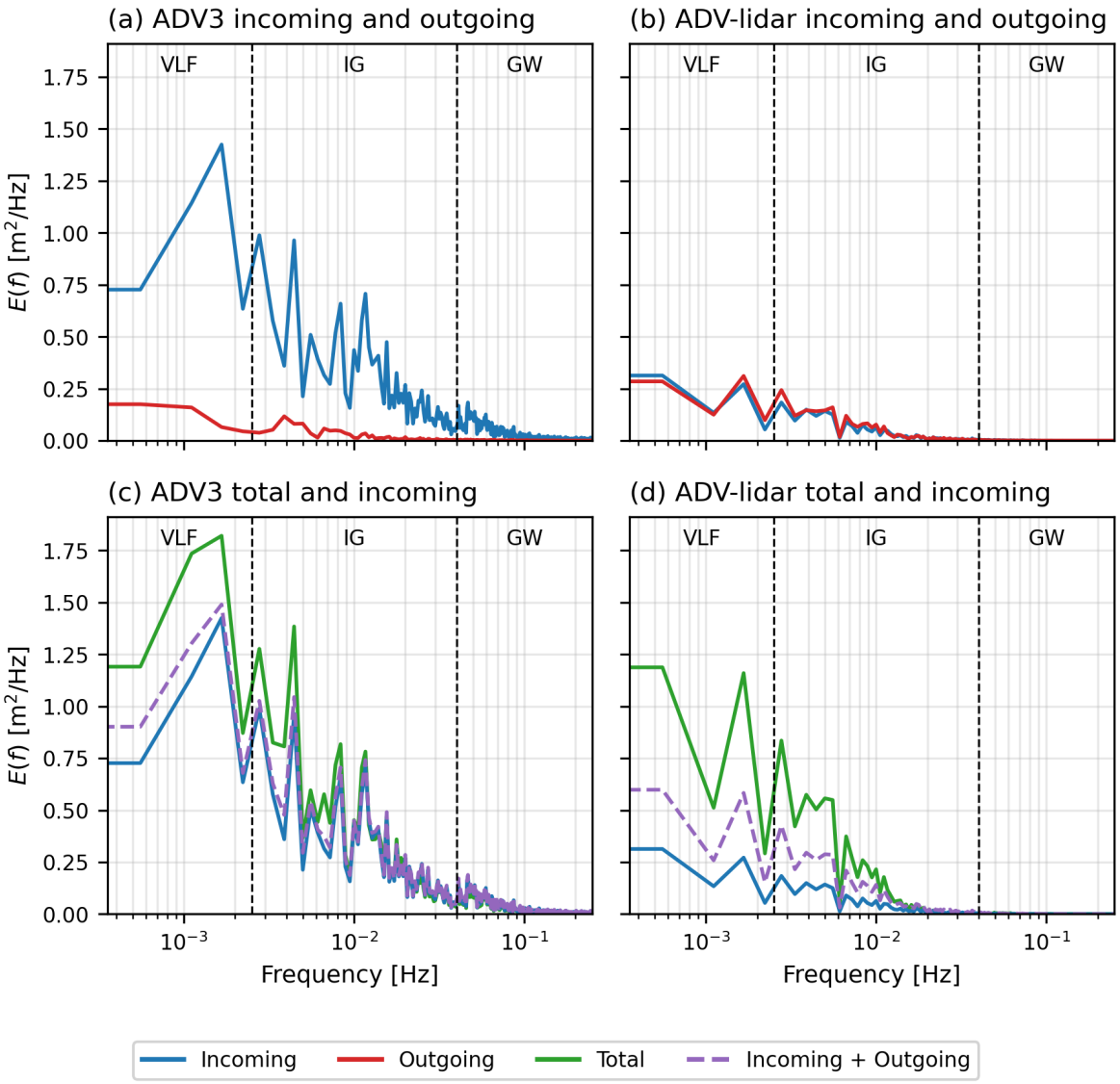


Figure 4.19: Spectra at ADV3 and the ADV-lidar on 11 July 2024: (a) incoming and outgoing spectra at ADV3, (b) incoming and outgoing spectra at the ADV-lidar, (c) total, incoming, and incoming + outgoing spectra at ADV3, and (d) total, incoming, and incoming + outgoing spectra at the ADV-lidar. The spectra are averaged over the 6 ADV3 bursts falling within the near-stationary window (9h–21h), with the same windows applied to the ADV-lidar so that the two stations can be compared directly.

At ADV3, the incoming spectrum exceeds the outgoing spectrum in all three bands (Figure 4.19a). This can be attributed to dissipation, since the outgoing component has crossed the reef flat in both directions before reaching this station. The ratio between the incoming and outgoing spectra is moreover not uniform across frequencies within a band, suggesting that the reflection coefficient may itself vary with frequency rather than being represented by a single value per band. Two factors may play a role. First, more incident energy is present at the lower frequencies to begin with. Second, higher frequencies dissipate more strongly (Lowe et al. 2007), so less of their energy reaches the shoreline to be reflected. Band-integrated parameters such as $H_{s,IG}$, K_r and N average over this variation and may therefore mask standing behaviour that is present only in the lower part of the band. Given the uncertainty on the individual spectral estimates, which is further addressed in Section 5.1, this cannot be established conclusively.

Figure 4.19c,d compares the total spectrum with the incoming spectrum and with the sum of the incoming and outgoing spectra. At the ADV-lidar the total spectrum exceeds this sum across the VLF

and IG bands. This follows from the decomposition itself, in which the surface elevation is split into an incoming and a reflected component, $\eta = \eta_{\text{inc}} + \eta_{\text{ref}}$ (Section 2.3.2). Since the energy is proportional to the variance of the surface elevation, $E \propto \langle \eta^2 \rangle$, squaring this sum and averaging gives:

$$\langle \eta^2 \rangle = \langle \eta_{\text{inc}}^2 \rangle + \langle \eta_{\text{ref}}^2 \rangle + 2 \langle \eta_{\text{inc}}\, \eta_{\text{ref}} \rangle \tag{4.1}$$

Here $\langle \eta_{\text{inc}}^2 \rangle$ and $\langle \eta_{\text{ref}}^2 \rangle$ give the energy of the incoming and the reflected wave, and the cross term $2 \langle \eta_{\text{inc}}\, \eta_{\text{ref}} \rangle$ gives an additional interference term E_{int}, so that:

$$E_{\text{total}}(f) = E_{\text{inc}}(f) + E_{\text{ref}}(f) + E_{\text{int}}(f) \tag{4.2}$$

This interference term is positive where the incoming and reflected waves are in phase, that is, at an antinode. The spectra indicate that antinodes are present, although the uncertainty on the spectra restricts identifying at which frequencies exactly.

To assess whether the peak and valley frequency shift found in the campaign-averaged mean spectra is also present over a shorter period, the spectra of the full pressure-sensor array were examined again over the same near-stationary window (Figure 4.20). Unlike the incoming and outgoing spectra above, these are based on the continuous pressure-sensor records (Section 3.2.3). The same cross-shore shift is found. Peak and valley frequencies were identified for the reef-flat sensors only, since the ADV-lidar lies at the shoreline, and their shallow water wavelengths again correspond to the node and antinode locations expected for a standing wave with an antinode at the shoreline. This is shown in Appendix I, together with the cross-shore structure of the wave height at each sensor's peak frequency, determined using the narrow-band approach (Section 3.2.7).

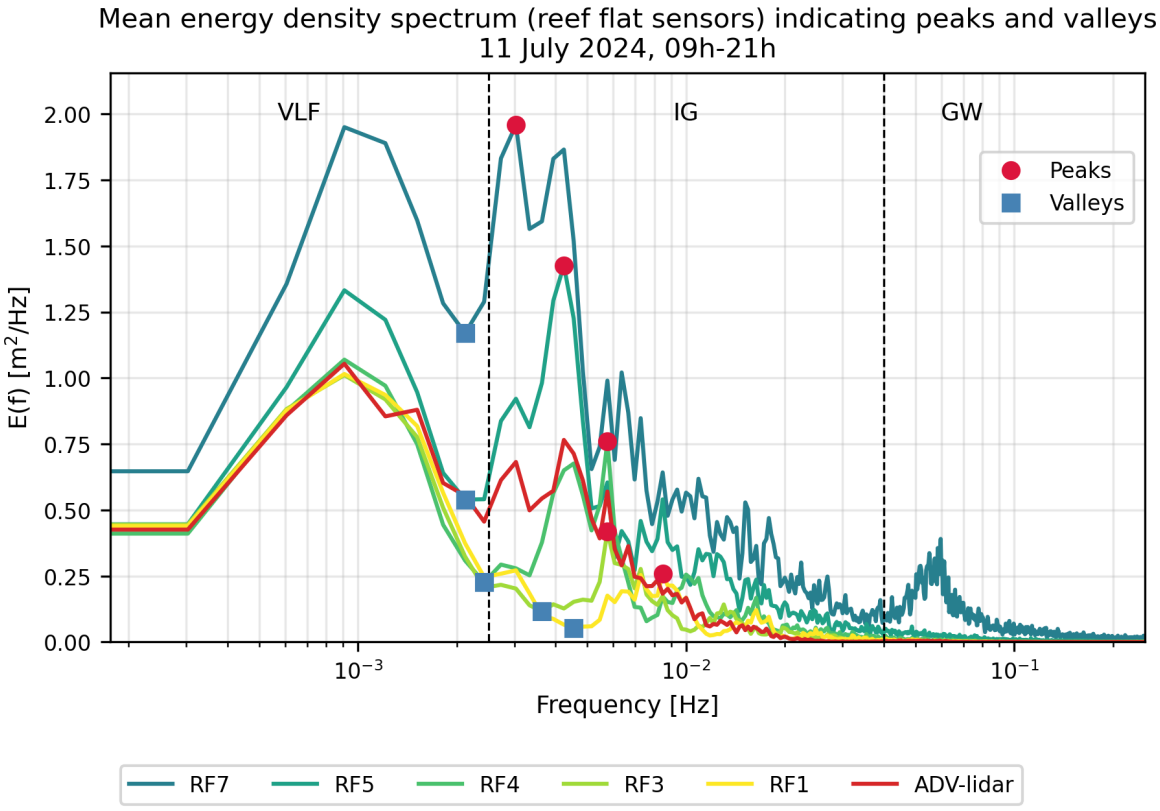


Figure 4.20: Mean energy density spectrum at each reef-flat sensor and at the ADV-lidar over the near-stationary window (9h–21h) on 11 July 2024, with the identified IG-band peak (red circles) and valley (blue squares) frequencies marked. No peak and valley are marked for the ADV-lidar, since it lies at the shoreline.

4.4.3. Run-up

The wave parameters presented so far reach up to $20\,\mathrm{m}$ from the shoreline (ADV-lidar). To characterise the total water level at the shoreline itself, the analysis is now extended to the run-up. The $2\,\%$ exceedance level was determined over a $1\,\mathrm{h}$ window, from 13h to 14h, which falls within the longest continuous run-up segment (Appendix D).

Figure 4.21 shows the separate contributions of the set-up and of the GW, IG, and VLF components. Expressed relative to the offshore still water level, $R_{2\%}$ was $0.91\,\mathrm{m}$ and $\eta_{2\%}$ at the ADV-lidar was $0.71\,\mathrm{m}$. Set-up was the largest term in both records, contributing $0.60\,\mathrm{m}$ ($65.9\,\%$) to $R_{2\%}$ and $0.45\,\mathrm{m}$ ($63.4\,\%$) to $\eta_{2\%}$. Among the oscillatory wave bands, IG dominated at both locations, at $0.26\,\mathrm{m}$ ($28.6\,\%$) in the run-up and $0.19\,\mathrm{m}$ ($26.8\,\%$) at the ADV-lidar. The GW contribution was small, at $0.03\,\mathrm{m}$ ($3.3\,\%$) in the run-up and $0.02\,\mathrm{m}$ ($2.8\,\%$) at the ADV-lidar. The VLF contribution, in contrast, was smaller in the run-up ($0.02\,\mathrm{m}$, $2.2\,\%$) than at the ADV-lidar ($0.05\,\mathrm{m}$, $7.0\,\%$), whereas all other terms increased over the final $20\,\mathrm{m}$ to the shoreline.

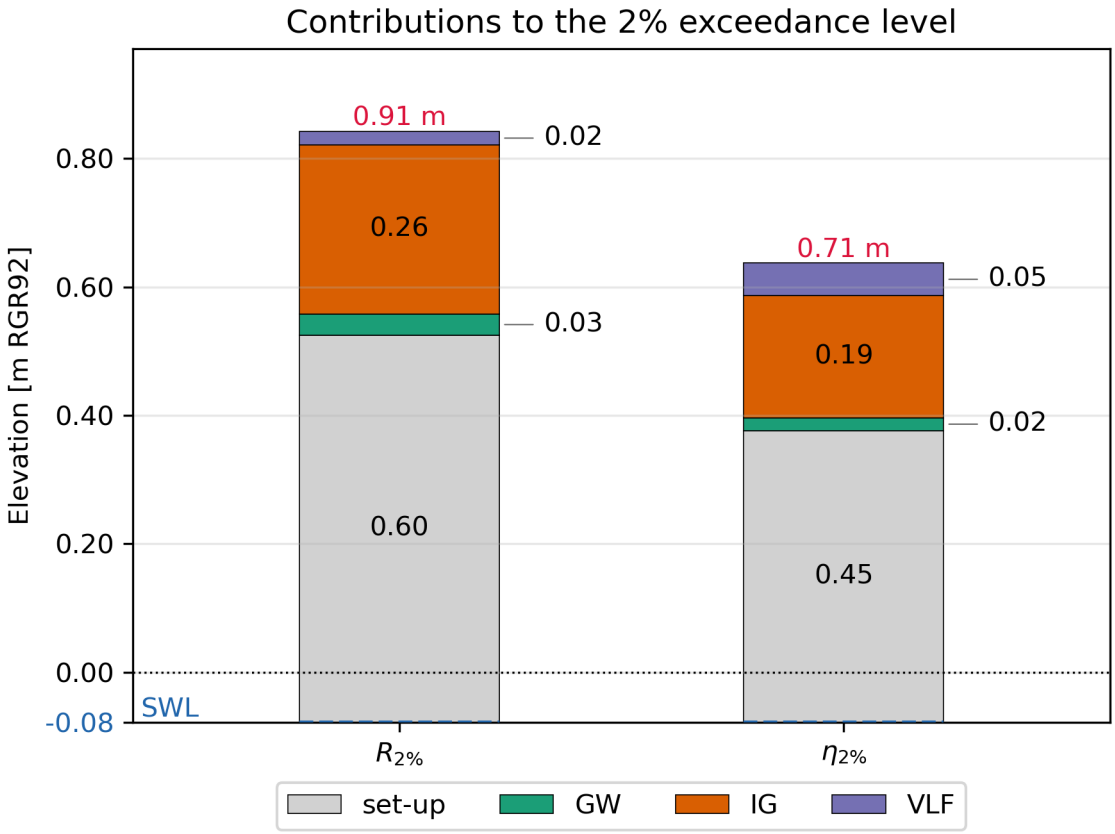


Figure 4.21: Contributions of the set-up and of the GW, IG, and VLF components to the $2\,\%$ exceedance level of the run-up ($R_{2\%}$) and of the ADV-lidar surface elevation ($\eta_{2\%}$), 11 July 2024, 13h–14h. The bars start at the offshore still water level (blue dashed line, $-0.08\,\mathrm{m}$ RGR92) and each block gives the contribution of that term in metres. The red number above each bar is the total $2\,\%$ exceedance level relative to the still water level. The dotted line marks the RGR92 vertical datum.

5

Discussion

The objective of this study was to identify the forcing conditions and processes governing the magnitude and spatial transformation of IG and VLF waves over La Saline fringing reef located on La Réunion. This chapter first discusses the limitations of the study and how they constrain the interpretation of the results (Section 5.1). The findings are then discussed in the subsequent sections.

5.1. Limitations

This section discusses the constraints regarding the data analysis and the measurement set-up.

5.1.1. VLF band limit choice

To analyse the wave field, frequency band limits were set. The band limits of the VLF band are the most uncertain part of this definition, as no clear physical frequency range for VLF motions has yet been established (Shimozono et al. 2022; Belkadi et al. 2024; Bruch et al. 2022; Cheriton et al. 2016). The limits were fixed beforehand, while the physical basis for this separation is itself part of what this study seeks to understand. This applies to both the upper and the lower limit of the VLF band.

Regarding the lower limit, the boundary of $0.0003\,\mathrm{Hz}$, corresponding to a period of approximately $55\,\mathrm{min}$, results from a methodological choice. It is therefore possible that residual slowly varying water-level contributions associated with changes in wave set-up or tidal level are classified as VLF energy. Such contributions may not represent the VLF surface-wave motions targeted in this study. As long as the processes responsible for VLF motions and their frequency range are not better constrained, this uncertainty in the band limits cannot fully be avoided.

These constraints are particularly relevant for analyses that aim to attribute the VLF variance to a specific process. This includes the resonance assessment, which relies partly on the band-integrated VLF response, and the velocity-to-pressure variance ratio N, for which the pressure variance may contain contributions that are not associated with VLF surface waves.

5.1.2. Spectral uncertainty and its propagation into the derived parameters

The choices made in the spectral analysis described in Section 3.2.3 result in a spectral resolution of $\Delta f = 0.0003\,\mathrm{Hz}$ and $M = 5$ averaged segments per window. The spectral estimates from Welch's method approximately follow a χ^2 distribution with $\nu = 2M = 10$ degrees of freedom (Rodríguez et al. 1999), which corresponds to a normalised standard error of $\varepsilon = \sqrt{2/\nu} \approx 45\,\%$ for an individual spectral estimate (Otnes and Enochson 1978).

The propagation of this uncertainty differs between the derived parameters. Band-integrated wave heights are relatively robust because variability in individual spectral estimates is reduced when energy is integrated over multiple frequency bins. In contrast, f_p depends on the location of a single spectral maximum and is therefore more sensitive to spectral variability and to the frequency resolution (Rodríguez et al. 1999).

These limitations are most pronounced in the VLF band, which contains only 8 frequency bins, compared with 123 in the IG band and 693 in the GW band. Consequently, $H_{s,VLF}$ is less robust than the corresponding IG and GW wave heights, while H_{eq} is even more sensitive because it is based on only 2 frequency bins. The VLF peak period is also particularly uncertain because Δf represents a relatively large fraction of f_p.

These uncertainties apply to all results derived from the spectra. The uncertainty in the peak frequency is relevant to the resonance assessments in both the IG and the VLF band, while the uncertainty in wave height is particularly important for the VLF transfer functions and the VLF resonance assessment.

5.1.3. Limitations of the velocity-based analyses

The ADV-derived parameters are additionally limited by the $30\,\mathrm{min}$ burst duration at ADV1 and ADV3. A VLF motion in particular is represented by only a few wave cycles within such a record, making the variances used to determine $\bar{\theta}$, $\bar{\delta}$, N, and K_r less robust than for the IG and GW bands.

Regarding the directional analyses, their interpretation also depends on whether the measured velocity variance can be attributed to VLF surface-wave motions. Rotational or shear-wave motions may also contribute to this variance and therefore influence the estimated wave direction and directional spread (Noyes et al. 2002).

The reflection coefficient is also affected by the wave direction, since the incoming and outgoing energy is separated only along the shore-normal direction in this study. As Winter et al. (2017) note, the energy flux of obliquely incident or reflected waves is distributed over both the cross-shore and the alongshore direction. If the incident and the reflected wave angle differ, changes in the reflection coefficient may therefore result not only from energy gain or loss within the band, but also from wave refraction.

Finally, the ADVs measured close to the bed where the flow can vary at the scale of individual coral colonies (Hench and Rosman 2013). The measured velocity direction may therefore partly reflect local flow around the instrument rather than the direction of the reef-scale flow.

5.1.4. Fundamental mode estimation and peak frequency comparison

The fundamental modes were estimated from an averaged bathymetric profile constructed from a limited number of cross-shore transects. Consequently, the full two-dimensional structure of the reef was not represented, and possible longshore effects on the fundamental modes were not addressed. Furthermore, a spatially constant water level was assumed over the reef flat, motivated by the relatively small differences in mean set-up between the sensor locations. This remains a simplification. Becker et al. (2014), for example, reported increases in set-up amplitude from the mid-reef towards the shoreline of $11\,\%$ and $16\,\%$ at two of their three fringing-reef study sites. The constant-water-level approximation is best justified under energetic conditions. The observed cross-reef differences in set-up did not increase with the offshore wave forcing and therefore become relatively small compared with the total water depth. These energetic conditions are also the most relevant for the present study.

Further simplifications concern the geometry and the boundary conditions used to calculate the fundamental mode. The seaward boundary of the domain was fixed at $450\,\mathrm{m}$ from the shoreline, based on the rapid change in bathymetric slope at this location. However, the precise location of the effective boundary is uncertain. In addition, the open-ended-basin assessment considered only the fundamental mode, while both configurations used the dominant peak frequency. Higher-order modes may also occur and, for the open-ended basin, may extend into the IG range.

Together, these simplifications add uncertainty to the resonance assessment.

5.1.5. VLF wave shape

The band-passed time series were obtained using an inverse Fourier transform. This may limit how accurately strongly nonlinear VLF wave shapes are represented. Gawehn et al. (2016) note that FFT-based methods have a limited ability to reproduce bore-like VLF waveforms. They propose the Hilbert–Huang transform as an alternative that better preserves such nonlinear waveforms, although at a higher computational cost. This limitation was not addressed in the present study. The shape of the VLF waves in the band-passed time series may therefore not be fully represented.

5.2. Offshore GW-driven, LF-dominated reef hydrodynamics

The mean reduction in $H_{s,GW}$ of $97.6\,\%$ between the reef slope and the mid-reef is consistent with the $97\,\%$ mean reduction in incident wave height reported by Bruch et al. (2022) at La Saline, and with observations at other fringing reefs (Cheriton et al. 2016; Gawehn et al. 2016; Ferrario et al. 2014). Furthermore, this study confirms the low-pass filtering effect of the reef, which is consistent with previous observations (Bruch et al. 2022; Beetham et al. 2016; Péquignet et al. 2014; Pomeroy et al. 2012a).

The transfer functions showed that at every reef-flat sensor, $H_{s,IG}$ and $H_{s,VLF}$ were best predicted by a combination of offshore wave power and the tidal component of the local water level (Tables 4.2 and 4.3). Offshore wave power explained most of the variance, on average $96\,\%$ for IG and $98\,\%$ for VLF. Bruch et al. (2022) obtained a comparable combination of offshore forcing and water level at the same site. Their transfer functions included offshore significant wave height, wave power, and water level as separate predictors. However, these predictors are not independent. Most of the explained variance was attributed to $H_{s,GW,RS}$ ($86\,\%$ for IG and $89\,\%$ for VLF) rather than to wave power. Both formulations nonetheless indicate that LF wave hydrodynamics are primarily controlled by offshore GW forcing, consistent with observations at other reefs (Beetham et al. 2016).

5.3. Spatial structure of the LF wave field

The spatial structure observed at La Saline is consistent with a partly standing LF wave field. Similar standing IG behaviour over reef flats has been reported in both laboratory experiments (Buckley et al. 2018) and field observations on fringing reefs (Péquignet et al. 2009; Becker et al. 2016). Besides cross-shore standing IG patterns, Winter et al. (2017) identified a local alongshore standing IG pattern over an alongshore-irregular rocky reef. They established this from the phase lags between every combination of surface elevation, cross- and longshore velocity, and between instruments separated in both the cross-shore and the alongshore direction. The present study did not identify the cross-shore standing waves from such a phase lag analysis. The analysis could nonetheless be extended in the same way for the cross-shore direction. This would make it possible to confirm which part of the LF range shows partly standing behaviour and how that behaviour develops under different offshore GW forcing events and water levels over the reef flat. However, such an analysis would still be constrained by the ADV data quality and burst duration.

Furthermore, no longshore variability was found with the present pressure sensor set-up. The sensors were spaced approximately $500\,\mathrm{m}$ apart at about $200\,\mathrm{m}$ from the shoreline. A suggestion would be to place the sensors at intervals smaller than a quarter of the expected standing-wave wavelength. At the mean reef-flat depth of $1\,\mathrm{m}$, the observed IG peak frequencies correspond to shallow-water wavelengths of approximately $400\,\mathrm{m}$ to $1000\,\mathrm{m}$. A spacing of the order of $100\,\mathrm{m}$ would therefore be more appropriate. This is also consistent with Winter et al. (2017), who used several sensors spaced approximately $50\,\mathrm{m}$ apart alongshore and identified alongshore standing waves at a water depth comparable to that at La Saline. VLF wavelengths range from approximately $1250\,\mathrm{m}$ to several kilometres. An alongshore standing pattern in this frequency range could therefore have been detected with the present sensor set-up, had such a pattern been present.

In addition to changing the sensor spacing, different locations on the reef flat could be examined in future measurements. For example, pressure and velocity sensors could be placed in the longshore direction closer to the shoreline, where the alongshore-directed VLF motion was observed. The origin of this direction was not established in the present study. One possibility is that it is related to the standing-wave pattern rather than to a separate process. At a surface-elevation antinode near the shoreline, the cross-shore velocity is small, so the horizontal velocity may be dominated by its longshore component. The remaining longshore velocity variance could still partly originate from shear motions. This may not be reflected in N, since the pressure variance is large at an antinode.

Alternatively, the observed longshore motion could be related to edge waves. Su and Ma (2018) found alongshore-propagating IG energy on a two-dimensional fringing reef with spatial characteristics consistent with edge-wave modes. Winter et al. (2017) also found phase relationships consistent with standing edge waves, but argued against this interpretation because classical edge-wave theory assumes an alongshore-uniform bathymetry. This assumption is not satisfied at La Saline either. They further note that a combined cross-shore and alongshore standing-wave pattern has a sinusoidal cross-

shore amplitude structure, whereas a standing edge wave follows a Laguerre-polynomial structure. Distinguishing between these mechanisms would therefore require more closely spaced cross-shore sensors, particularly towards the shoreline, to resolve the cross-shore amplitude structure.

5.4. Resonance in the enclosed-basin formulation

The present assessment gave no clear indication of resonance for the enclosed-basin formulation. Nevertheless, Appendix G shows that, at several locations, the ratio of the observed peak frequency to the fundamental frequency clusters around integer values. This could suggest that some of the IG spectral peaks may be related to (higher-order) enclosed-basin modes. However, the present analysis considered only the dominant spectral peak and may therefore not fully capture how energy is distributed around the different eigenmodes within the IG band. Buckley et al. (2018) report a comparable concentration of energy at the natural frequencies of the reef flat, although for an open-ended rather than an enclosed formulation.

This could be investigated further by adapting the approach of Buckley et al. (2018). They normalised the complete spectra by the incoming offshore wave energy and expressed frequency in terms of the ratio between the reef-flat length and the corresponding wavelength. Expressing frequency as L/λ places each eigenmode at a fixed position, allowing spectra from different water depths to be compared. Applying the same approach to the enclosed-basin formulation would show whether enhanced spectral energy consistently occurs around its eigenmodes, including when the dominant spectral peak lies at another frequency.

In addition, the boundaries of the enclosed basin would need a firmer basis for such an analysis. They are now placed at the shoreline and the reef crest, whereas a position that forms a clearer physical boundary may be more appropriate, for example at a location with a more pronounced change in bathymetry.

5.5. Possible VLF generation mechanisms

One possible generation mechanism for surface VLF waves reported in the literature is resonance following an open-ended basin configuration on the reef, that is, with a node at the reef crest and an antinode at the shoreline (Péquignet et al. 2009; Pomeroy et al. 2012b; Gawehn et al. 2016; Buckley et al. 2018). In this study, indications of resonant VLF behaviour were found as well, although this assessment in particular is affected by the limitations described in Section 5.1. However, it is likely that resonance is not the only mechanism involved, since the VLF band contained energy also at times when no resonance signature was present, and the campaign mean does not reflect a resonant response in the VLF band either. Another mechanism that could be explored further is therefore discussed as well, namely non-linear interactions between IG components generating VLF energy on the reef flat.

5.5.1. Resonance

In particular, individual spectra did imply a resonant response at certain times (e.g. Figure 4.14). However, these spectra also show that the VLF band contains energy not only around the peak close to the fundamental mode, but also in its lower part. This supports the earlier question of what is included in the VLF band under the present definition (Section 5.1.1).

Furthermore, this resonance assessment can be questioned on the same grounds. The whole band-integrated $H_{s,VLF}$ is used as the response, so such influences may be reflected here as well. A resonant response confined to a narrow frequency range may then not show up in the assessment. Using a narrower range would be a way to test this, with the lower bound of the VLF band placed at a higher frequency but ensuring that the fundamental mode still falls within it.

However, the choice of such a boundary is not straightforward. The results showed that the frequency of the peak response on the reef flat lies below the fundamental frequency (e.g. Figure 4.14). This is even more apparent in Figure 5.1, where the response at RF1 peaks at ratios below one. Referenced to the offshore peak frequency at RS2, the same response is largest near a ratio of one (Figure 4.12). A comparable difference was reported at the same site by Bruch et al. (2022), who observed a mean VLF period of $18\,\mathrm{min}$ against a fundamental mode of $15\,\mathrm{min}$. The same difference has been found in numerical experiments. Lasserre et al. (2020) obtained maximum resonance at longer periods than

the theoretical resonant periods of their schematised reef, consistent with Pearson et al. (2017).

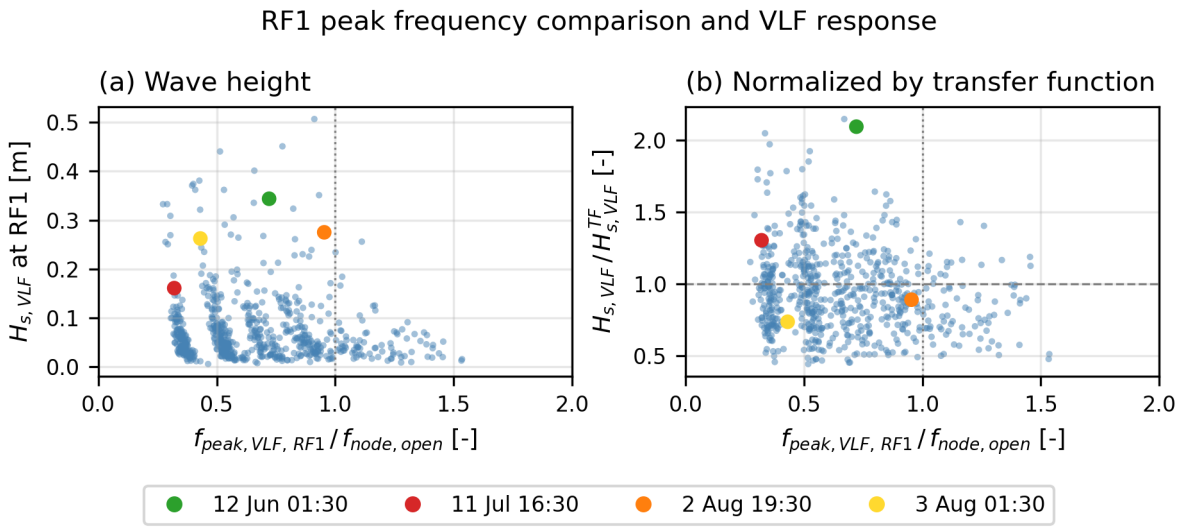


Figure 5.1: $H_{s,VLF}$ at RF1 against the ratio of the VLF peak frequency at RF1 to the open-basin fundamental. (a) shows the raw $H_{s,VLF}$ and (b) shows $H_{s,VLF}$ normalised by the transfer-function prediction $H^{TF}_{s,VLF}$. The highlighted cases are the same as in Figure 4.12, in which the offshore VLF peak frequency at RS2 is used as the reference instead. Whereas the response in that figure is largest near a ratio of one, the response at RF1 peaks at ratios below one.

This behaviour could potentially be linked to the reef flat acting as a damped system, in which the damping is provided by, among others, the friction of the reef. Although not reported in the context of fringing reefs, the effect itself is well known. The classic steady-state harmonic response of a damped oscillator shows that the frequency of maximum response lies below the undamped fundamental frequency, and that this frequency ratio decreases further as the damping ratio increases (Rao 2011), as illustrated in Figure 5.2a. The phase lag of the displacement with respect to the applied force behaves similarly. Without damping it changes abruptly from $0°$ to $180°$ at the fundamental frequency, whereas with damping the transition becomes more gradual (Figure 5.2b). To better study this damping effect, the present study could be extended by including the envelope of the offshore forcing and comparing it directly to the envelope over the reef flat, and by determining the phase lag between the two under potentially resonant conditions, such as those identified in this study.

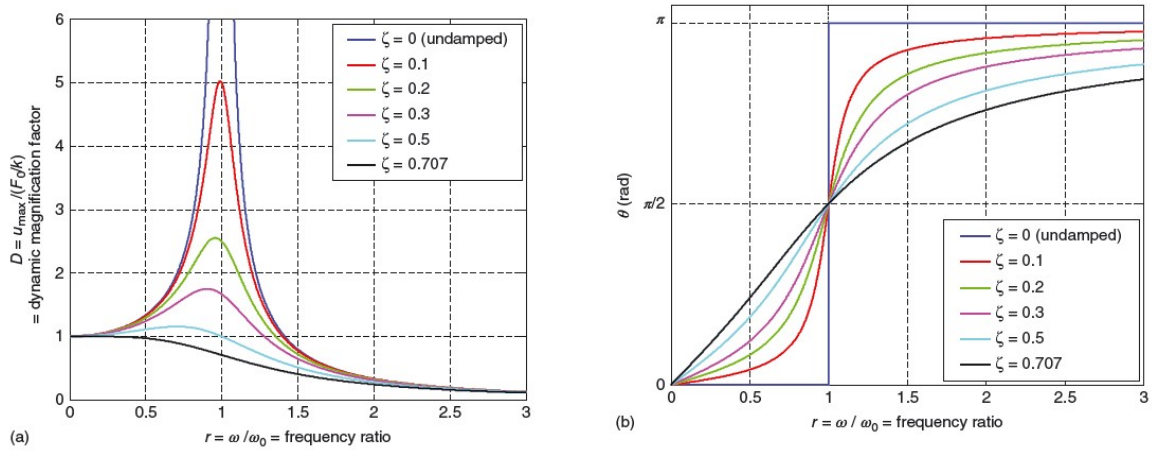


Figure 5.2: Steady-state harmonic response of a damped oscillator. (a) Amplitude of the response against the ratio of the forcing frequency to the undamped natural frequency, for increasing damping ratio (ζ). (b) Phase lag of the displacement with respect to the applied force. Adapted from Heinrich and Dufour (2015).

5.5.2. Non-linear LF interactions

Besides a purely resonant response, other generation mechanisms could be considered. The spectra obtained in this study could point to non-linear triad interactions between IG components leading to VLF energy on the reef flat. This is suggested by a comparison between the difference of two IG-band peak frequencies identified in the mean spectrum and the observed VLF peak frequency. Figure 5.3 shows the campaign-mean spectrum at RF7, RF5 and RF3, with the highest IG-band peak and a smaller secondary peak close to it identified at each sensor. The difference between these two frequencies coincides closely with the observed VLF peak frequency at all three stations. Applying the same approach to the mean spectrum on 11 July (Figure J.1) also shows this to some extent. However, this assessment is highly limited by the frequency resolution and the uncertainty reported earlier.

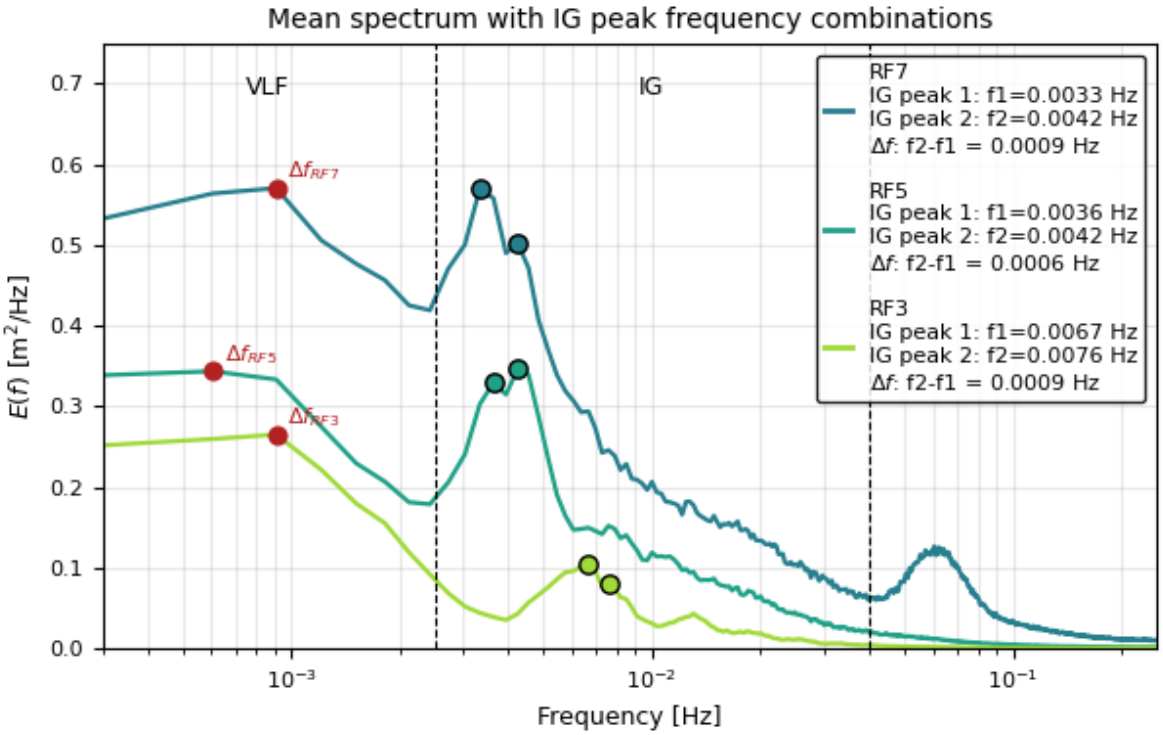


Figure 5.3: Campaign-mean spectrum (26 Jun–16 Aug 2024, excluding 22–30 Jul 2024) at RF7, RF5, and RF3, with the highest IG-band peak, a smaller secondary IG peak, and their difference frequency marked.

If such an interaction were to take place, this could at the same time explain the closely related transfer functions of IG and VLF. The strength of such an interaction scales with the amplitude of the interacting components (Elgar and Guza 1985). Since the IG amplitude increases with the offshore forcing, this could explain both the observed increase of $H_{s,VLF}$ with P_{Tm01} and the close covariation of the two bands. The IG waves on the reef flat are moreover free rather than bound long waves, which is what could allow them to exchange energy with other frequencies rather than only with the groups that forced them.

To test this hypothesis, a bispectral analysis could be performed to establish the phase coupling between the IG components involved and the VLF frequency (Elgar and Guza 1985). Such an interaction would also provide a second route towards resonance. Besides being forced directly from offshore, a resonant response could then develop when enough energy is transferred to a frequency close to the fundamental mode of the reef flat.

5.6. Shoreline run-up

Understanding the reef dynamics ultimately contributes to predicting run-up at the shoreline. Over the analysed window on 11 July, set-up was the largest contribution, while IG waves dominated the wave-induced contribution (Figure 4.21). This IG dominance is consistent with observations at other

reef-lined coasts, where shoreline run-up is similarly dominated by low-frequency motions (Péquignet et al. 2009; Beetham et al. 2016; Cheriton et al. 2016; Gawehn et al. 2016; Shimozono et al. 2022), and with the antinode identified at the shoreline in Section 5.3. This assessment was, however, limited to the short available run-up record.

The difference between the two exceedance levels matters for coastal flooding assessment. $R_{2\%}$ exceeded $\eta_{2\%}$ by $28\,\%$. Using $\eta_{2\%}$ to assess the shoreline run-up could therefore underestimate the water level reached at the coast, and studies that do so, such as Merrifield et al. (2014), may underpredict it for this type of reef-lined coast.

Climate change is relevant here as well, as sea levels are expected to rise, while more energetic events can lead to a higher set-up. Greater water depths over the reef can reduce wave dissipation and allow more wave energy to propagate towards the shoreline. In addition, increasing water depth shifts the reef-flat eigenfrequencies towards higher frequencies, changing their position relative to the forcing spectrum. Péquignet et al. (2009) therefore suggested that resonance over reef flats may become more important under sea-level rise.

6

Conclusions and recommendations

The objective of this study was to identify the processes and forcing conditions that govern the magnitude and transformation of infragravity (IG) and very-low-frequency (VLF) waves over a fringing reef. To this end, an observational dataset collected over approximately three months between June and September 2024 was analysed.

The main research question addressed in this study is as follows:

What processes and conditions influence the magnitude of infragravity (IG) and very-low-frequency (VLF) waves over a fringing reef?

In order to answer this question, four sub-questions were addressed, which are answered separately below.

Sub-question 1

How do offshore wave conditions and local water depth influence IG and VLF wave heights across the reef flat?

IG and VLF wave heights over the reef flat are found to depend most strongly on the offshore gravity wave (GW) power, which combines the offshore GW height and period. In addition, they are modulated to a lesser extent by the water level over the reef, which depends on the tide and the set-up.

Sub-question 2

How do gravity (GW), infragravity (IG), and very-low-frequency (VLF) wave properties evolve in the cross-shore and longshore directions?

The La Saline fringing reef was found to act as a strong low-pass filter. Mean $H_{s,GW}$ decreased by $97.6\,\%$ between the reef slope and the mid-reef. At the mid-reef, the IG and VLF bands dominated, accounting for $59\,\%$ and $30.7\,\%$ of the total energy, respectively.

Both $H_{s,IG}$ and $H_{s,VLF}$ peaked at the reef crest and decreased towards the mid-reef. For VLF, however, this pattern depended on the forcing, with stronger forcing sometimes resulting in an increase towards the mid-reef. At the mid-reef, $H_{s,IG}$ remained comparable to its offshore value, while $H_{s,VLF}$ was amplified by approximately $235\,\%$. Closer to the shoreline, $H_{s,IG}$ increased again on 11 July.

No significant longshore variability in wave height or period was found beyond that associated with local bathymetric variations.

Up to the mid-reef, GW, IG, and VLF motions were mainly cross-shore directed. Near the shoreline, GW and IG remained mainly cross-shore directed, whereas the VLF motion became almost entirely longshore-directed.

The shoreward dominance of the LF bands was also reflected in the run-up. Over the analysed window on 11 July, the wave set-up, IG, VLF, and GW components accounted for $65.9\,\%$, $28.6\,\%$, $2.2\,\%$, and

$3.3\,\%$ of the total run-up magnitude, respectively. IG therefore formed the dominant contribution within the oscillatory part of the run-up.

Sub-question 3

Do standing wave patterns occur on the reef flat, and if so, what is their spatial signature?

Standing-wave patterns were found to be present on the reef flat. On 11 July, full reflection was observed near the shoreline for both IG and VLF waves, forming an antinode there. Towards the reef crest, the outgoing component became smaller relative to the incoming component for both bands. This indicates that the wave field was close to fully standing near the shoreline and became more progressive in character moving offshore.

Sub-question 4

What physical mechanisms drive the generation and amplification of VLF waves on the reef flat?

Indications of a resonant response following an open-ended basin configuration were found. However, VLF energy was also present at times when no resonance signature was observed, which suggests that resonance is not the only mechanism involved. Non-linear interactions between IG components could, for example, be explored further as a VLF generation mechanism.

Recommendations

Based on the findings and limitations of this study, the following recommendations are made for future research:

- Deploy the ADVs with longer burst durations of at least $1\,\mathrm{h}$, and preferably longer, to improve the reliability of velocity-based analyses, particularly for the VLF band.
- Deploy pressure and velocity sensors closer to the shoreline and in the longshore direction to further investigate the nature of the longshore-directed VLF motions observed near the shoreline.
- Establish the VLF frequency limits on a stronger physical basis. In particular, the lower frequency limit should be further investigated to better separate VLF surface-wave motions from slower variations in tidal level and wave set-up.
- Extend the run-up measurements to longer periods and a wider range of forcing conditions. This would allow transfer functions to be established directly for shoreline run-up and would make it possible to investigate whether resonant VLF conditions are associated with enhanced run-up.
- Extend the observational analysis with numerical modelling. This could be used to test hypotheses on the proposed VLF generation and amplification mechanisms under controlled variations in reef geometry, water level, and offshore forcing, and to extend the analysis beyond the conditions captured during the field campaign.
- Include the effect of bottom roughness more explicitly when investigating resonance. Quantifying the associated damping could help determine whether it contributes to the shift of the maximum VLF response towards frequencies below the theoretical fundamental frequency.
- Perform bispectral analysis to investigate non-linear interactions between low-frequency components and their possible contribution to VLF generation.

References

Battjes, J. A., H. J. Bakkenes, T. T. Janssen, and A. R. Van Dongeren (2004). “Shoaling of subharmonic gravity waves”. In: *Journal of Geophysical Research: Oceans* 109.C2, p. C02009. DOI: 10.1029/2003JC001863.

Becker, J. M., M. A. Merrifield, and H. Yoon (2016). “Infragravity waves on fringing reefs in the tropical Pacific: Dynamic setup”. In: *Journal of Geophysical Research: Oceans* 121.5, pp. 3010–3028. DOI: 10.1002/2015JC011516.

Becker, Janet M., Mark A. Merrifield, and Matthew Ford (2014). “Water level effects on breaking wave setup for Pacific Island fringing reefs”. In: *Journal of Geophysical Research: Oceans* 119.2, pp. 914–932. DOI: 10.1002/2013JC009373.

Beetham, Edward, Paul S. Kench, Joanne O’Callaghan, and Stéphane Popinet (2016). “Wave transformation and shoreline water level on Funafuti Atoll, Tuvalu”. In: *Journal of Geophysical Research: Oceans* 121.1, pp. 311–326. DOI: 10.1002/2015JC011246.

Belkadi, Myriam, Frederic Bouchette, France Floc’h, Marion Tissier, and Damien Sous (2024). “Characterization of Very Low Frequency Wave Energy Distribution in a Coral Reef–Lagoon System”. In: *CoastLab 2024: Physical Modelling in Coastal Engineering and Science*. Delft, Netherlands: TU Delft OPEN Publishing. URL: https://proceedings.open.tudelft.nl/coastlab24/article/view/804.

Bertin, Xavier, A. T. M. de Bakker, Ap van Dongeren, Giovanni Coco, Gwenaël André, Fabrice Ardhuin, Philippe Bonneton, Frédéric Bouchette, Bruno Castelle, Wayne C. Crawford, Mark Davidson, Michiel Deen, Thomas Guérin, Katie Inch, Fabien Leckler, Robert McCall, H. Muller, Maitane Olabarrieta, and Marion Tissier (2018). “Infragravity waves: From driving mechanisms to impacts”. In: *Earth-Science Reviews* 177, pp. 774–799. DOI: 10.1016/j.earscirev.2018.01.002. URL: https://doi.org/10.1016/j.earscirev.2018.01.002.

Bishop, C. T. and M. A. Donelan (1987). “Measuring Waves with Pressure Transducers”. In: *Coastal Engineering* 11, pp. 309–328. DOI: 10.1016/0378-3839(87)90031-7.

Bosboom and Stive (Jan. 11, 2023). *Coastal Dynamics*. Delft, The Netherlands: TU Delft Open, pp. 270–271. ISBN: 978-94-6366-370-0. DOI: 10.5074/T.2021.001. URL: https://doi.org/10.5074/T.2021.001.

Bowen, A. J. and R. A. Holman (1989). “Shear instabilities of the mean longshore current 1. Theory”. In: *Journal of Geophysical Research* 94, pp. 18023–18030.

Bruch, William, Emmanuel Cordier, France Floc’h, and Stuart G. Pearson (2022). “Water Level Modulation of Wave Transformation, Setup and Runup Over La Saline Fringing Reef”. In: *Journal of Geophysical Research: Oceans* 127.e2022JC018570. DOI: https://doi.org/10.1029/2022JC018570.

Buckley, M. L., R. J. Lowe, J. E. Hansen, A. R. van Dongeren, and C. D. Storlazzi (2018). “Mechanisms of wave-driven water level variability on reef-fringed coastlines”. In: *Journal of Geophysical Research: Oceans* 123.5, pp. 3811–3831. DOI: 10.1029/2018JC013933. URL: https://doi.org/10.1029/2018JC013933.

Chanson, Hubert (Aug. 2008). “Acoustic Doppler Velocimetry (ADV) in the Field and in Laboratory: Practical Experiences”. In: *Proceedings of the International Meeting on Measurements and Hydraulics of Sewers (IMMHS’08), Summer School GEMCEA/LCPC*. Hydraulic Model Report No. CH70/08, Division of Civil Engineering, The University of Queensland, Brisbane, Australia. Bouguenais, France, pp. 49–66.

Cheriton, Olivia M., Curt D. Storlazzi, and Kurt J. Rosenberger (2016). “Observations of wave transformation over a fringing coral reef and the importance of low-frequency waves and offshore water levels to runup, overwash, and coastal flooding”. In: *Journal of Geophysical Research: Oceans* 121.5, pp. 3121–3140. DOI: 10.1002/2015JC011231.

Contardo, Stephanie, Ryan J. Lowe, Francois Dufois, Jeff E. Hansen, and Graham Symonds (2025). "Free Long Wave Generation: Breakpoint Forcing Versus Bound Wave Release". In: *Journal of Geophysical Research: Oceans* 130.7, e2025JC022377. DOI: 10.1029/2025JC022377.

Cordier, E., J. Lézé, and J. L. Join (2013). "Natural tidal processes modified by the existence of fringing reef on La Reunion Island (Western Indian Ocean): Impact on the relative sea level variations". In: *Continental Shelf Research* 55, pp. 119–128. DOI: 10.1016/j.csr.2013.01.016.

Davy, C., G. Barruol, F. Fontaine, and E. Cordier (2016). "Analyses of extreme swell events on La Réunion Island from microseismic noise". In: *Geophysical Journal International* 207.3, pp. 1767–1782. DOI: 10.1093/gji/ggw365.

Dongeren, Ap van, Martijn de Jong, Cock van der Lem, Alex van Deyzen, and Joost den Bieman (2016). "Review of Long Wave Dynamics over Reefs and into Ports with Implication for Port Operations". In: *Journal of Marine Science and Engineering* 4.1. DOI: https://doi.org/10.3390/jmse4010012.

Elgar, Steve and R. T. Guza (1985). "Observations of bispectra of shoaling surface gravity waves". In: *Journal of Fluid Mechanics* 161, pp. 425–448. DOI: 10.1017/S0022112085003007.

Emery, W. J. and R. E. Thomson (2014). *Data Analysis Methods in Physical Oceanography*. Amsterdam: Elsevier.

Ferrario, Filippo, Michael W. Beck, Curt D. Storlazzi, Fiorenza Micheli, Christine C. Shepard, and Laura Airoldi (2014). "The effectiveness of coral reefs for coastal hazard risk reduction and adaptation". In: *Nature Communications* 5, p. 3794. DOI: 10.1038/ncomms4794. URL: https://doi.org/10.1038/ncomms4794.

Gawehn, M., A. R. van Dongeren, A. van Rooijen, C. D. Storlazzi, O. M. Cheriton, and A. Reniers (2016). "Identification and classification of very low frequency waves on a coral reef flat". In: *Journal of Geophysical Research: Oceans* 121.10, pp. 7560–7574. DOI: 10.1002/2016JC011834.

Goring, Derek and Vladimir Nikora (Jan. 2002). "Despiking Acoustic Doppler Velocimeter Data". In: *Journal of Hydraulic Engineering-asce - J HYDRAUL ENG-ASCE* 128. DOI: 10.1061/(ASCE)0733-9429(2002)128:1(117).

Guza, R. T., E. B. Thornton, and R. A. Holman (1984). "Swash on steep and shallow beaches". In: *Proceedings of the 19th International Conference on Coastal Engineering*. ASCE, pp. 708–723. DOI: 10.9753/icce.v19.48.

Heinrich, Stephen M. and Isabelle Dufour (2015). "Fundamental Theory of Resonant MEMS Devices". In: *Resonant MEMS: Fundamentals, Implementation and Application*. Ed. by Oliver Brand, Isabelle Dufour, Stephen M. Heinrich, and Fabien Josse. Wiley-VCH Verlag GmbH & Co. KGaA, pp. 3–28. DOI: 10.1002/9783527676330.ch1.

Hench, James L. and Johanna H. Rosman (2013). "Observations of spatial flow patterns at the coral colony scale on a shallow reef flat". In: *Journal of Geophysical Research: Oceans* 118.3, pp. 1142–1156. DOI: 10.1002/jgrc.20105.

Henderson, Stephen M., Steve Elgar, and A. J. Bowen (2001). "Observations of surf beat propagation and energetics". In: *Proceedings of the 27th International Conference on Coastal Engineering*. Sydney, Australia: ASCE.

Herbers, T. H. C., S. Elgar, R. T. Guza, and W. C. O'Reilly (1995). "Infragravity□Frequency (0.005–0.05 Hz) Motions on the Shelf. Part II: Free Waves". In: *Journal of Physical Oceanography* 25.6, pp. 1063–1079. DOI: 10.1175/1520-0485(1995)025<1063:IFHMOT>2.0.CO;2. URL: https://doi.org/10.1175/1520-0485(1995)025%3C1063:IFHMOT%3E2.0.CO;2.

Herbers, T. H. C., Steve Elgar, and R. T. Guza (1999). "Directional spreading of waves in the nearshore". In: *Journal of Geophysical Research* 104.C4, pp. 7683–7693. DOI: 10.1029/1998JC900092.

Holthuijsen, Leo H. (2007). *Waves in Oceanic and Coastal Waters*. Cambridge: Cambridge University Press. ISBN: 9780521860284. DOI: 10.1017/CBO9780511618536.

IPCC (2021). *Climate Change 2021: The Physical Science Basis. Contribution of Working Group I to the Sixth Assessment Report of the Intergovernmental Panel on Climate Change*. Ed. by V. Masson-Delmotte, P. Zhai, A. Pirani, S. L. Connors, C. Péan, S. Berger, N. Caud, Y. Chen, L. Goldfarb, M. I. Gomis, M. Huang, K. Leitzell, E. Lonnoy, J. B. R. Matthews, T. K. Maycock, T. Waterfield, O. Yelekçi, R. Yu, and B. Zhou. Cambridge, United Kingdom and New York, NY, USA: Cambridge University Press, p. 2391. DOI: 10.1017/9781009157896.

Jaud, Marion, Mila Geindre, Stéphane Bertin, Yoan Benoit, Emmanuel Cordier, France Floc'h, Emmanuel Augereau, and Kévin Martins (2025). "Correction of Refraction Effects on Unmanned Aerial

Vehicle Structure-from-Motion Bathymetric Survey for Coral Reef Roughness Characterisation". In: *Remote Sensing* 17.23, p. 3846. DOI: 10.3390/rs17233846.

Kench, Paul S. (2025). "Effects of Environmental and Climatic Changes on Coral Reef Islands". In: *Annual Review of Marine Science*. DOI: https://doi.org/10.1146/annurev-marine-032223-030921.

Kennedy, David M. and Colin D. Woodroffe (2002). "Fringing reef growth and morphology: A review". In: *Earth□Science Reviews*. DOI: https://doi.org/10.1016/S0012-8252(01)00077-0.

Lasserre, Camila Gaido, Marion Tissier, Ad Reniers, Stuart Pearson, and Jeremy Bricker (2020). "Numerical experiments on resonant wave amplification over a fringing reef". In: *Proceedings of Virtual Conference on Coastal Engineering, 2020*. Ed. by Patrick Lynett. Vol. 36v. Coastal Engineering Research Council. DOI: 10.9753/icce.v36v.waves.54.

Lippmann, T. C., T. H. C. Herbers, and E. B. Thornton (1999). "Gravity and Shear Wave Contributions to Nearshore Infragravity Motions". In: *Journal of Physical Oceanography* 29.2, pp. 231–239. DOI: 10.1175/1520-0485(1999)029<0231:GASWCT>2.0.CO;2.

Longuet-Higgins, M. S. and R. W. Stewart (1962). "Radiation stress and mass transport in gravity waves, with application to "surf beats"". In: *Journal of Fluid Mechanics* 13, pp. 481–504.

Lowe (Mar. 2021). *Advancing Predictions of Nearshore Processes Within Ecosystems*. Presentation for the 2nd Sea State CCI User Meeting. European Space Agency Climate Change Initiative.

Lowe, James L. Falter, Jeffrey R. Koseff, Stephen G. Monismith, and Marlin J. Atkinson (2007). "Spectral wave flow attenuation within submerged canopies: Implications for wave energy dissipation". In: *Journal of Geophysical Research: Oceans* 112.C5, p. C05018. DOI: 10.1029/2006JC003605.

Lowe, Ryan J., James L. Falter, Stephen G. Monismith, and Michael J. Atkinson (2009). "Wave-driven circulation of a coastal reef–lagoon system". In: *Journal of Physical Oceanography* 39.4, pp. 873–893. DOI: 10.1175/2008JPO3958.1.

Merrifield, Mark A., Janet M. Becker, Matthew Ford, and Yuepeng Yao (2014). "Observations and estimates of wave-driven water level extremes at the Marshall Islands". In: *Geophysical Research Letters* 41.20, pp. 7245–7253. DOI: 10.1002/2014GL061005.

Mouquet, Pascal, Touria Bajjouk, and Michel Ropert (2016). *MNT Bathymétrique à haute résolution des fonds marins des zones récifales de la côte ouest de l'île de La Réunion (2015)*. DOI: 10.12770/ee059de2-2c81-46ce-88de-0fb5517046af.

National Oceanic and Atmospheric Administration (NOAA) (2024). *What are the three main types of coral reefs?* https://oceanservice.noaa.gov/facts/threecorals.html. Accessed: 2025-01-12.

Nikora, Vladimir I. and Derek G. Goring (1998). "ADV Measurements of Turbulence: Can We Improve Their Interpretation?" In: *Journal of Hydraulic Engineering* 124.6, pp. 630–634. DOI: 10.1061/(ASCE)0733-9429(1998)124:6(630).

Noyes, T. James, R. T. Guza, Steve Elgar, and T. H. C. Herbers (2002). "Comparison of Methods for Estimating Nearshore Shear Wave Variance". In: *Journal of Atmospheric and Oceanic Technology* 19, pp. 136–149.

Oltman-Shay, Joan, Peter A. Howd, and William A. Birkemeier (1989). "Shear Instabilities of the Mean Longshore Current: 2. Field Observations". In: *Journal of Geophysical Research: Oceans* 94.C12, pp. 18031–18042. DOI: 10.1029/JC094iC12P18031.

Otnes, Robert K. and Loren D. Enochson (1978). *Applied Time Series Analysis, Volume 1: Basic Techniques*. New York: John Wiley and Sons. ISBN: 9780471242352.

Pearson, Stuart G., Curt D. Storlazzi, Ap van Dongeren, Marion F. S. Tissier, and Ad J. H. M. Reniers (2017). "A Bayesian-Based System to Assess Wave-Driven Flooding Hazards on Coral Reef-Lined Coasts". In: *Journal of Geophysical Research: Oceans* 122.12. DOI: 10.1002/2017JC013204.

Péquignet, A. Christine N., Janet M. Becker, Mark A. Merrifield, and Jérôme Aucan (2009). "Forcing of resonant modes on a fringing reef during tropical storm Man-Yi". In: *Geophysical Research Letters* 36.3, p. L03607. DOI: 10.1029/2008GL036259.

Péquignet, Anne C. N., Janet M. Becker, and Mark A. Merrifield (2014). "Energy transfer between wind waves and low-frequency oscillations on a fringing reef, Ipan, Guam". In: *Journal of Geophysical Research: Oceans* 119, pp. 6709–6724. DOI: 10.1002/2014JC010179.

Pomeroy, Andrew, Ryan Lowe, Graham Symonds, A. P. Van Dongeren, and Christine Moore (2012a). "The dynamics of infragravity wave transformation over a fringing reef". In: *Journal of Geophysical Research C: Oceans* 117, p. C11022. DOI: 10.1029/2012JC008310. URL: https://doi.org/10.1029/2012JC008310.

Pomeroy, A. van Dongeren, R. J. Lowe, J. S. M. van Thiel de Vries, and J. A. Roelvink (2012b). “Low frequency wave resonance in fringing reef environments”. In: 1, pp. 1–10. DOI: 10.9753/icce.v33.currents.25.

Rabinovich, A. B. (2009). “Seiches and Harbor Oscillations”. In: *Handbook of Coastal and Ocean Engineering*. Ed. by Y. C. Kim. Singapore: World Scientific Publishing Co. Pte. Ltd., pp. 193–236.

Rao, Singiresu S. (2011). *Mechanical Vibrations*. 5th ed. Upper Saddle River, NJ: Prentice Hall.

Rodríguez, G., C. Guedes Soares, and U. Machado (1999). “Uncertainty of the sea state parameters resulting from the methods of spectral estimation”. In: *Ocean Engineering* 26.10, pp. 991–1002. DOI: 10.1016/S0029-8018(98)00027-4.

Roelvink, J. A. and M. J. F. Stive (1989). “Bar-Generating Cross-Shore Flow Mechanisms on a Beach”. In: *Journal of Geophysical Research* 94.C4, pp. 4785–4800. DOI: 10.1029/JC094iC04p04785.

Sabatier, François (2007). “U.S. Army Corps of Engineers, Coastal Engineering Manual (CEM), Engineer Manual 1110-2-1100 [Compte rendu d’ouvrage]”. In: *Méditerranée. Revue géographique des pays méditerranéens / Journal of Mediterranean geography* 108, p. 146. DOI: 10.4000/mediterranee.201.

Sheremet, A., R. T. Guza, S. Elgar, and T. H. C. Herbers (2002). “Observations of nearshore infragravity waves: Seaward and shoreward propagating components”. In: *Journal of Geophysical Research: Oceans* 107.C8, p. 3095. DOI: 10.1029/2001JC000970. URL: https://doi.org/10.1029/2001JC000970.

Shimozono, Takenori, Ryotaro Shibata, Susumu Onaka, Tomohiro Mori, and Yuta Awazu (2022). “Variability of shoreline water levels on an atoll in the Maldives”. In: *Journal of Geophysical Research: Oceans* 127.5, e2021JC017880. DOI: 10.1029/2021JC017880.

Stockdon, H. F., R. A. Holman, P. A. Howd, and A. H. Sallenger (2006). “Empirical Parameterization of Setup, Swash, and Runup”. In: *Coastal Engineering* 53.7, pp. 573–588. DOI: 10.1016/j.coastaleng.2005.12.005. URL: https://www.sciencedirect.com/science/article/pii/S0378383906000044.

Su, Shih-Feng and Gangfeng Ma (2018). “Modeling two-dimensional infragravity motions on a fringing reef”. In: *Ocean Engineering* 153, pp. 256–267. DOI: 10.1016/j.oceaneng.2018.01.111.

Suhayda, Joseph N. (1974). “Standing waves on beaches”. In: *Journal of Geophysical Research* 79.21, pp. 3065–3071. DOI: 10.1029/JC079i021p03065. URL: https://doi.org/10.1029/JC079i021p03065.

Symonds, G., D. A. Huntley, and A. J. Bowen (1982). “Two-dimensional surf beat: Long wave generation by a time-varying breakpoint”. In: *Journal of Geophysical Research: Oceans* 87.C1, pp. 492–498. DOI: 10.1029/JC087iC01p00492. URL: https://doi.org/10.1029/JC087iC01p00492.

Tissier, Marion F. S., Patrick Bonneton, Hervé Michallet, and Gerben G. Ruessink (2015). “Infragravity-wave modulation of short-wave celerity in the surf zone”. In: *Journal of Geophysical Research: Oceans* 120.10, pp. 6799–6814. DOI: 10.1002/2015JC010708.

Ursell, F. (1952). “Edge waves on a sloping beach”. In: *Proceedings of the Royal Society of London. Series A* 214.1116, pp. 79–97. DOI: 10.1098/rspa.1952.0152. URL: https://doi.org/10.1098/rspa.1952.0152.

Vetter, O., J. M. Becker, M. A. Merrifield, A.–C. Pequignet, J. Aucan, S. J. Boc, and C. E. Pollock (2010). “Wave setup over a Pacific Island fringing reef”. In: *Journal of Geophysical Research: Oceans* 115.C12, p. C12066. DOI: 10.1029/2010JC006455.

Watanabe, Atsushi and Takashi Nakamura (2019). “Carbon Dynamics in Coral Reefs”. In: *Blue Carbon in Shallow Coastal Ecosystems: Carbon Dynamics, Policy, and Implementation*. Ed. by Tomoyuki Kuwae and Motohiko Hori. Springer Nature Singapore, pp. 273–293. DOI: 10.1007/978-981-13-1295-3_10.

Winter, G., R. J. Lowe, G. Symonds, J. E. Hansen, and A. R. van Dongeren (2017). “Standing infragravity waves over an alongshore irregular rocky bathymetry”. In: *Journal of Geophysical Research: Oceans* 122.6, pp. 4868–4885. DOI: 10.1002/2016JC012242. URL: https://doi.org/10.1002/2016JC012242.

A Sensor metadata

This appendix lists the deployment details of the instruments used in this study. Table A.1 gives the pressure sensors and Table A.2 the ADV current meters.

Table A.1: Deployment period, sampling frequency, instrument type, location, and elevation above the bed for each pressure sensor. All deployments took place in 2024.

Sensor	Instrument type	Location (lat, lon)	Deployment period	Sampling frequency (Hz)	Height above the bed (m)
RS2	RBR Virtuoso	21.100641°S, 55.232360°E	04 Jun – 17 Sep	2	0.05
RF7	RBR Duet	21.099337°S, 55.233985°E	26 Jun – 16 Aug*	4	0.10
RF5	RBR Virtuoso	21.098871°S, 55.234344°E	07 Jun – 06 Sep	2	0.09
RF4	OSSI wave gauge	21.098346°S, 55.234836°E	07 Jun – 06 Sep	5	0.10
RF3	OSSI wave gauge	21.097853°S, 55.235239°E	07 Jun – 20 Aug	5	0.12
RF1	OSSI wave gauge	21.097472°S, 55.235358°E	07 Jun – 06 Sep	5	0.08
RF3a	RBR Virtuoso	21.094228°S, 55.231058°E	22 Jun – 03 Sep	2	0.10
RF3b	OSSI wave gauge	21.091247°S, 55.228321°E	22 Jun – 03 Sep	5	0.10

* Data gap from 22 Jul to 30 Jul

Table A.2: Deployment details for the Nortek ADV current meters. All deployments took place in 2024. Bed refers to the frame location, used as the sensor's analysis position. Head and bottom coordinates of the ADVs were surveyed separately and were used to determine instrument orientation. Note that the vertical coordinates are expressed as ellipsoidal heights (geodetic heights), rather than as levelled heights relative to the local vertical datum of RGR92. They are presented this way as they were surveyed as such, which avoids a conversion bias when using them directly in the projection of the velocity components.

ADV	Point	Coordinates (lat, lon)	Elevation (m)	Deployment period	Sampling frequency (Hz)	Height above the bed (m)
ADV1	Bed	21.097863°S, 55.235253°E	3.182	22 Jun – 04 Aug	8	0.25
	Head	21.097862°S, 55.235253°E	3.436			
	Bottom	21.097856°S, 55.235250°E	3.498			
ADV3	Bed	21.099161°S, 55.234228°E	3.285	22 Jun – 04 Aug	8	0.25
	Head	21.099161°S, 55.234228°E	3.517			
	Bottom	21.099155°S, 55.234223°E	3.544			
ADV-lidar	Bed	21.096066°S, 55.236107°E	2.896	11 Jul	32	0.30
	Head	21.096066°S, 55.236106°E	3.252			
	Bottom	21.096062°S, 55.236101°E	3.264			

B Pre-processing examples

This appendix shows one example per data set of the pre-processing described in Section 3.2.1.

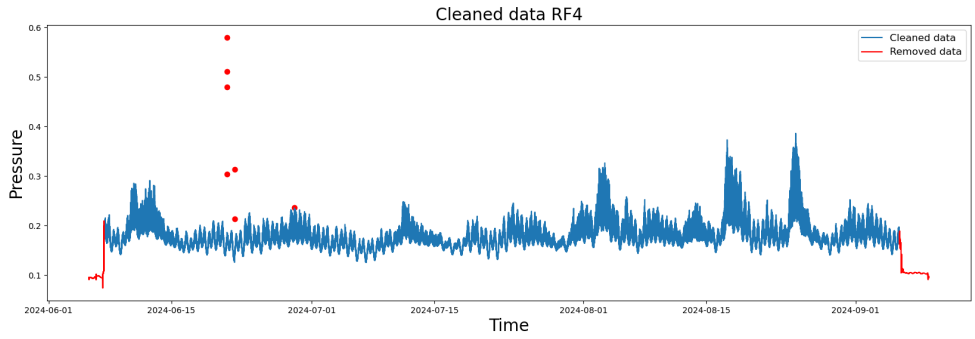


Figure B.1: Example of the pressure record cleaning procedure, shown for sensor RF4. Unphysical spikes, identified using a threshold of eight standard deviations of the hourly running mean, are shown alongside the resulting cleaned record.

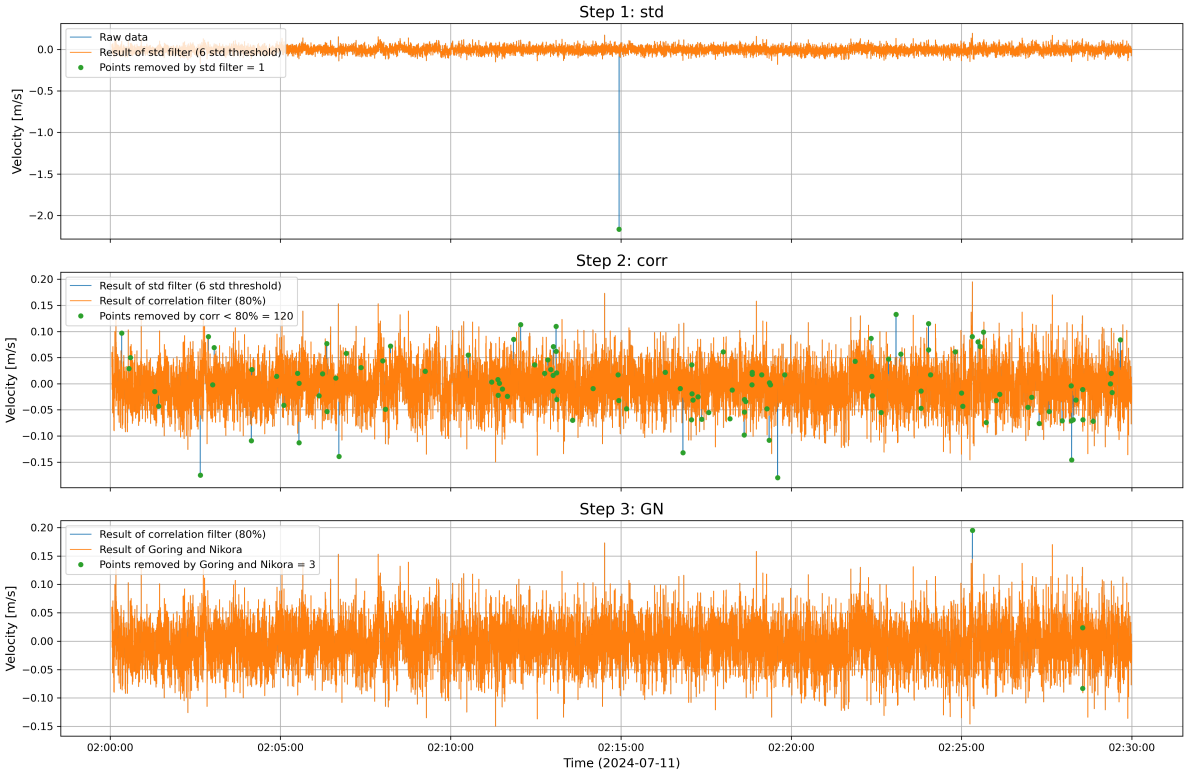


Figure B.2: Example of the ADV velocity pre-processing procedure. The raw signal is shown alongside the result after each successive filtering step: the running standard deviation filter, the correlation-based filter (correlation threshold of 80%), and the phase-space despiking method of Goring and Nikora (2002).

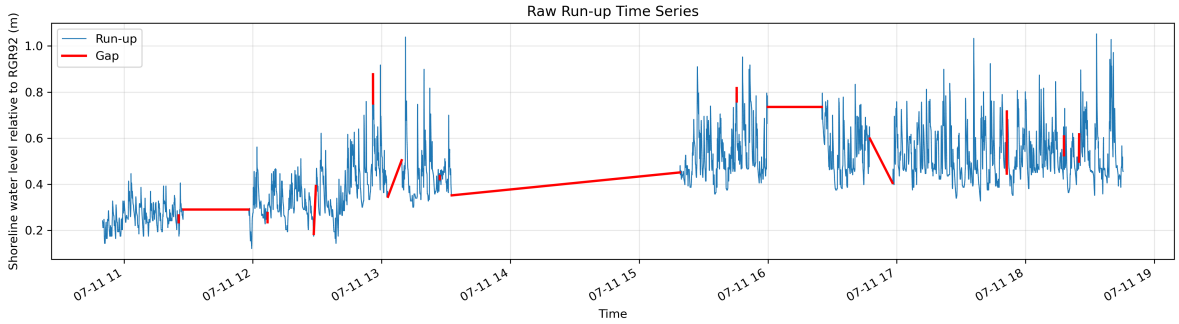


Figure B.3: Raw run-up signal marking the gaps in the data.

C Wave Set-up

The wave set-up at each reef-flat sensor was determined from the difference in water-surface elevation relative to the reef-slope station RS2, with both elevations expressed in the RGR92 reference system, as described in Section 3.2.4,

$$\bar{\eta}(\text{sensor}, t) = \left[z_{b,\text{sensor}} + h_{\text{sensor}}(t)\right] - \left[z_{b,\text{RS2}} + h_{\text{RS2}}(t)\right], \tag{C.1}$$

where z_b is the GNSS-surveyed sensor elevation minus its height above the bed d_s, and h the measured water depth. The resulting set-up time series for all reef-flat sensors is shown in Figure C.1.

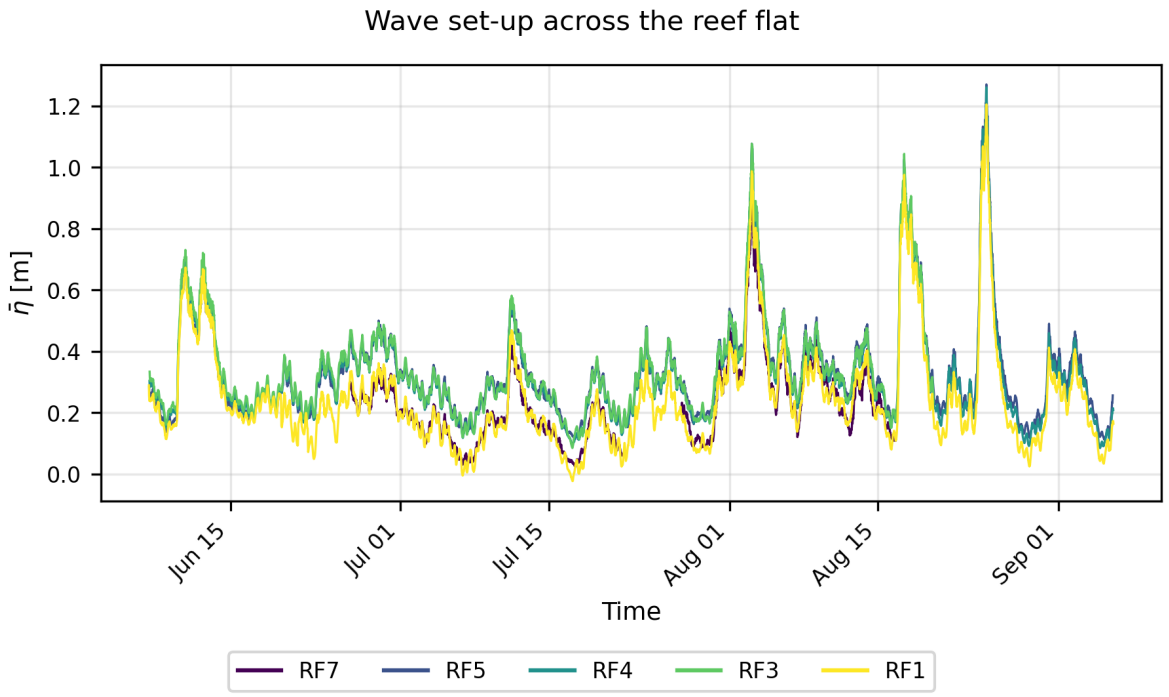


Figure C.1: Wave set-up $\bar{\eta}$ across the reef flat over the full study period, shown for all five reef-flat sensors (RF7, RF5, RF4, RF3, RF1) relative to the SWL at RS2.

The elevation of RS2 was not surveyed directly but obtained from its nominal deployment depth. It was therefore checked against the regression approach of Vetter et al. (2010), also applied by Bruch et al. (2022), in which the water-depth difference between a reef-flat sensor and RS2 is regressed against the offshore root-mean-square wave height in the gravity band,

$$h_{\text{sensor}}(t) - h_{\text{RS2}}(t) = a\, H_{\text{rms,GW,RS2}}(t) + c \tag{C.2}$$

where the intercept c is the depth difference at zero wave forcing, so that $z_{b,\text{RS2}} = z_{b,\text{sensor}} + c$. Applying this to each reef-flat sensor over the full record gives the values in Table C.1. All five estimates lie within $0.11\,\text{m}$ of the adopted value.

Table C.1: Elevation of RS2 obtained from the regression against each reef-flat sensor, compared with the adopted value of $-11.67\,\mathrm{m}$.

Reference sensor	$z_{b,\mathrm{RS2}}$ [m]	Difference [m]	R^2
RF7	-11.76	-0.09	0.97
RF5	-11.69	-0.01	0.97
RF4	-11.70	-0.03	0.97
RF3	-11.69	-0.01	0.96
RF1	-11.78	-0.11	0.94

Over the full study period the mean set-up was $0.22\,\mathrm{m}$ at RF7, $0.33\,\mathrm{m}$ at RF5 and RF4, $0.34\,\mathrm{m}$ at RF3 and $0.25\,\mathrm{m}$ at RF1, with a spread between the five stations of $0.12\,\mathrm{m}$ on average. This spread does not change with the set-up level, so relative to the set-up it becomes smaller as the set-up grows, and the assumption of a spatially uniform set-up is best justified under energetic conditions.

Part of this spread can be explained by uncertainty in the sensor elevations. Table C.1 shows that the elevation obtained for RS2 varies by about $0.10\,\mathrm{m}$ depending on which reef-flat sensor is used as reference, which is of the same order as the spread in set-up.

D Run-up and Water Level Decomposition

This appendix shows the decomposition described in Section 3.2.9, applied to the video-derived run-up R (Figure D.1) and to the surface elevation η at the ADV-lidar (Figure D.2) on 11 July 2024. The shaded area in both figures marks the $1\,\mathrm{h}$ window (13h–14h) over which the $2\,\%$ exceedance levels reported in Section 4.4.3 were determined.

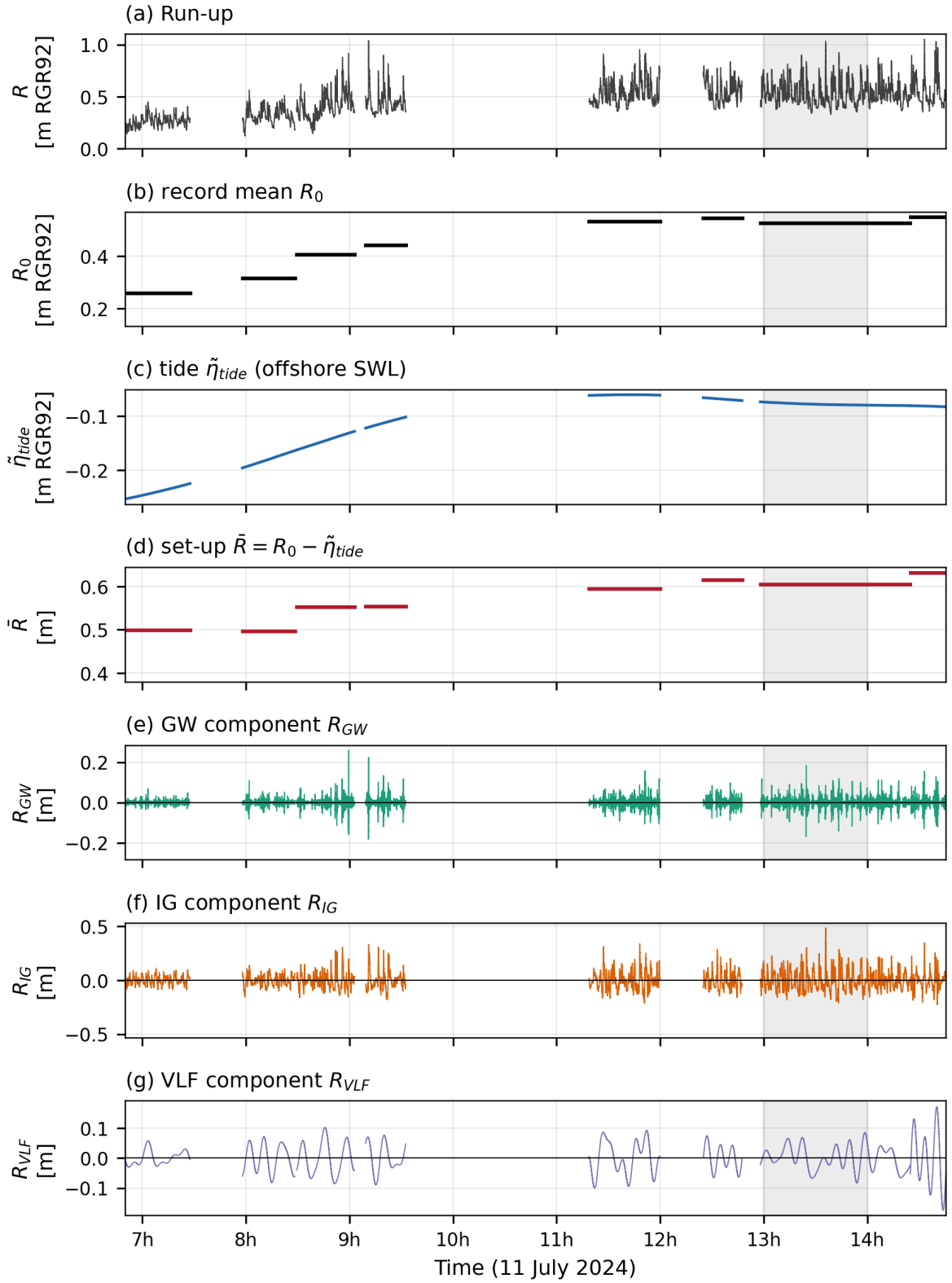


Figure D.1: Decomposition of the run-up R on 11 July 2024. (a) Run-up relative to the RGR92 datum. (b) Record mean R_0 per continuous segment. (c) Offshore still water level $\tilde{\eta}_{\text{tide}}$. (d) Set-up $\bar{R} = R_0 - \tilde{\eta}_{\text{tide}}$. (e–g) GW, IG, and VLF components obtained by band-pass filtering $R - R_0$. The shaded area marks the $1\,\text{h}$ window (13h–14h) used for the $2\,\%$ exceedance levels.

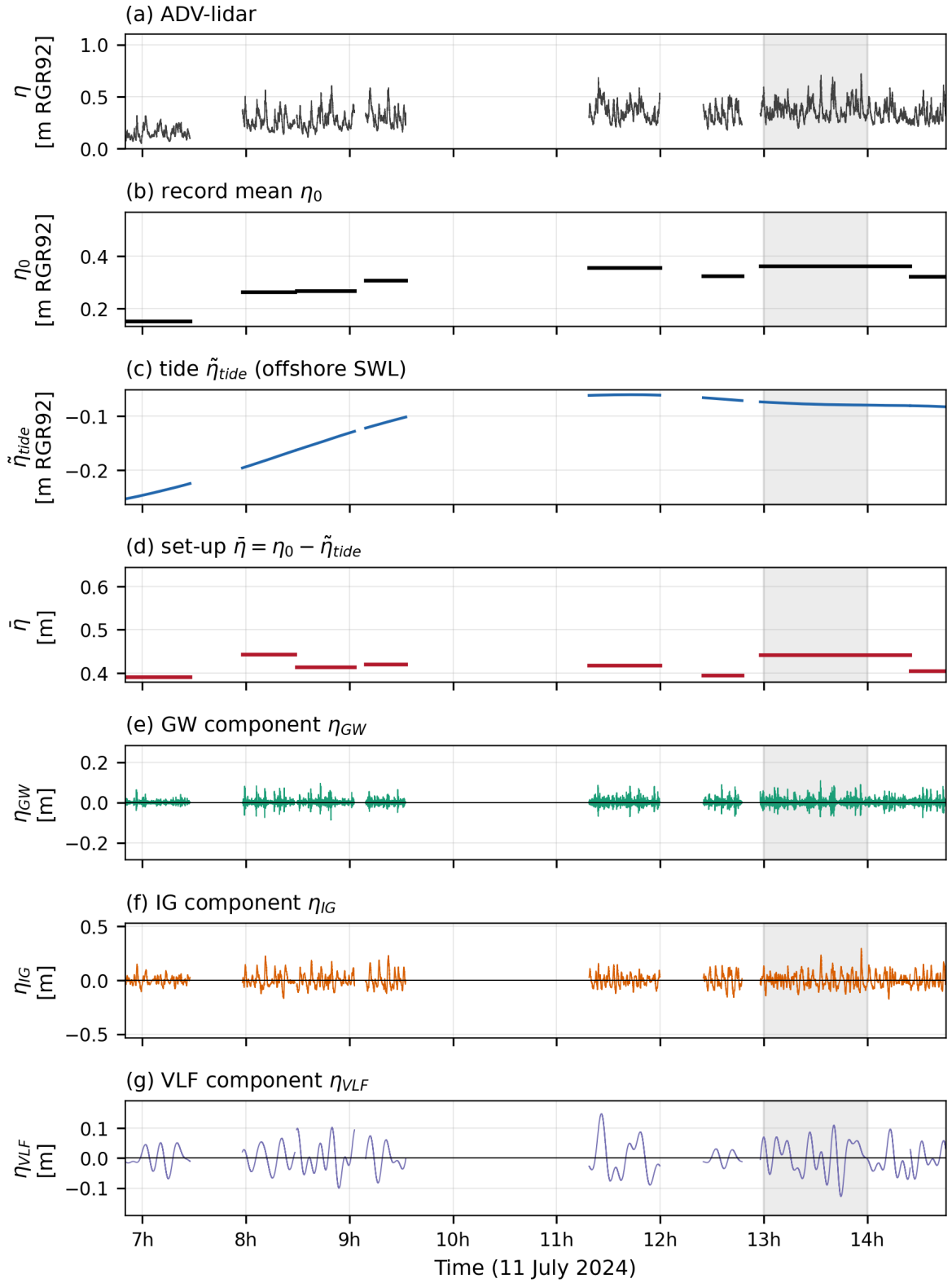


Figure D.2: Decomposition of the surface elevation η at the ADV-lidar over the same window as Figure D.1. (a) Surface elevation relative to the RGR92 datum. (b) Record mean η_0 per continuous segment. (c) Offshore still water level $\tilde{\eta}_{\text{tide}}$. (d) Set-up $\bar{\eta} = \eta_0 - \tilde{\eta}_{\text{tide}}$. (e–g) GW, IG, and VLF components obtained by band-pass filtering $\eta - \eta_0$. The shaded area marks the $1\,\text{h}$ window (13h–14h) used for the $2\,\%$ exceedance levels.

E Longshore hydrodynamic parameters

Figure E.1 shows the water depth and the significant wave heights in the GW, IG, and VLF bands at RF3 and the two longshore stations RF3a and RF3b, located at approximately the same cross-shore position, over the full study period. No systematic longshore variability attributable to physical processes is apparent; the small differences between the stations are consistent with their differing distance to the reef crest and the inhomogeneous bathymetry, as discussed in Section 4.3.

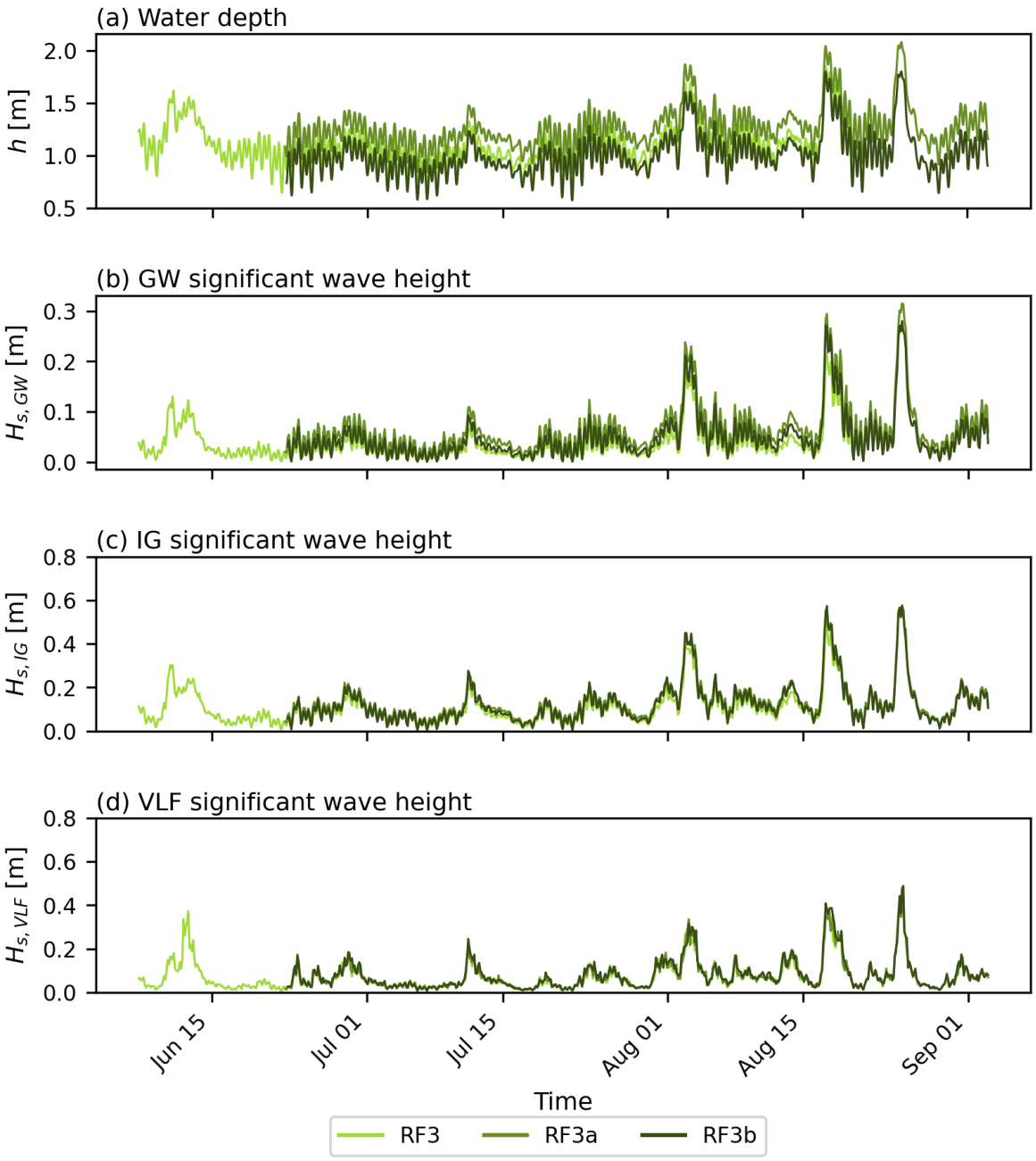


Figure E.1: Longshore hydrodynamic parameters at RF3, RF3a, and RF3b over the full study period: (a) water depth h, (b) $H_{s,GW}$, (c) $H_{s,IG}$, (d) $H_{s,VLF}$.

F Cross-shore spectral evolution

Figure F.1 shows the temporal evolution and mean energy density spectrum at the reef slope (RS2) and two reef flat stations (RF7, RF1), spanning the cross-shore transect from offshore to the mid reef. The distribution of energy across the GW, IG, and VLF bands derived from these spectra, and the cross-shore shift of the IG spectral peak, are described in Section 4.3.1.

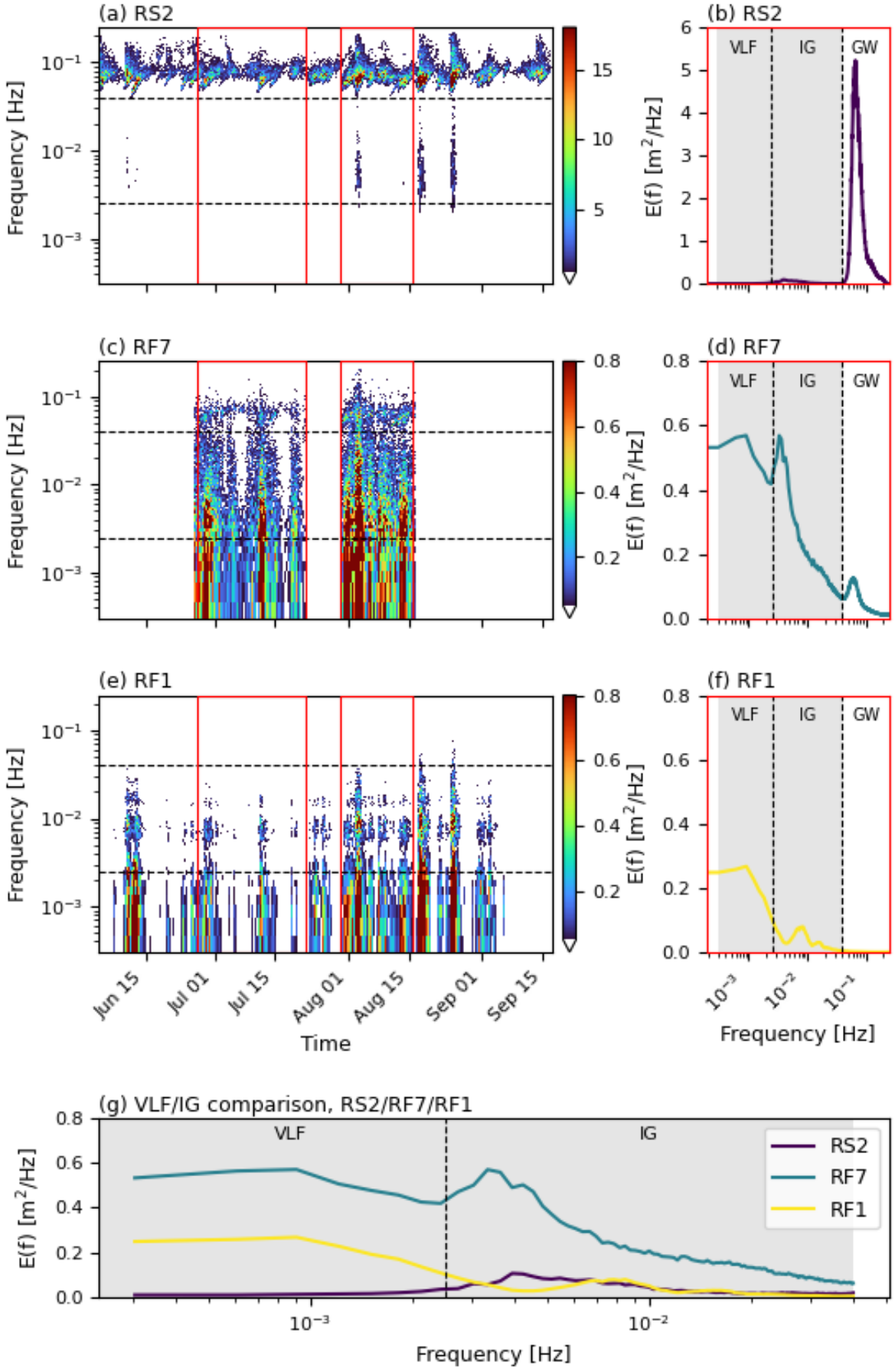


Figure F.1: (a, c, e) Temporal evolution and (b, d, f) mean energy density spectrum at RS2, RF7, and RF1. Red boxes mark the period used for the mean spectrum. (g) Mean energy density spectra of RS2, RF7, and RF1, zoomed to the VLF and IG bands, illustrating that at RS2 comparable IG energy is already present relative to RF1.

G IG resonance assessment

This appendix shows the resonance assessment for the IG band, following the enclosed-basin formulation described in Section 3.2.8.

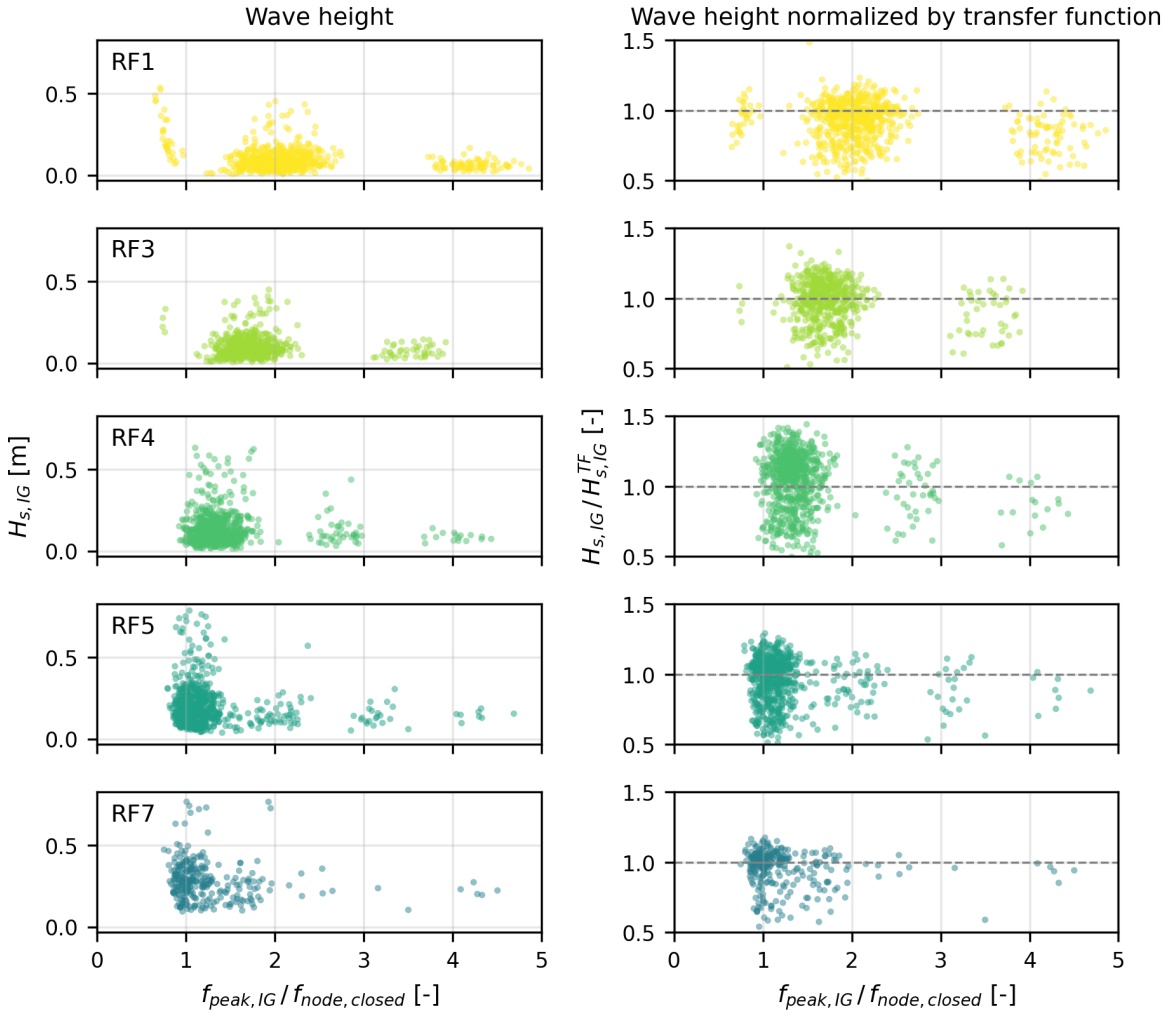


Figure G.1: $H_{s,IG}$ against the ratio of each sensor's own IG peak frequency to the closed-basin eigenfrequency, per reef-flat sensor. The left column shows the raw $H_{s,IG}$ and the right column shows $H_{s,IG}$ normalised by each sensor's own transfer-function prediction $H^{TF}_{s,IG}$.

H Additional spectra

This appendix gives the cross-shore VLF response for the two cases highlighted in Section 4.3.4 that are not shown there, namely 3 August 2024 01:30 and 11 July 2024 16:30. For each case the spectrum at every reef-flat sensor is shown, together with the band-integrated $H_{s,VLF}$ and the narrow-band H_{eq} around the RF1 peak frequency, in the same form as Figure 4.13.

On 3 August 2024 01:30 (Figure H.1), both peak frequencies lie further from the fundamental mode than on 2 August. The cross-shore structure of H_{eq} around the RF1 peak frequency nonetheless still grows toward the shoreline, which may indicate a resonance signature at that frequency.

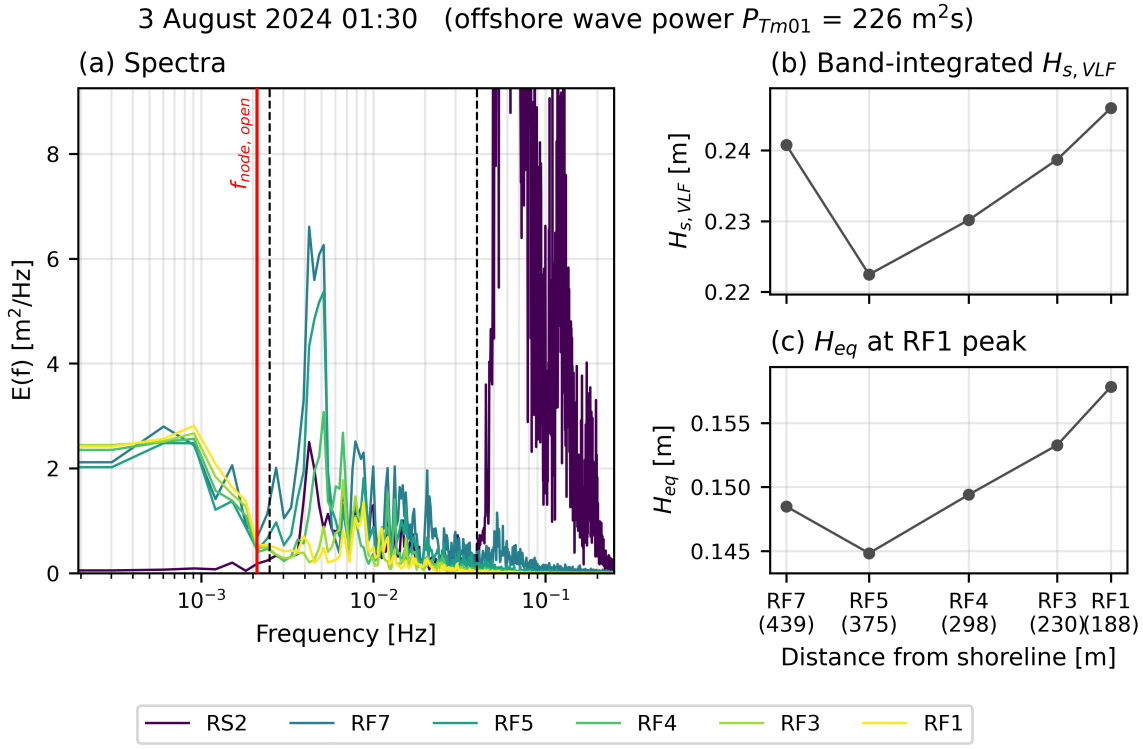


Figure H.1: Cross-shore VLF response on 3 August 2024 01:30. (a) shows the energy density spectrum at each reef-flat sensor, with the red line marking the open-ended basin eigenfrequency $f_{node,open} = 0.002\,11\,\mathrm{Hz}$ at that moment. (b) shows the band-integrated $H_{s,VLF}$ (top) and the narrow-band H_{eq} around the RF1 peak frequency (bottom) at each reef-flat sensor. The offshore peak at RS2 lies at $0.001\,52\,\mathrm{Hz}$ and the RF1 peak at $0.000\,91\,\mathrm{Hz}$, giving ratios to the fundamental of 0.72 and 0.43, respectively.

On 11 July 2024 16:30 (Figure H.2), there is no indication of a resonant response. The VLF energy at RF1 is lower than at the other sensors across the whole band, rather than showing the shoreward growth expected between a node at the reef crest and an antinode at the shoreline.

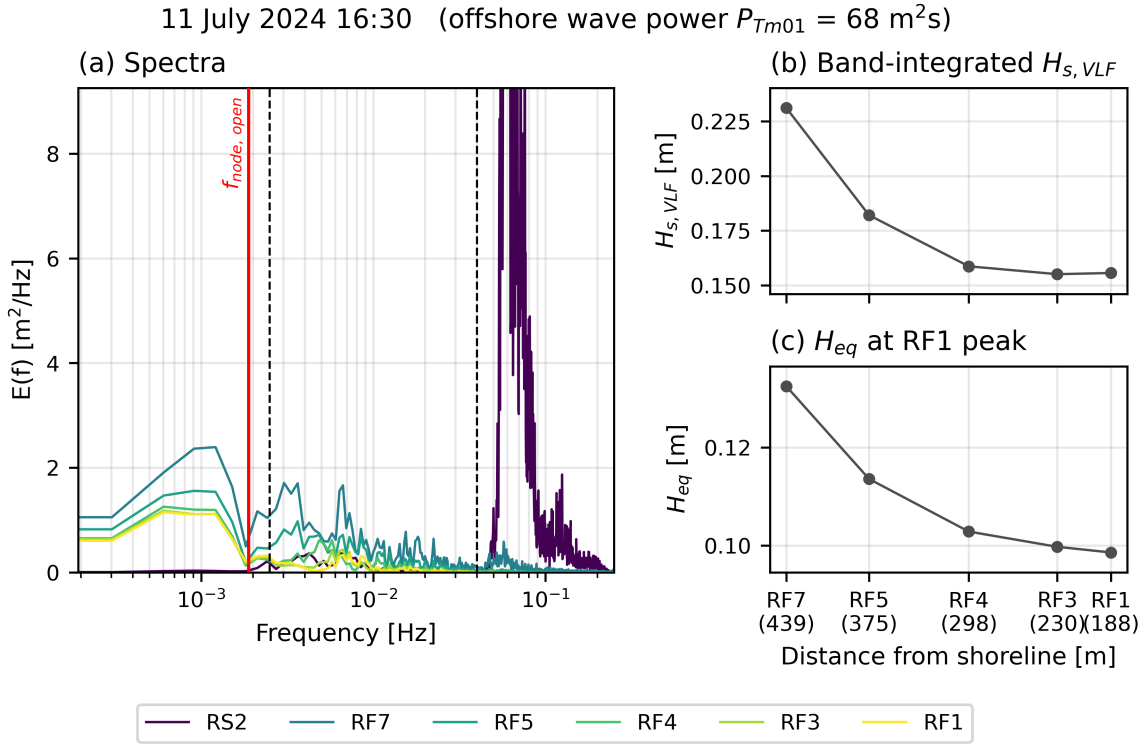


Figure H.2: Cross-shore VLF response on 11 July 2024 16:30. (a) shows the energy density spectrum at each reef-flat sensor, with the red line marking the open-ended basin eigenfrequency $f_{node,open} = 0.001\,89\,\mathrm{Hz}$ at that moment. (b) shows the band-integrated $H_{s,VLF}$ (top) and the narrow-band H_{eq} around the RF1 peak frequency (bottom) at each reef-flat sensor. The offshore peak at RS2 lies at $0.002\,42\,\mathrm{Hz}$ and the RF1 peak at $0.000\,61\,\mathrm{Hz}$, giving ratios to the fundamental of 1.28 and 0.32, respectively.

Standing wave analysis on 11 July 2024

This appendix gives the standing-wave assessment for the near-stationary window on 11 July 2024 (9h–21h), following the same approach as for the campaign-averaged spectra in Section 4.3.3. Table I.1 lists the IG-band peak and valley frequency identified at each reef-flat sensor, and Figure I.1 compares their shallow water wavelengths with the node–antinode spacing expected for a standing wave with an antinode at the shoreline. The wavelengths were computed with the mean reef-flat depth over this window, $\bar{h} = 1.2\,\mathrm{m}$.

Table I.1: IG-band peak and valley frequency at each reef-flat sensor over the near-stationary window (9h–21h) on 11 July 2024. At RF1 the second IG peak is used, since its first peak lies at a considerably lower frequency than at the other sensors.

Sensor	Peak frequency [Hz]	Valley frequency [Hz]
RF7	0.0030	0.0021
RF5	0.0042	0.0021
RF4	0.0058	0.0024
RF3	0.0058	0.0036
RF1	0.0085	0.0045

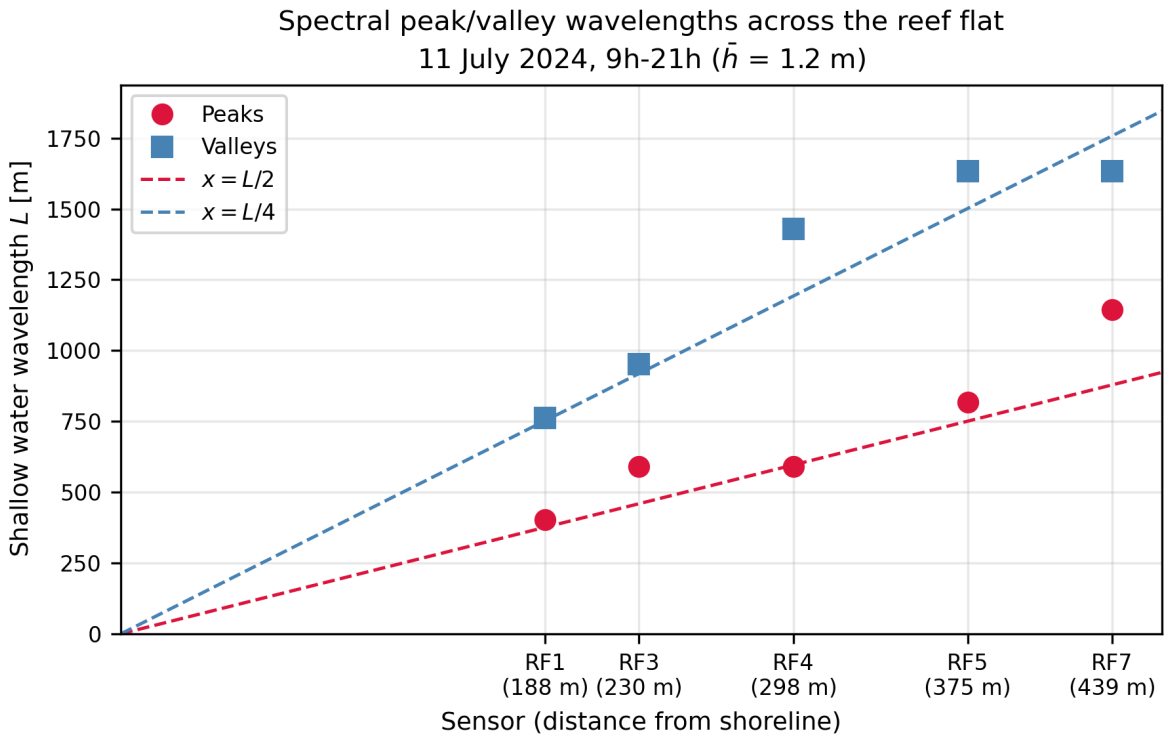


Figure I.1: Shallow water wavelength of the IG-band peak and valley frequencies at each reef-flat sensor over the near-stationary window (9h–21h) on 11 July 2024, plotted against distance from the shoreline. Peaks (antinodes) are compared against the $x = L/2$ line and valleys (nodes) against the $x = L/4$ line, both expected for a standing wave with an antinode at the shoreline.

Figure I.2 shows the cross-shore structure of the wave height at each of these peak frequencies, obtained with the narrow-band approach of Section 3.2.7, which illustrates this standing behaviour in space.

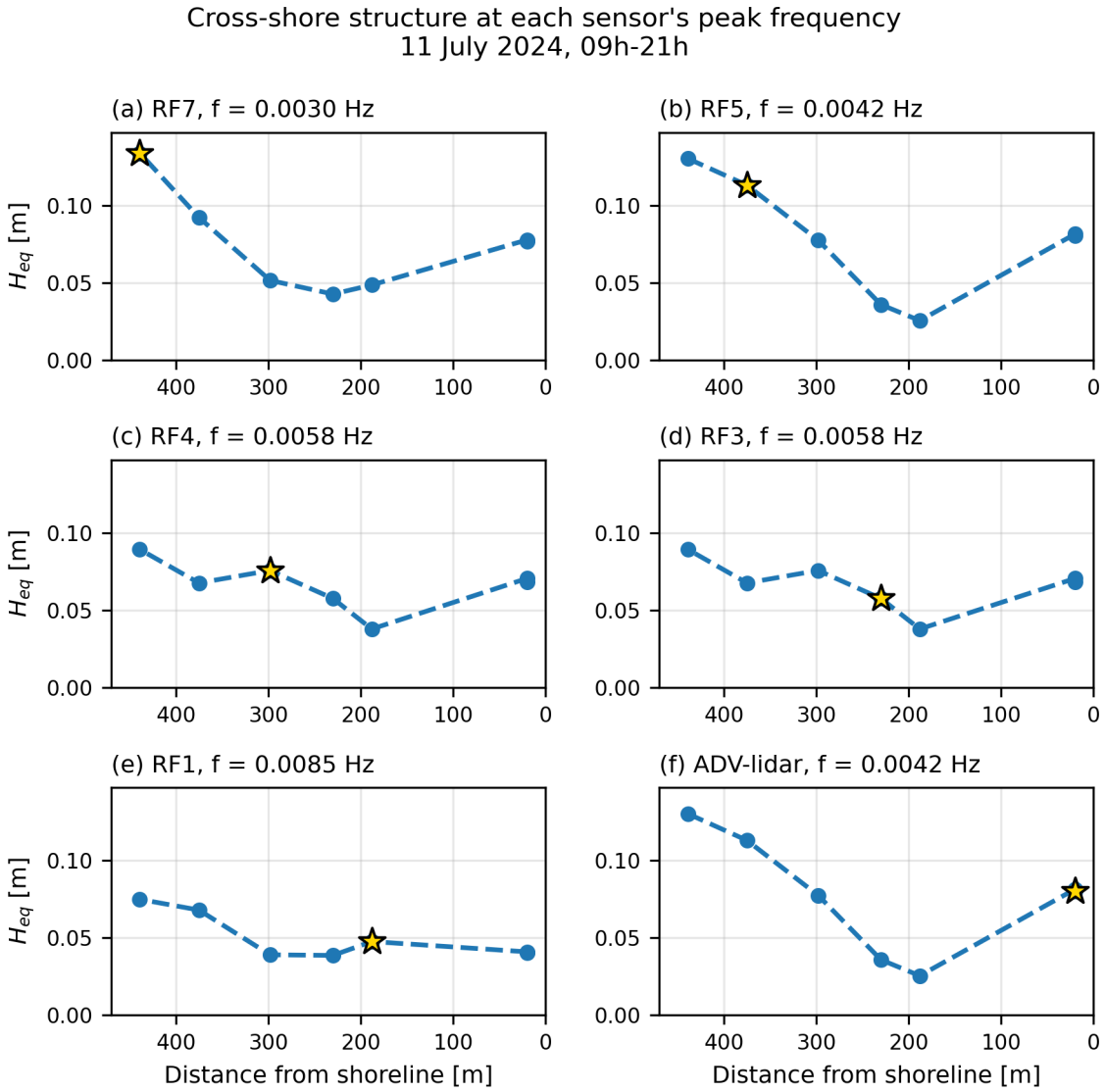


Figure I.2: Cross-shore structure of the wave height H_{eq} associated with each sensor's peak frequency over the near-stationary window (9h–21h) on 11 July 2024. Each panel uses the peak frequency identified for that sensor and shows the profile across the whole array, with the sensor's own position marked by a star. The vertical axis is the same in every panel.

J IG peaks frequency difference on 11 July 2024

This appendix shows the comparison described in Section 5.5.2 to the mean spectrum of 11 July 2024 over the near-stationary window (9h-21h).

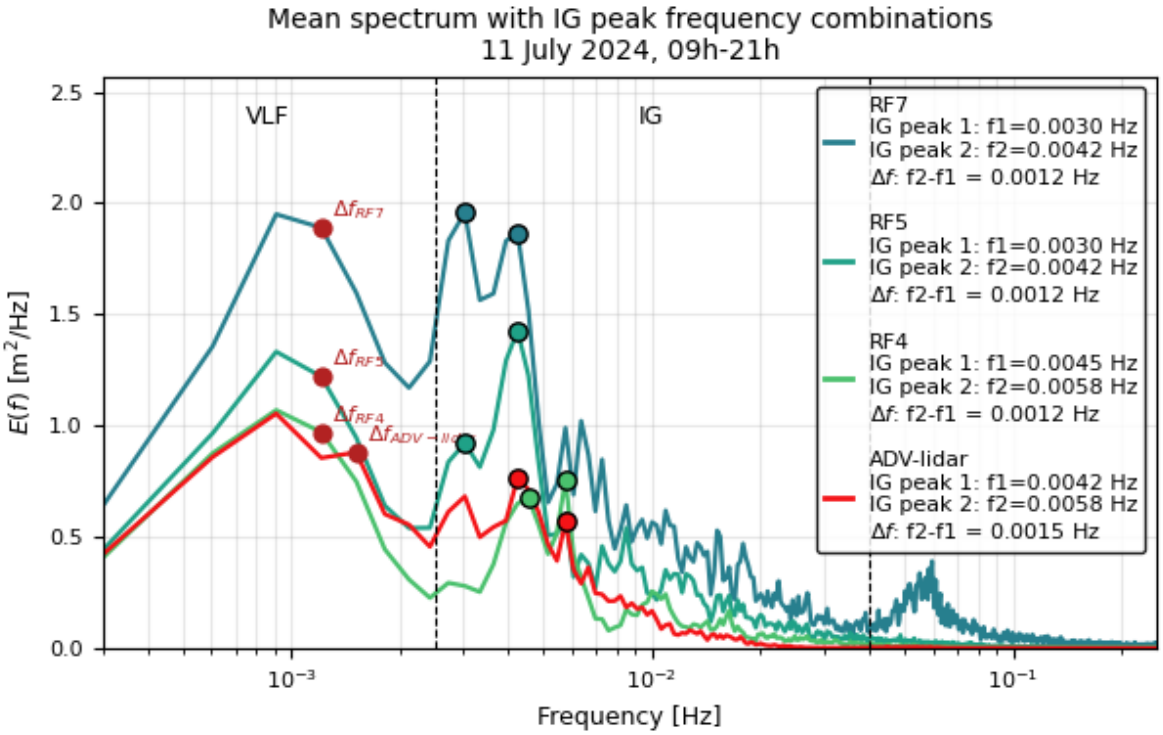


Figure J.1: Mean spectrum on 11 July 2024 at RF7, RF5, and RF3, with the highest IG-band peak, a smaller secondary IG peak, and their difference frequency marked.